UNIVERSITY OF CALIFORNIA

Santa Barbara

# Integrated Stress-Optic Silicon Nitride Photonics for Communications and Atomic Applications

A dissertation submitted in partial satisfaction of the

requirements for the degree Doctor of Philosophy

in Electrical and Computer Engineering

by

Jiawei Wang

Committee in charge:

Professor Daniel J. Blumenthal, Chair

Professor Steven P. DenBaars

Professor Galan Moody

Dr. Ryan Q. Rudy

March 2024

The dissertation of Jiawei Wang is approved.

_____

Dr. Ryan Q. Rudy

_____

Professor Galan Moody

_____

Professor Steven P. DenBaars

_____

Professor Daniel J. Blumenthal, Committee Chair

January 2024

Integrated Stress-Optic Silicon Nitride Photonics for Communications and Atomic Applications



Jiawei Wang

# ACKNOWLEDGEMENTS

Completing my Ph.D. journey at the UCSB has been a remarkable experience filled with both challenges and profound growth. Throughout this academic odyssey, I have had the privilege of acquiring invaluable knowledge and having meaningful connections with exceptional individuals who have supported me along the way.

Foremost, I would like to express my gratitude to my advisor Professor Daniel J. Blumenthal for giving me the opportunity, platform, and facilities to conduct cutting-edge research in integrated photonics devices. With the mentorship from Dan at OCPI, I not only advanced my research skills but also learned life lessons and witnessed the highest standards of integrity, work ethic, and enthusiasm for pioneering research. I truly have benefited from his attitudes towards research, and these have shaped me into a better person, preparing me for a promising future in my career.

I would also like to thank my committees Professor Steven Denbaars, Professor Galan Moody, and Dr. Ryan Rudy for their guidance, discussion, and encouragement during my Ph.D. Special thanks go to Ryan for his effort to fabricate and test the PZT devices and provide his invaluable insight advice and guidance during our discussions.

Next, I want to thank all my exceptional lab mates in the Optical Communication and Photonic Integration group. Without their unwavering support, collaborative spirit, and expertise I could not conduct productive research and have meaningful discussions and ideas. Especially, I want to express my appreciation to Nitesh, Kaikai, Andrei, and Mark for assisting me with various measurements and simulations and for their invaluable advice and technical support, Debapam for working with me together in the cleanroom, and Grant, Qiancheng, Renan, and Meiting for their guidance in research. The knowledge and expertise

shared within our group have been instrumental in my Ph.D. completion. All of them are truly smart and remarkable people, I have no doubt that all of them will succeed and be pioneers in their future career endeavors. Furthermore, I would like to acknowledge the UCSB Nanofab staff for providing world-class cleanroom facilities and assistance in processing and fabrication, especially Demis John and Brian Thibeault.

Santa Barbara has held a special place in my heart ever since I arrived in the USA. I really enjoyed the pleasant weather and the beautiful ocean and beaches. This chapter of my life would not have been as unforgettable without the companionship of my friends. I extend my gratitude to Weiyi, Yue, Ming, Yichen, Fengqiao, David, Alisson, and Angela as well as my non-UCSB friends Yu, Yiren, Yujie, Hangjie, and Leihao for spending so many good times together, traveling, hiking, snowboarding and much more.

Finally, I wish to express my profound gratitude to my parents for their unconditional love and support. As an international student, being far from home and not having seen my parents for over five years has been incredibly challenging. It is their enduring love and faith in me that have provided me with the motivation to persevere. And I have been extremely fortunate to meet my wife Menglin during my time at UCSB. I cannot overstate the significance of her presence in my life – her constant support, patience, kindness, and care. Last, I want to thank our cats Taro and Luna for the joy and happiness they bring into our lives.

***Dedicated to my family, Xinjun and Yanlin, and my love, Menglin***

VITA OF JIAWEI WANG

February 2024

## EDUCATION

Doctor of Philosophy in Electrical and Computer Engineering — Feb '24
*University of California, Santa Barbara*
Doctoral Advisor: Prof. Daniel J. Blumenthal

Master of Science in Electrical Engineering — Jun '17
*University of California, Los Angeles*
M.Sc Advisor: Prof. Benjamin Williams

Bachelor of Engineering, School of Optical and Electronic Information — Jun '15
*Huazhong University of Science and Technology, Wuhan, China*

Exchange Student, Electrical Engineering and Information Technology — Sep '14 - Jun '15
*RWTH Aachen University, Aachen, Germany*

## PROFESSIONAL EMPLOYMENT

Photonic Test Engineering Intern — Jun '23 - Sep '23
*OpenLight Photonics, Inc., Santa Barbara, CA*

Secretary, Photonic Society at UCSB — Jan '21 – Jan '22
*University of California, Santa Barbara*

Graduate Student Researcher — Sep '17 - Jan '24
*Dept. ECE, University of California, Santa Barbara*

*Graduate Student Researcher* — Jun '16 - Jun '17
*Dept. ECE, University of California, Los Angeles*

## JOURNAL PUBLICATIONS

**Wang, J.**, Liu, K., Isichenko, A., Rudy, R. Q., & Blumenthal, D. J. (2023). Integrated programmable strongly coupled three-ring resonator photonic molecule with ultralow-power piezoelectric control. *Optics Letters, 48*(9), 2373-2376.

**Wang, J.**, Liu, K., Harrington, M. W., Rudy, R. Q., & Blumenthal, D. J. (2022). Silicon nitride stress-optic microresonator modulator for optical control applications. *Optics Express, 30*(18), 31816-31827.

Liu, K., **Wang, J.**, Chauhan, N., Harrington, M. W., Nelson, K. D., & Blumenthal, D. J. (2024). Integrated photonic molecule Brillouin laser with a high-power sub-100-mHz fundamental linewidth. *Optics Letters, 49*(1), 45-48.

Isichenko, A., Chauhan, N., Bose, D., **Wang, J.**, Kunz, P. D., & Blumenthal, D. J. (2023). Photonic integrated beam delivery for a rubidium 3D magneto-optical trap. *Nature Communications*, 14(1), 3080.

Liu, K., Chauhan, N., **Wang, J.**, Isichenko, A., Brodnik, G. M., Morton, P. A., Behunin, R.O., Papp, S.B. & Blumenthal, D. J. (2022). 36 Hz integral linewidth laser based on a photonic integrated 4.0 m coil resonator. *Optica*, *9*(7), 770-775.

Chauhan, N., **Wang, J.**, Bose, D., Liu, K., Compton, R. L., Fertig, C., Hoyt, C.W. & Blumenthal, D. J. (2022). Ultra-low loss visible light waveguides for integrated atomic, molecular, and quantum photonics. *Optics express, 30*(5), 6960-6969.

Chauhan, N., Isichenko, A., Liu, K., **Wang, J.**, Zhao, Q., Behunin, R. O., ... & Blumenthal, D. J. (2021). Visible light photonic integrated Brillouin laser. *Nature Communications, 12*(1), 4685.

Zhao, Q., Behunin, R. O., Rakich, P. T., Chauhan, N., Isichenko, A., **Wang, J.**, ... & Blumenthal, D. J. (2020). Low-loss low thermo-optic coefficient Ta2O5 on crystal quartz planar optical waveguides. *APL Photonics*, *5*(11).

Sun, S., Wang, B., Liu, K., Harrington, M., Tabatabaei, F., Liu, R., **Wang, J**., Hanifi, S., Morgan, J.S., Jahanbozorgi, M. and Yang, Z., (2024). Integrated optical frequency division for stable microwave and mmWave generation. *Nature*, 1-6.

## CONFERENCE PUBLICATIONS

**Wang, J.**, Liu, K., Rudy, R. Q., & Blumenthal, D. J. (2023, June). AOM-Free Laser Stabilization using integrated Silicon Nitride Carrier-Tracking Stress-Optic Modulator and Reference Cavity. In *Quantum 2.0* (pp. QW3B-3). Optica Publishing Group.

**Wang, J.**, Liu, K., Harrington, M. W., Rudy, R. Q., & Blumenthal, D. J. (2022, May). A low-power PZT stress-optic Si3N4 micro-ring modulator for PDH locking applications. In *CLEO: Science and Innovations* (pp. STu5G-2). Optica Publishing Group.

**Wang, J.**, Liu, K., Harrington, M. W., Rudy, R. Q., & Blumenthal, D. J. (2022, March). Ultra-low loss silicon nitride ring modulator with low power PZT actuation for photonic

control. In *Optical Fiber Communication Conference* (pp. W3D-5). Optica Publishing Group.

**Wang, J.**, Zhao, Q., Rudy, R. Q., & Blumenthal, D. J. (2021, November). Low loss, low power, silicon nitride PZT stress-optic microresonator modulator for control functions. In *Frontiers in Optics* (pp. FW6B-2). Optica Publishing Group.

**Wang, J.**, Liu, K., Zhao, Q., Isichenko, A., Rudy, R. Q., & Blumenthal, D. J. (2021, May). Independently Coupled and PZT Controllable Photonic Integrated Three-Resonator Photonic Molecule. In *CLEO: Science and Innovations* (pp. STu1F-7). Optica Publishing Group.

Liu, K., Harrington, M. W., **Wang, J.**, Nelson, K. D., & Blumenthal, D. J. (2023, October). Integrated self-delayed 2-m coil-resonator for high sensitivity optical frequency discrimination and laser linewidth narrowing. In *Laser Science* (pp. JW4A-22). Optica Publishing Group.

Sun, S., Wang, B., Liu, K., **Wang, J.**, Liu, R., Jahanbozorgi, M., ... & Yi, X. (2023, October). Integrated Optical Frequency Division with SiN-based Reference Cavity and Microcomb. In *Frontiers in Optics* (pp. FTh3E-4). Optica Publishing Group.

Liu, K., Harrington, M. W., **Wang, J.**, Isichenko, A., Chauhan, N., Nelson, K. D., & Blumenthal, D. J. (2023, October). Integrated tunable two-point-coupled 10-meter 336 million Q coil-resonator for laser stabilization. In *Frontiers in Optics* (pp. FM6D-6). Optica Publishing Group.

Isichenko, A., Chauhan, N., **Wang, J.**, Bose, D., Liu, K., Harrington, M. W., & Blumenthal, D. J. (2023, July). Photonic integrated building-blocks for rubidium cold atom systems. In *2023 IEEE Photonics Society Summer Topicals Meeting Series (SUM)* (pp. 1-2). IEEE.

Liu, K., **Wang, J.**, Chauhan, N., & Blumenthal, D. J. (2023, July). Circulator-free photonic integrated Brillouin laser. In *Nonlinear Optics* (pp. Tu2A-3). Optica Publishing Group.

Blumenthal, D. J., Chauhan, N., Isichenko, A., **Wang, J.**, Bose, D., Liu, K., & Harrington, M. W. (2023, June). Visible Light Photonics for Atomic and Quantum Sensing and Computation. In *Quantum 2.0* (pp. QTu4C-1). Optica Publishing Group.

Blumenthal, D. J., Chauhan, N., Isichenko, A., Liu, K., & **Wang, J.** (2023, March). Integrated stabilized lasers and circuits for atom cooling, trapping, and interrogation. In *Quantum Sensing, Imaging, and Precision Metrology* (Vol. 12447, pp. 157-161). SPIE.

Chauhan, N., Isichenko, A., **Wang, J.**, & Blumenthal, D. J. (2022, November). Sub-dB/m loss integrated 103 and 90 million Q resonators for laser stabilization at rubidium and strontium wavelengths. In *2022 IEEE Photonics Conference (IPC)* (pp. 1-2). IEEE.

Chauhan, N., Liu, K., Isichenko, A., **Wang, J.**, Timmers, H., & Blumenthal, D. J. (2022, October). Integrated 3.0 meter coil resonator for λ= 674 nm laser stabilization. In *Frontiers in Optics* (pp. FM1E-1). Optica Publishing Group.

Bose, D., **Wang, J.**, & Blumenthal, D. J. (2022, May). 250C process for< 2dB/m ultra-low loss silicon nitride integrated photonic waveguides. In *CLEO: Science and Innovations* (pp. SF3O-1). Optica Publishing Group.

Liu, K., Chauhan, N., **Wang, J.**, Isichenko, A., Brodnik, G. M., Morton, P. A., ... & Blumenthal, D. J. (2022, March). Semiconductor laser stabilized by a photonic integrated 4 meter coil-waveguide resonator. In *Optical Fiber Communication Conference* (pp. Tu3D-2). Optica Publishing Group.

Liu, K., Chauhan, N., **Wang, J.**, Morton, P. A., Behunin, R., & Blumenthal, D. J. (2021, November). Precision laser stabilization using photonic integrated coil resonator. In *Frontiers in Optics* (pp. FTh2A-1). Optica Publishing Group.

Zhao, Q., Harrington, M. W., Isichenko, A., Bose, D., **Wang, J.**, Liu, K., ... & Blumenthal, D. J. (2021, June). Silicon Nitride Bus-Coupled Spiral-Ring Resonator for Dual-Mode Locking Temperature Stabilization. In 2021 *Optical Fiber Communications Conference and Exhibition (OFC)* (pp. 1-3). IEEE.

Liu, K., Puckett, M. W., Harrington, M. W., Brodnik, G. M., Zhao, Q., Chauhan, N., **Wang, J.,**... & Blumenthal, D. J. (2021, May). Milliwatt threshold ultra-Low linewidth photonic integrated Si3N4 Brillouin laser. In *CLEO: Science and Innovations* (pp. SF2O-1). Optica Publishing Group.

Zhao, Q., **Wang, J.**, Chauhan, N., Bose, D., Jin, N., Moreira, R., ... & Blumenthal, D. (2020, May). Low-Loss D-Shape Silicon Nitride Waveguides using a Dielectric Lift-Off Fabrication Process. In *2020 Conference on Lasers and Electro-Optics (CLEO)* (pp. 1-2). IEEE.

Chauhan, N., **Wang, J.**, Bose, D., Moreira, R., & Blumenthal, D. J. (2020, May). Ultra-low loss 698 nm and 450 nm silicon nitride visible wavelength waveguides for strontium atomic clock applications. In *CLEO: Science and Innovations* (pp. STh1J-2). Optica Publishing Group.

Puckett, M. W., **Wang, J.**, Bose, D., Brodnik, G. M., Wu, J., Nelson, K., & Blumenthal, D. J. (2019, June). Silicon nitride ring resonators with 0.123 dB/m loss and Q-factors of 216 million for nonlinear optical applications. In *2019 Conference on Lasers and Electro-Optics Europe & European Quantum Electronics Conference (CLEO/Europe-EQEC)* (pp. 1-1). IEEE.

## AWARDS

Doctoral Student Travel Grant (2022-2023)

Doctoral Student Travel Grant (2021-2022)

Excellent Graduate, *Huazhong University of Science and Technology*, 2015

Outstanding Scientific Research Achievement Award, *Hubei Provincial Department of Education*, China, 2015

# ABSTRACT

Integrated Stress-Optic Silicon Nitride Photonics for Communications and Atomic Applications

by

Jiawei Wang

Modulation-based control and locking of lasers, filters, and other photonic components is a ubiquitous function across many applications that span the visible to infrared (IR) range, including atomic, molecular, and optical (AMO), quantum sciences, fiber communications, metrology, and microwave photonics. Today, modulators used to realize these control functions consist of high-power bulk-optic components for tuning, sideband modulation, and phase and frequency shifting while providing low optical insertion loss and moderate operation bandwidth. To enhance the power efficiency, scalability, and cost-effectiveness of these applications while reducing their size and weight, it is imperative to implement modulation control functions in a low-loss, wafer-scale complementary metal-oxide-semiconductor (CMOS)-compatible photonic integration platform. The silicon nitride integration platform has been successful in realizing extremely low waveguide losses across the visible to infrared range [1,2] and components including high-performance lasers [3], filters [4], resonators, stabilization cavities [5], and optical frequency combs [6]. However, the advancement in incorporating low-loss, low-power modulators into the silicon nitride platform while maintaining compatibility with wafer-scale processes has been constrained.

This dissertation represents significant progress in the integration of a piezo-electric (PZT, lead zirconate titanate) actuated micro-ring modulator within a fully planar, wafer-scale silicon nitride platform, at both 1550 nm and 780 nm. This integration maintains low optical losses at infrared and visible wavelengths, accompanied by an order of magnitude increase in optical bandwidth (DC to 25 MHz 3-dB) and an order of magnitude lower power consumption of 20 nW improvement over prior PZT modulators [7,8]. This work demonstrated control applications utilizing the developed PZT modulator as sideband modulation in a Pound-Drever Hall (PDH) lock loop for laser stabilization and as a laser carrier tracking filter. Subsequently, an AOM/EOM-free laser stabilization scheme is demonstrated unifying both functions using a single PZT modulator. This approach has the potential to pave the way for photonic integrated stabilized lasers, given the compatibility of the PZT modulator with both the integrated reference cavity [9] and lasers [3,10]. The PZT modulator design can be extended to the visible region in the ultra-low loss silicon nitride platform with waveguide design changes. The integration of PZT modulation in the ultra-low loss silicon nitride waveguide platform enables modulator control functions in a wide range of visible to IR applications such as atomic and molecular transition locking for cooling, trapping and probing, controllable optical frequency combs, low-power external cavity tunable lasers, quantum computers, sensors and communications, atomic clocks, and tunable ultra-low linewidth lasers, and ultra-low phase noise microwave synthesizers. Finally, more complex photonic structures with PZT control are investigated, such as symmetrically coupled photonic molecules and their potential applications in optical isolators and high-order switchable filters. These results open the door to novel device designs and a wide range of applications including tunable lasers, high-order suppression

ultra-narrow linewidth lasers, dispersion engineering, optical parametric oscillators, physics simulations, and atomic and quantum photonics.

TABLE OF CONTENTS

ACKNOWLEDGEMENTS ..... iv

VITA OF JIAWEI WANG ..... vii

ABSTRACT ..... xii

LIST OF FIGURES ..... xvii

LIST OF TABLES ..... xxiv

1. Introduction ..... 1

1.1 Background on Silicon Nitride Photonics ..... 1

1.2 Motivation of Stress-Optic Modulation on Silicon Nitride Platform ..... 2

1.3 The Structure and Scope of this Thesis ..... 4

2. PZT-actuated Silicon Nitride Microresonator Modulator ..... 7

2.1 Introduction ..... 7

2.2 Microresonator Design for Infrared and Visible Wavelengths ..... 7

2.3. Piezoelectricity and Stress-optic Simulation and Design ..... 12

2.4. Fabrication Processes ..... 17

3. Characterization of PZT Modulator ..... 25

3.1 Resonator Quality Factor and Loss Measurement ..... 25

3.2 PZT Actuator Static Tuning Measurement ..... 29

3.3 Modulator Bandwidth Measurement ..... 33

3.4 Modulator Linearity Measurement ..... 38

4. PZT Modulation in Laser Stabilization Control Applications ..... 42

4.1 Introductions to PDH Locking and Laser Stabilization ..... 42

4.2 Control Applications: Sideband Modulation and Carrier Tracking with PZT Modulation....43
4.3 AOM/EOM-free Laser Stabilization with PZT Modulation....48
5. Integrated Symmetrically-coupled Three-Ring Photonic Molecule with PZT Control 55
5.1 Introduction of Photonic Molecule....55
5.2 Device Design and Simulation....60
5.3 Device Characterization and PZT Control Demonstration....68
5.4 Discussion of the work....71
6. Discussion and Future Work....74
6.1 Non-magnetic integrated optical isolator and circulator....74
6.2 PZT-actuated fast-switchable high-order ring filter....78
6.3 Photonic integrated stabilized laser....80
References....82

LIST OF FIGURES

Figure 1. 1 Prior art of different modulation method on silicon nitride platform. .....4

Figure 2. 1 Waveguide design for different wavelengths of 1550 nm and 780 nm. .....7

Figure 2. 2 Simulated mode profiles in 175 nm core for λ = 1550 nm and 120 nm core for λ = 780 nm. .....10

Figure 2. 3 Bend loss simulation for resonator designs at λ = 1550 nm and λ = 780 nm. 10

Figure 2. 4 Coupling coefficients simulation for bus-ring and ring-ring at λ = 1550 nm. 11

Figure 2. 5 Coupling coefficients simulation for bus-ring and ring-ring at λ = 780 nm. 11

Figure 2. 6 (a) Cross-section of the device, the PZT actuator is deposited on top of the waveguide with certain offsets to achieve the best performance without affecting the optical loss. (b) Illustration of the stress-optic microresonator modulator, the PZT actuator (yellow) is monolithically integrated on top of the $Si_3N_4$ resonator (black) without under-etching process. .....12

Figure 2. 7 Device working principle: converse piezoelectric effect and stress-optic effect. .....13

Figure 2. 8 Piezoelectric and stress-optic simulation in COMSOL.....15

Figure 2. 9 Simulation of effective index change with different (a) PZT offsets and thickness and (b) PZT offsets and widths. .....16

Figure 2. 10 Simulation of waveguide loss with different cladding thickness and metal offset design.....17

Figure 2. 11 Passive silicon nitride waveguide fabrication process .....18

Figure 2. 12 SEM images of fabricated waveguides. .....20

Figure 2. 13 AFM measurement of waveguide edge.....20
Figure 2. 14 AFM measurement of waveguide top and bottom surfaces.....21
Figure 2. 15 PZT fabrication process. .....21
Figure 2. 16 (a) Fabricated PZT-actuated silicon nitride ring modulator; (b) Mask layout and layer description of the device.....23
Figure 2. 17 X-ray diffraction (XRD) scan of the PZT material. .....24

Figure 3. 1 (a) The optical image of the fabricated PZT modulator resonator. (b) The Q measurement of the 1550 nm resonator. The calibrated MZI with a 5.87 MHz FSR acts as a frequency ruler (yellow trace) to measure the FWHM of the resonator resonance (blue trace). (c) System diagram of the quality factor measurement with the calibrated MZI.....26
Figure 3. 2 Summary of the simulation data, showing that the 2 μm offset results in the largest strain effect. (b) The measurement of the fabricated devices agrees with the simulation. .....28
Figure 3. 3 The Q measurement of the 780 nm resonator. The calibrated MZI with a 24 MHz FSR acts as a frequency ruler (blue trace) to measure the resonator resonance (red trace).....29
Figure 3. 4 The optical transmission spectrum of the static tuning of the device. The resonance has a 14 dB extinction ratio (ER) across the 4 GHz tuning range. (c) The linear fitting of the tuning curve corresponds to -1.3 pm/V or -162 MHz/V tuning coefficient.....30
Figure 3. 5 Thermal tuning of the Pt heater located inside the PZT actuator.....32

Figure 3. 6 PZT static tuning of (a) No PZT offset design with 480 MHz/V tuning strength and (b) 2 μm PZT offset design with -150 MHz/V tuning strength.....32

Figure 3. 7 (a) The experimental diagram for small-signal electrical-to-optical frequency response measurements. (b) The frequency response (S21) indicates that the 3-dB and 6-dB modulation bandwidth is 15 MHz and 25 MHz, respectively.33

Figure 3. 8 Optical response calculation at different detuning point (red and orange curve) with measured optomechanical response S21 (blue curve).....36

Figure 3. 9 Modeling of the frequency response system divided into (1) electric, (2) opto-mechanic and (3) optical response. .....37

Figure 3. 10 The frequency response ($S_{21}$) (a) amplitude information and (b) phase information of the 780 nm PZT modulator. .....38

Figure 3. 11 (a) The experimental diagram for two-tone spurious-free dynamic range (SFDR) measurements. (b) Detected RF power of the carrier frequencies at 9.5 MHz and 10.5 MHz and the third-order intermodulation distortion (IMD3) frequencies at 8.5 MHz and 11.5 MHz with 1 kHz resolution bandwidth. (c) and (d) RF output power of the fundamental and third order intermodulation distortion (IMD3) component as a function of RF input power of the ring modulator at 1 MHz and 10 MHz.....39

Figure 4. 1 Laser stabilization demonstration. (a) Illustration of DSB modulated carrier. (b) Measured DSB spectrum of the laser signal with and without the PZT DSB modulation, showing the 40MHz sidebands with modulation depth of 0.48. (c) A semiconductor laser is PDH locked to an ultra-high Q (UHQ) reference cavity

using the PZT modulator as a double sideband (DSB) modulator, replacing the electro-optic modulator (EOM). The double sideband modulated carrier is frequency shifted by an acousto-optic modulator (AOM) and locked to the quadrature point of an UHQ integrated reference resonator using a proportional–integral–derivative (PID) control loop that drive a voltage-controlled oscillator (VCO) AOM frequency shift control signal. The resulting stabilized frequency noise is measured using an unbalanced fiber MZI optical frequency discriminator (OFD). (d) Measured frequency noise (FN) power spectral density for the free-running (blue trace) and stabilized laser (red trace) showing 40 dB close to carrier noise reduction and near thermo-refractive noise (TRN) limited performance for the 1 kHz to 10 kHz frequency range. .....45

Figure 4. 2 (a) The PZT-actuated ring modulator is locked to the laser in a PID locking loop, when an external signal is applied to the laser, the locked modulator will respond to the signal dithering and track the laser carrier. The scope at the output port recorded the optical level fluctuation (orange) with the signal dithering in the laser signal (blue). (b) The total response of the feedback loop shows the bandwidth is close to 1 MHz. (c) Step input, control loop response, and tracking filter output stabilization time (from 90% to 10%) ~ 130 μs with ~ 8 μs settling time. .....48

Figure 4. 3 Dual stage laser stabilization using integrated silicon nitride ultra-high Q resonators [84] as (a) nonlinear Brillouin laser resonator and (b) reference cavity to achieve laser noise reduction at both high- and low-frequency. (c) Frequency noise illustration showing the frequency noise of the laser can be first reduced at

the high frequency offset from the carrier due to the nonlinear Brillouin process and then further reduced at the low frequency offset from the carrier by PDH locking to a reference cavity.....49

Figure 4. 4 Experimental diagram for AOM-free photonic integrated stabilization. VCO, voltage-controlled oscillator. UHQ cavity, ultra-high quality factor cavity. PD, photodetector.....52

Figure 4. 5 (a) Frequency noise measurement for the free-running and stabilized laser with simulated TRN in the reference cavity. (b) The ADEV plots of the free-running and the stabilized laser.....52

Figure 4. 6 Illustrative example application of PZT-actuated modulator for control functions in an external cavity laser (ECL). The PZT actuator can be used to tune and control the ECL, and generate sidebands to further stabilize the laser fluctuation by Pound-Drever Hall (PDH) locking to an ultra-high Q reference cavity. The stabilized output can be modulated (optional) based on specific applications. 53

Figure 5. 1 Analogy of hydrogen model to photonic molecule.....56

Figure 5. 2 Previous work on photonic molecule. .....59

Figure 5. 3 Illustration of PZT controlled photonic molecule and optical micrograph of a fabricate device with monolithically integrated PZT actuators.....60

Figure 5. 4 (a) Coupled photonic molecule model and (b) the comparison with hydrogen model. (c) The energy state splitting of three coupled atoms.....62

Figure 5. 5 Simulation of the symmetric alignment case of transmission and reflection spectrum. .....64

Figure 5. 6 Lumerical INTERCONNECT schematic diagram. ..... 65

Figure 5. 7 Lumerical INTERCONNECT simulation of (a) symmetric aligned case and (b) non-degenerate splitting case. Blue curve represents the through port output and the red and green curve represent the drop ports at the two other rings. ..66

Figure 5. 8 Comparison between the coupled photonic molecule (CPM) modeling (left side) and Lumerical simulation for different cases (right side). ..... 67

Figure 5. 9 The quality factor (Q) measurement of a single ring resonator with R = 580 μm with and without PZT actuator. ..... 68

Figure 5. 10 Measured and modeled PM transmission spectra for a single bus. ..... 69

Figure 5. 11 Spectrum measurements of the photonic molecule (a) at both through port (b) and drop ports (c)..... 70

Figure 5. 12 (a)-(c): DC biasing of rings A, B and C. The colored lines indicate the measured transmission spectrums as DC bias is adjusted from 0 to 15V and the dashed black lines are the coupled photonic molecule model fitting. (d) The symmetric case can be reached by tuning multiple rings; N.T., normalized transmission. ..... 71

Figure 6. 1 (a) Three-port integrated optical isolator/circulator; (b) Imparting equivalent angular moment via parametric modulation of three coupled resonators with three RF signals of same amplitude and 120 degrees phase shift from each other to induce magnetic-free optical non-reciprocity; (c) Measurements showing RF probing of three resonators photonic molecule with PZT actuators..... 76

Figure 6. 2 Measurement setup for 780 nm isolator test. The three RF signals are generated from the arbitrary waveform generator (AWG) and are phase synchronized, and then are amplified and applied to each resonator via the PZT actuator modulation. ..... 77

Figure 6. 3 Third and fourth order ring filter design for 780 nm and 1550 nm. Thermal heater using the bottom Pt electrode layer is patterned inside the ring to assist for cascaded ring resonance alignment. ..... 79

Figure 6. 4 Simulation of the high-order ring filter at 1550 nm. For third order filter design, a flat passband about 6 GHz with 100 dB extinction ratio can be reached; for fourth order filter design, a flat passband about 6 GHz with 120 dB extinction ratio can be reached. ..... 79

Figure 6. 5 External cavity laser with PZT actuator integrated on vernier rings and waveguide to detune the laser. ..... 81

Figure 6. 6 Photonic integrated stabilized laser source with SBS resonator and reference cavity. The PZT actuator is integrated on top of the SBS resonator and filter to directly control the SBS laser. The PZT ring modulator is used as DSB modulator to generate sidebands on the laser carrier for PDH locking to the coil reference cavity. ..... 81

# LIST OF TABLES

Table 1. 1 Comparison of different modulation method on silicon nitride platform. ...4

Table 2. 1 Refractive indexes used in Lumerical mode profile simulation. .....9

Table 2. 2 Indexes used in piezoelectric simulation in COMSOL. .....14

Table 5. 1 Summary of this work with comparable integrated ring-resonator modulator. SOI: silicon on insulator; TEC: thermoelectric cooler. * Extracted based on the information provided in the literature.....73

# 1. Introduction

## *1.1 Background on Silicon Nitride Photonics*

The silicon nitride ($Si_3N_4$) photonic integrated platform [11,12] delivers ultra-low waveguide losses, low-temperature coefficient, high optical power density handling, and broad passive functionality across the visible range through the IR wavelength range [1,2] in a planar wafer-scale CMOS-compatible process. This platform has the potential to provide the benefits of integration, namely low-cost, portability, low-power, scalability, and enhanced reliability to a wide range of applications including quantum information sciences and applications [13,14], optical atomic clocks [15,16], precision metrology [17,18], atomic, molecular and optical [19], microwave photonics [20,21], fiber optic precision frequency distribution [22–24], and energy-efficient communications [25]. A ubiquitous function among these applications is optical actuation and modulation, to perform tuning and control functions including wavelength shifting, sideband and sweep modulation, and phase shifting, with low optical insertion loss and modulation bandwidths from DC to 10s of MHz and higher. Examples include laser locking to reference cavities, and atomic transitions [26] and optical channel tracking in fiber communications [27]. Today, these systems use power-consuming bulk-optic electrooptic (EOM) [28] and acousto-optic (AOM) [29] modulators to implement control loops, such as the PDH [30,31] and proportional, integration, and derivative (PID) [26,32]. Devices and functions that will benefit from integrated, low-power, active modulation include hybrid tunable lasers [33], optical frequency combs [34,35], Brillouin lasers [2,36,37], atomic and ion transition trapping, cooling and locking [15,38], laser stabilization [39], phase-lock loops [22], and cryogenic applications [40,41]. However,

it has remained a challenge to transition these modulators to the silicon nitride platform while maintaining ultra-low optical loss in a CMOS-compatible, wafer-scale process. Therefore, integrated control modulators that maintain the desirable properties of the silicon nitride platform as well as low-power consumption are required.

### *1.2 Motivation of Stress-Optic Modulation on Silicon Nitride Platform*

Efforts have been made to realize tuning and modulation in ultra-low loss silicon nitride photonics. Silicon nitride has a high third-order Kerr nonlinearity which is suitable for generating octave-spanning frequency comb [42] and stimulated Brillouin scattering (SBS) [3], however, due to its centrosymmetric crystal structure, silicon nitride has a small second-order Pockels effect with a maximum electro-optic (EO) coefficient of 8.31±5.6 fm/V [43] and cannot make use of free-carrier modulation like silicon [44]. Conventional thermal tuning approaches support bandwidths of up to 10 kHz [6] with 40 mW silicon nitride tuners [41]. The heterogeneous integration of nonlinear materials and silicon nitride waveguides introduces second-order nonlinearities for EO modulation, such as lithium niobate [45], ferroelectrics [46], and zinc oxide [47], as shown in Figure 1.1. These methods offer modulation bandwidths above 1 GHz; however, they suffer from large optical losses, increased fabrication complexity, higher power consumption, and a limited material optical wavelength range owing to the heterogeneous integration of different materials. Electrically poling of silicon nitride films can align Si-N bonds and induce second-order nonlinearity in silicon nitride materials [48,49], demonstrating a modulation bandwidth of >100 MHz; however, this method requires a high-power $CO_2$ laser above 10 W to heat the device to hundreds of degrees of poling temperature [48] with an extremely high poling voltage approximately 1000 V [49] and days of operation, which is not compatible with other

processes and experiments. The stress-optic effect, on the other hand, offers a broad optical bandwidth, moderate electrical bandwidth, and ultra-low power consumption. Stress-optic actuated silicon nitride waveguides have been demonstrated using piezoelectric materials, such as aluminum nitride (AlN) [40,50] and lead zirconate titanate (PZT) [7,8], as shown in Figure 1.1. AlN actuation utilizes acoustic resonant enhancement because of its relatively small piezoelectric coefficient (AlN: $e_{31,f} = 1.02\ C/m^2$, PZT: $e_{31,f} = -18.3\ C/m^2$ [51]) and tuning efficiency, which is an order of magnitude weaker than that of PZT [52]. The under-etched or waveguide-released PZT approach results in high loss, low Q, and limited modulation bandwidth (< 1 MHz), and is difficult to make compatible with planar wafer-scale integration [7]. Progress has been made with planar-processed PZT actuators including a Mach-Zehnder interferometer (MZI) phase modulator [8] with a modulation bandwidth of 629 kHz and high optical loss. Therefore, it is imperative to develop a planar-integrated, CMOS-compatible, low-loss and low-power modulation technique for ultra-low loss silicon nitride platform utilizing the stress-optic method and realize complex optical control functions on the chip. Table 1.1 summarizes the pros and cons of different modulation methods for silicon nitride in terms of modulation speed, optical loss, power consumption, and nitride waveguide optical transparency.

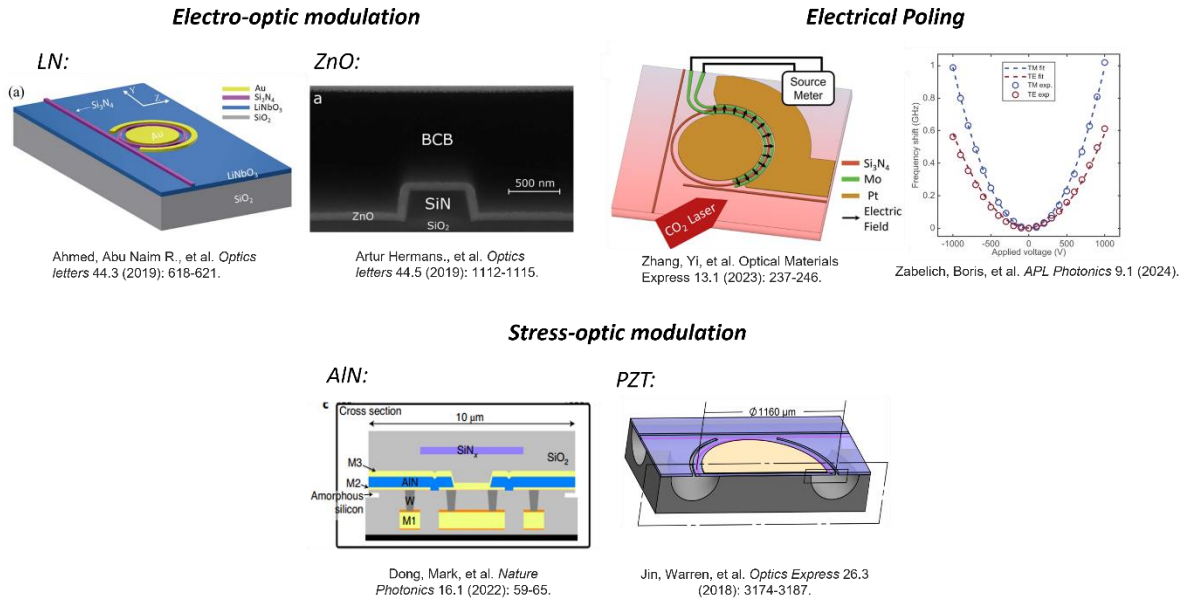


**Figure 1. 1 Prior art of different modulation method on silicon nitride platform.**

| Mechanism | Speed | Loss | Power Consumption | Optical Transparency |
|---|---|---|---|---|
| Thermal [6,53] | < 10 kHz | < 1dB/cm | > 40 mW | Broad |
| Electro-Optic [45,47] | > 1GHz | > 1 dB/cm | \ | Limited |
| Poling [48,49] | ~ 100 MHz | \ | HIGH | Limited |
| Stress-Optic [7,41] | MHz - GHz | < 0.4 dB/cm | ~ 10s nW | Broad |

**Table 1. 1 Comparison of different modulation method on silicon nitride platform.**

### *1.3 The Structure and Scope of this Thesis*

This dissertation focuses on the design and properties of PZT-actuated stress-optic modulator and its applications on silicon nitride waveguide platform. Chapter 1 briefly

introduces the properties and applications of silicon nitride integrated photonics. The motivation for using the stress-optic modulation method compared to other methods is then discussed.

In Chapter 2, silicon nitride waveguide and resonator designs at 1550 nm and 780 nm are discussed in detail. The PZT actuator designs are similar for both wavelengths and are discussed in detail, including the working principle, modeling, and simulation. Finally, the fabrication processes of both passive nitride waveguide patterning and an active PZT actuator are introduced.

In Chapter 3, PZT single-ring modulators at 1550 nm and 780 nm are discussed and characterized in detail. This includes the resonator quality factor and loss measurements, PZT actuator static tuning and static power consumption measurements, PZT modulator bandwidth, and linearity characterization.

In Chapter 4, different optical control applications using PZT modulation are demonstrated. First, the PZT modulator works as a double-sideband modulation and replaces the conventional electro-optic modulator (EOM) component in PDH locking circuits to realize laser stabilization and frequency noise suppression. Second, the PZT modulator was demonstrated to be locked and tracked to the laser carrier, which is important for monitoring and stabilizing wavelength changes to minimize the wavelength drift and spectral misalignments that cause power loss and signal distortion in fiber communications. Finally, by combining these two functions into one application, an AOM/EOM-free laser stabilization scheme is proposed and demonstrated using only one PZT modulator to replace the functions of bulky EOM phase modulation and AOM frequency shifting and realize laser

stabilization. This work can be instrumental as it can pave the way for all-waveguide, system-on-chip photonic integrated frequency-stabilized lasers.

In Chapter 5, a novel photonic molecule composed of three symmetrically and mutually coupled silicon nitride resonators with independent PZT actuators was designed and studied. Simulation and coupled-mode theory were developed to study the spectrum behavior and supermodes splitting under different coupling conditions. The PZT actuation and independent tuning control with low crosstalk on each photonic atom were also studied and demonstrated.

In Chapter 6, future work that can be enabled by PZT technology is discussed, including non-magnetic optical isolator/circulator, fast switchable high-order filters, and photonic integrated laser sources.

# 2. PZT-actuated Silicon Nitride Microresonator Modulator

## *2.1 Introduction*

Compared to the previous art of stress-optic actuated silicon nitride waveguide devices in Figure 1.1 [7,41] that require waveguide releasing and under-etching process, the PZT actuator in this thesis is monolithically integrated on a silicon nitride waveguide, and the devices are planar-processed and fabricated on the wafer scale.

## *2.2 Microresonator Design for Infrared and Visible Wavelengths*

The waveguide design and fabrication process are based on the silicon nitride ultra-low loss waveguide (ULLW) platform [1,2,11,54] developed at UCSB. There are two types of silicon nitride waveguide designs in this thesis, one for infrared wavelengths of 1550 nm and the other for visible wavelengths of 780 nm.

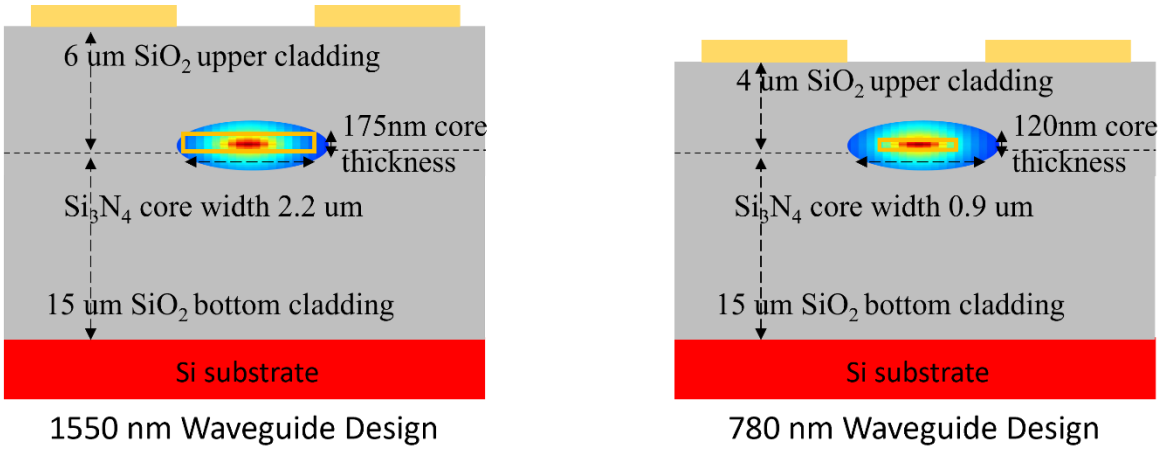


**Figure 2. 1 Waveguide design for different wavelengths of 1550 nm and 780 nm.**

As indicated in Figure 2.1, for 1550 nm, the waveguide thickness is chosen to be 175 nm, the width is 2.2 μm and the top cladding thickness is 6 μm. For 780 nm, the waveguide thickness is chosen to be 120 nm, the width is 0.9 μm and the top cladding thickness is 4 μm. For a fixed waveguide thickness, different waveguide widths support multiple optical modes, and the waveguide width is chosen to support only the fundamental TE and TM modes in the waveguides. The indices used for different materials at different wavelengths are summarized in Table 2.1. The waveguide simulation is performed in Lumerical, and the mode profiles are simulated, as shown in Figure 2.2. For the 1550 nm waveguide design, the $TE_0$ mode has an effective mode index of 1.519 and an effective mode area of 2.05 $\mu m^2$, the $TM_0$ mode has an effective mode index of 1.469 and an effective mode area of 4.62 $\mu m^2$. For 780 nm waveguide design, the $TE_0$ mode has an effective mode index of 1.585 and an effective mode area of 0.32 $\mu m^2$, the $TM_0$ mode has an effective mode index of 1.508 and an effective mode area of 0.65 $\mu m^2$. In contrast to the normal highly confined waveguide mode, the waveguides designed for the ULLW process and in this thesis have a relatively loosely confined mode with a high aspect ratio. Optical mode confinement determines the propagation loss and bending limit of the waveguide structure. The reason for the high-aspect-ratio waveguide design is that the optical propagation loss mainly comes from scattering losses generated by the sidewall roughness during nitride etching processes, which is generally an order of magnitude larger than the surface roughness of the waveguide. By having a high-aspect-ratio waveguide, meaning that waveguide has a small thickness (down to 20 nm) and relatively large width (approximately 2 μm), the contribution of scattering loss is minimized as the majority of the optical mode sits in silicon dioxide claddings. It is worth noting that a low scattering loss is not sufficient to produce a low

optical loss in waveguides. Other main contributions include material absorption loss due to hydrogen impurities, waveguide bend loss, and scattering due to particles introduced during lithography and processing, which will be further discussed in the fabrication process in Section 2.5. Bend loss occurs when light traveling through a waveguide encounters a sharp bend or curve in the structure, and partial light radiates out owing to bending-induced modes. When the waveguide bends, several factors contribute to bend loss: mode mismatch, scattering, phase mismatch, material absorption and higher-order mode excitation. To simulate the bend loss, we define critical bend loss to be 1 dB/cm and simulate it in Lumerical mode analysis and include "bent waveguide" option. The bend loss simulation for waveguide designs at 1550 nm and 780 nm are shown in Figure 2.3. From the simulations, a minimum bend radius of approximately 300 μm is required to support the fundamental mode operation. The radius of the 1550 nm resonator is chosen to be 580 μm and 625 μm, and the radius of the 780 nm resonator is chosen to be 750 μm. The resonator bus-to-ring and ring-to-ring coupling coefficient simulations are performed in Lumerical FDTD for the 1550 nm and 780 nm resonators, as shown in Figure 2.4 and Figure 2.5.

| | 1550 nm | 780 nm |
|---|---|---|
| Top TEOS cladding index | 1.45 | 1.46 |
| Silicon nitride index | 1.95 | 1.99 |
| Bottom thermal oxide index | 1.445 | 1.455 |
| Top cladding thickness | 6 μm | 4 μm |

**Table 2. 1 Refractive indices used in Lumerical mode profile simulation.**

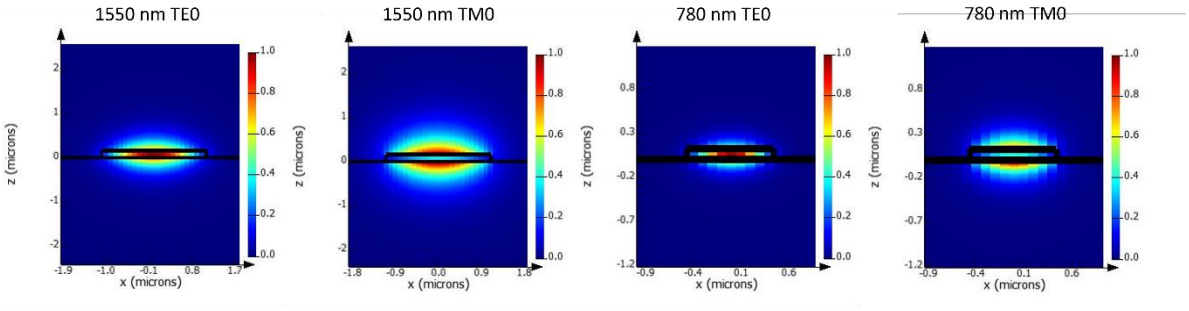


**Figure 2. 2 Simulated mode profiles in 175 nm core for λ = 1550 nm and 120 nm core for λ = 780 nm.**

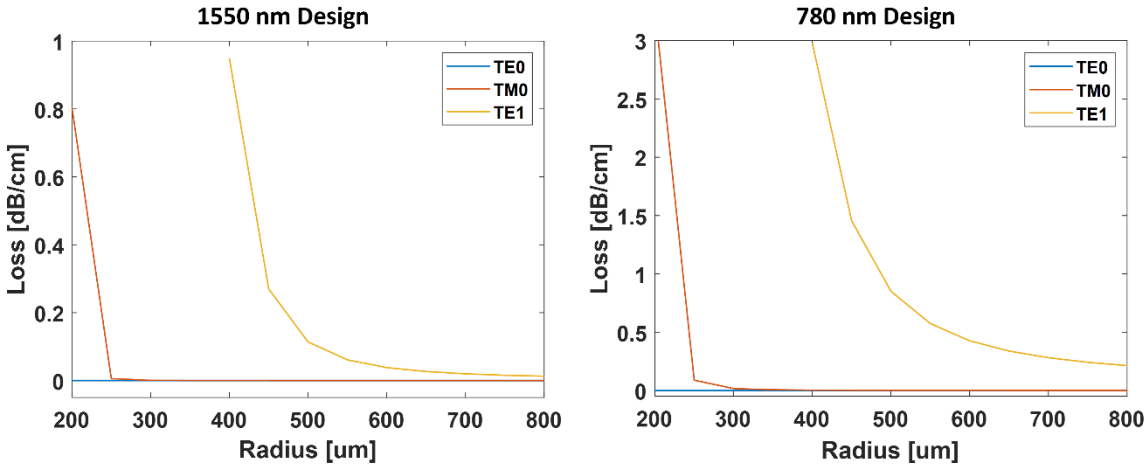


**Figure 2. 3 Bend loss simulation for resonator designs at λ = 1550 nm and λ = 780 nm.**

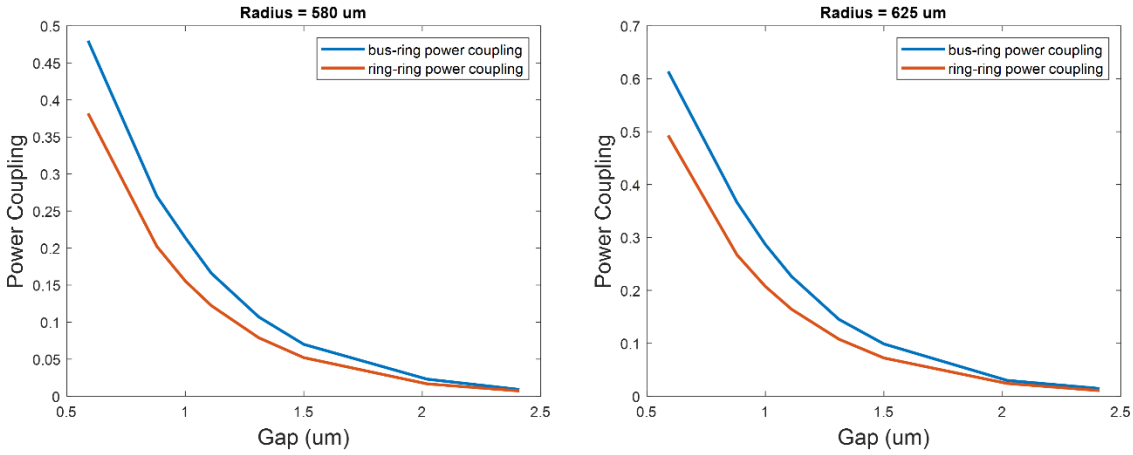


**Figure 2. 4 Coupling coefficients simulation for bus-ring and ring-ring at λ = 1550 nm.**

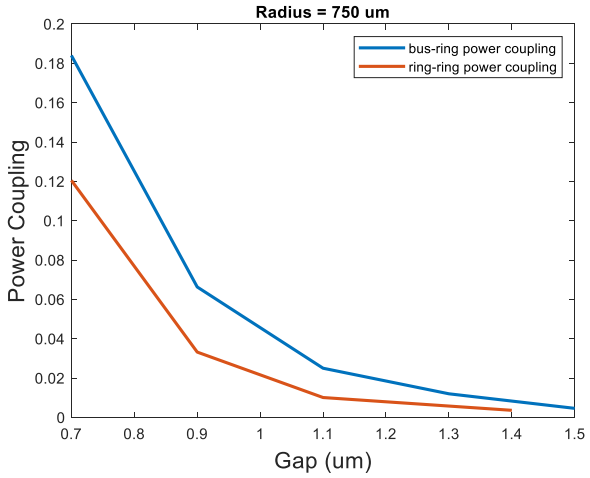


**Figure 2. 5 Coupling coefficients simulation for bus-ring and ring-ring at λ = 780 nm.**

### *2.3. Piezoelectricity and Stress-optic Simulation and Design*

As discussed in the introduction, compared to thermo-optic modulation and electro-optic modulation on silicon nitride waveguides, stress-optic modulation can benefit from minimal power consumption and moderate modulation speed without compromising the optical loss and wavelength transparency of the silicon nitride waveguide. Active control of the stress in the silicon nitride waveguide can be achieved by the deposition of thin film piezoelectric material on top of the waveguide, as shown in Figure 2.6. The stress-optic modulator developed in this dissertation is based on piezoelectric material PZT, which is the abbreviation of lead zirconate titanate with the chemical formula $Pb[Zr_xTi_{1-x}]O_3$ ($0 \leq x \leq 1$)). PZT exhibits a strong piezoelectric effect; for example, in comparison to other commonly used piezoelectric materials such as aluminum nitride (AlN) and zinc oxide (ZnO), PZT has an order of magnitude stronger effective transverse piezoelectric coefficient than that of AlN (AlN: $e_{31,f}$ = -1.02 $C/m^2$, ZnO: $e_{31,f}$ = -1.00 $C/m^2$, PZT: $e_{31,f}$ = -18.3 $C/m^2$ [8,51,55]).

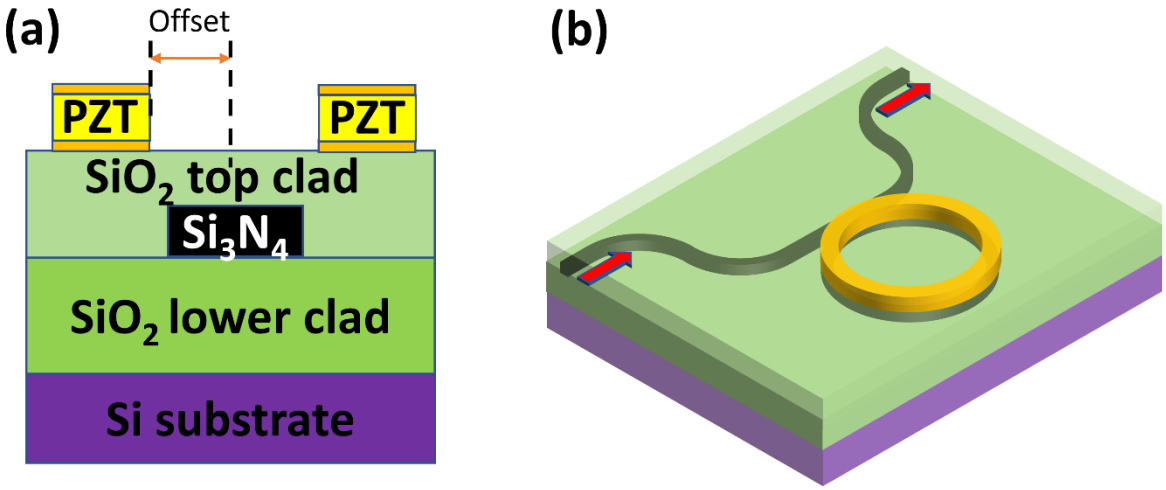


**Figure 2. 6 (a) Cross-section of the device, the PZT actuator is deposited on top of the waveguide with certain offsets to achieve the best performance without affecting**

**the optical loss. (b) Illustration of the stress-optic microresonator modulator, the PZT actuator (yellow) is monolithically integrated on top of the $Si_3N_4$ resonator (black) without under-etching process.**

As a piezoelectric material, PZT exhibits the piezoelectric effect, meaning the mechanical stress applied to the material will generate electrical charges and therefore electric fields. We utilize the converse piezoelectric effect, where the electric field applied across the PZT thin film causes it to expand in the direction of the electrical field and contract in the perpendicular direction. The stress/strain propagates underneath to the waveguide, resulting in a change and modulation of the effective refractive index of the optical mode. This process is illustrated in Figure 2.7.


**Figure 2. 7 Device working principle: converse piezoelectric effect and stress-optic effect.**

The stress-optic effect relation can be described as:

$$\Delta n_{ij} = -B_{ijkl}\sigma_{kl} \tag{2.1}$$

where $\Delta n_{ij} = n_{ij}-n_0 I_{ij}$, $B_{ijkl}$ and $\sigma_{kl}$ are the refractive index tensor, the stress-optical coefficient tensor and the stress tensor respectively. Therefore, the principle diagonal components of anisotropic refractive index tensor can be expressed as:

$$n_x = n_0 - B_1\,\sigma_x - B_2\,[\sigma_y + \sigma_z] \tag{2.2}$$

$$n_y = n_0 - B_1\,\sigma_y - B_2\,[\sigma_z + \sigma_x] \tag{2.3}$$

$$n_z = n_0 - B_1\,\sigma_z - B_2\,[\sigma_x + \sigma_y] \tag{2.4}$$

The change in refractive index and permittivity due to strain is given by:

$$\Delta\left(\frac{1}{n^2}\right)_i = \Delta\left(\frac{1}{\varepsilon_r}\right)_i = p_{ij}\,\varepsilon \tag{2.5}$$

where $\varepsilon_r$ is the relative permittivity, $\varepsilon$ is the strain and $p$ is the photo-elastic tensor. For $SiO_2$: $p_{11} = 0.121,\ p_{12} = 0.27, p_{44} = -0.075$; for Si: $p_{11} = -0.094, p_{12} = 0.017, p_{44} = -0.051$. The photo-elastic coefficient of silicon nitride are estimated to by same as $SiO_2$ [7].

Using these equations, the piezoelectricity and stress-optic simulation can be set up in COMSOL Multiphysic. The parameters used in simulation are summarized in the Table 2.2 below.

| | Young's modulus (GPa) | B1 ($m^2/N$) | B2 ($m^2/N$) | Piezoelectric constant (pm/V) | Poisson's ratio | Thermal expansion coeffi. (1/K) | Density ($kg/m^3$) |
|---|---|---|---|---|---|---|---|
| Si | 110 | \ | \ | \ | 0.19 | $2.5\times10^{-6}$ | 2330 |
| $SiO_2$ | 78 | $6.5\times10^{-13}$ | $4.2\times10^{-12}$ | \ | 0.17 | $3.5\times10^{-7}$ | 2203 |
| $Si_3N_4$ | 280 | $-3.5\times10^{-13}$ | $2.36\times10^{-12}$ | \ | 0.24 | $3.3\times10^{-6}$ | 3170 |
| PZT | 60.5 | \ | \ | $d_{31}$= -180<br>$d_{33}$ = 300 | 0.3 | $2\times10^{-6}$ | 7500 |

**Table 2. 2 Indexes used in piezoelectric simulation in COMSOL.**

Here, an example for the PZT stress-optic simulation for 1550 nm waveguide design is shown as in Figure 2.8. The top cladding thickness is chosen to be 6 μm and the PZT thickness, width and offset are chosen to be variable for simulation. The simulation set up is shown as in Figure 2.8 (a), the waveguide design and cladding thickness are simulated in

Lumerical and same as discussed in the microresonator design in the previous section. Figure 2.8 (b) and (c) shows the simulation results of stress distribution and actuator displacement under the condition of 15 µm PZT width, 2 µm PZT thickness, 3 µm PZT offsets and 10 V applied voltage.

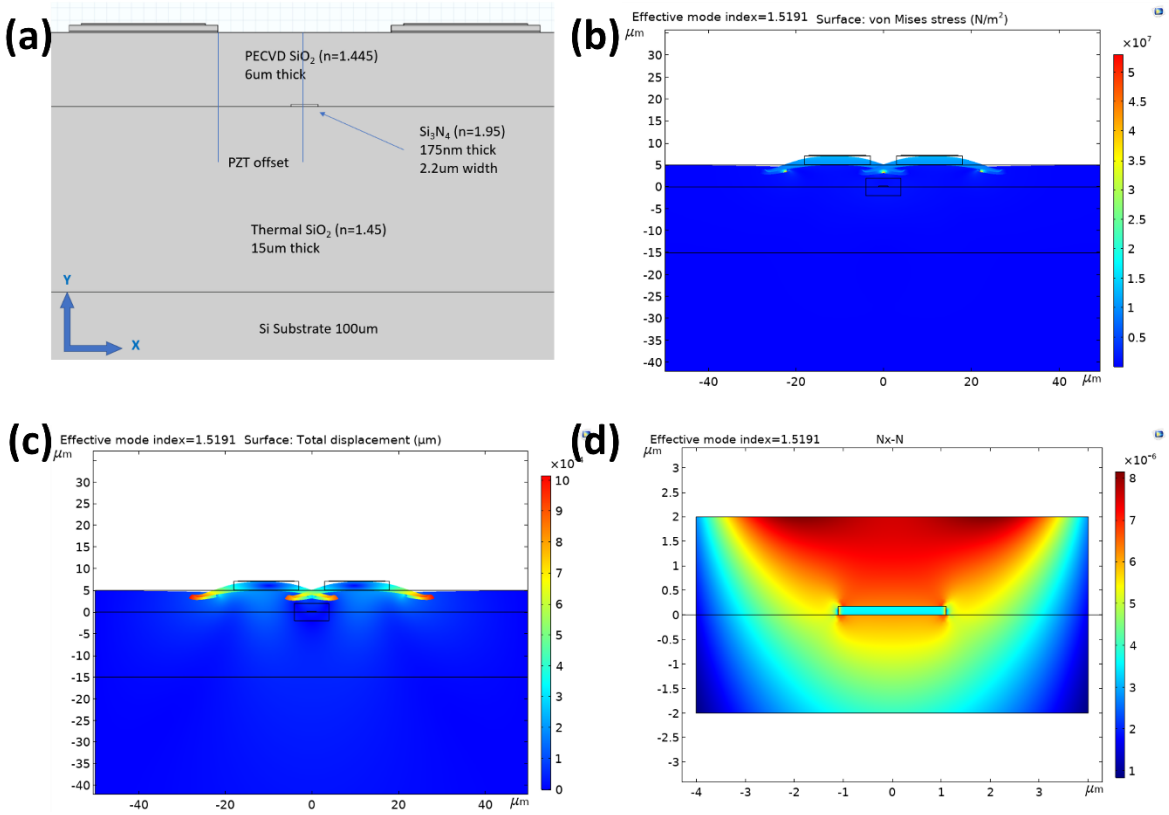


**Figure 2. 8 Piezoelectric and stress-optic simulation in COMSOL.**

By sweeping these parameters, the effective index change of the waveguide in relation to different PZT offsets, thickness and widths can be simulated and plotted, as shown in Figure 2.9. According to the simulation, the stress-optic effect becomes stronger with increased PZT thickness and PZT width, reaching a maximum with offsets around 2 µm to 3 µm. It is worth noting that, as depicted in Figure 2.9 (b), at the certain designs, the index change due

to the PZT stress-optic effect will exhibit a change in sign. This results in an opposite direction of static tuning of the PZT-actuated ring resonator, leading to red- and blue-shifted resonant wavelengths / frequencies. This phenomenon will be discussed and demonstrated in Chapter 3.2. The waveguide loss simulation with different waveguide cladding thickness and metal offset designs is shown as in Figure 2.10. Based on the simulation and fabrication process requirements, the top cladding thickness of the waveguide is set to 4 μm and 6 μm, the PZT thickness is set to 500 nm and 1 μm, the PZT offsets is set to 0 μm, 2 μm, and 5 μm, and the PZT width is set to 15 μm for the offset design and 30 μm for the no-offset design.

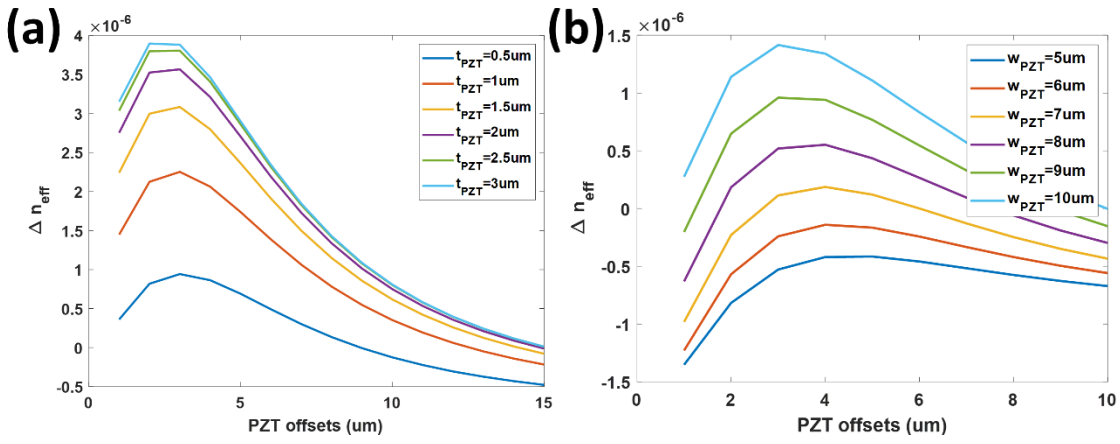


**Figure 2. 9 Simulation of effective index change with different (a) PZT offsets and thickness and (b) PZT offsets and widths.**

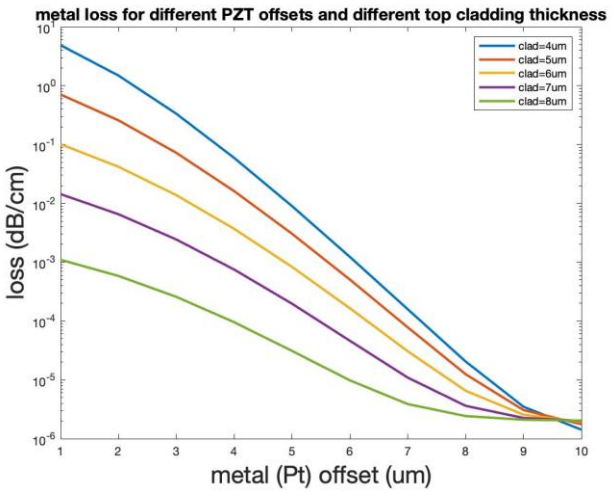


**Figure 2. 10 Simulation of waveguide loss with different cladding thickness and metal offset design.**

### *2.4. Fabrication Processes*

The fabrication processes are divided into two parts: the first part involves the fabrication of passive silicon nitride ultra-low loss waveguides fabrication at UCSB Nanofabricaiton facility and Honeywell Aerospace cleanroom foundry; the second part involves the fabrication of the PZT actuator at Army Research Laboratory.

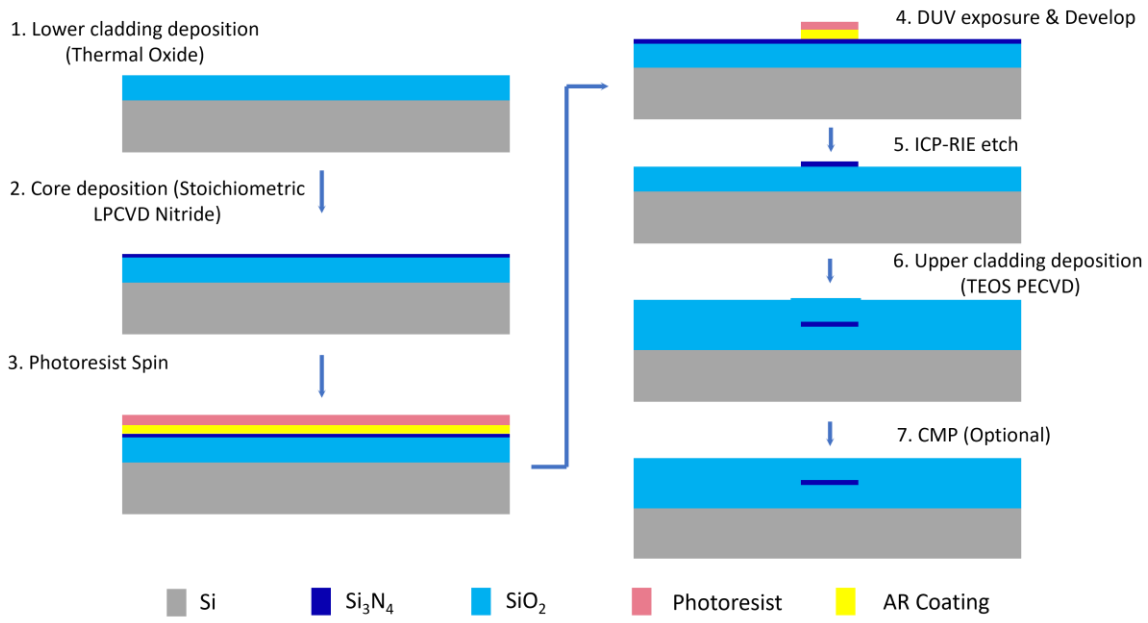


**Figure 2. 11 Passive silicon nitride waveguide fabrication process**

For the passive nitride processes, as depicted in Figure 2.11, the fabrication begins with a 15 μm thick lower cladding layer consisting of thermal silicon dioxide grown on a 1 mm thick, 100 mm diameter silicon substrate. Next, the stoichiometric silicon nitride layer is deposited by low-pressure chemical vapor deposition (LPCVD) atop the thermal oxide layer. LPCVD silicon nitride has low intrinsic stress compared to plasma-enhanced chemical vapor deposition (PECVD) and offers high uniformity across the wafer, which is crucial for depositing both very thin layer of nitride (for example 20 nm and 40 nm) and very thick layer (>400 nm) for frequency comb devices. Subsequently, positive photoresist UV6-0.8 and DUV anti-reflection (AR) coating resist DUV42-P are spin-coated onto the nitride layer and patterned with a photomask using 248 nm ASML DUV stepper exposure. The nitride core is etched with $CF_4/CHF_3/O_2$ gas in inductively coupled plasma (ICP) and reactive ion etching (RIE) etcher. Before upper cladding deposition, the wafer undergoes cleaning to

remove particle defects and achieve ultra-low optical loss. The cleaning steps include oxygen plasma ashing to remove byproducts during the dry chemical etching, NMP (N-Methylpyrrolidone) photoresist stripping at 80 ºC, and piranha (a mixture of sulfuric acid and hydrogen peroxide) cleaning at 110 ºC. Next, top cladding silicon dioxide is deposited in two steps by plasma enhanced chemical vapor deposition (PECVD) using tetraethylorthosilicate (TEOS) used as a Si precursor. TEOS is chosen for its reduced hydrogen content compared to silane [56]. The wafer then undergoes high-temperature annealing at 1050 °C for 7 hours and 1150 °C for 2 hours to further reduce absorption loss due to the hydrogen content in Si-H and N-H bonds [57]. Following upper cladding deposition, the wafer undergoes chemical-mechanical polishing (CMP) to planarize the surface for piezo actuator deposition.

The final patterned waveguides are characterized by scanning electron microscopy (SEM), as illustrated in Figure 2.12. Some fabrication variations occur when moving to smaller feature sizes and approaching the diffraction limit of ~ 250 nm for the DUV stepper. Atomic force microscopy (AFM) measurements are conducted to characterize waveguide edges and surfaces roughness. As shown in Figure 2.13 and Figure 2.14, the edge roughness of the waveguide is measured and calculated to be 1.04 nm, while the top of the waveguide (LPCVD silicon nitride) exhibits a surface RMS roughness of 468.8 pm, and the bottom of the waveguide (etched thermal oxide) exhibits a surface RMS roughness of 467.2 pm.

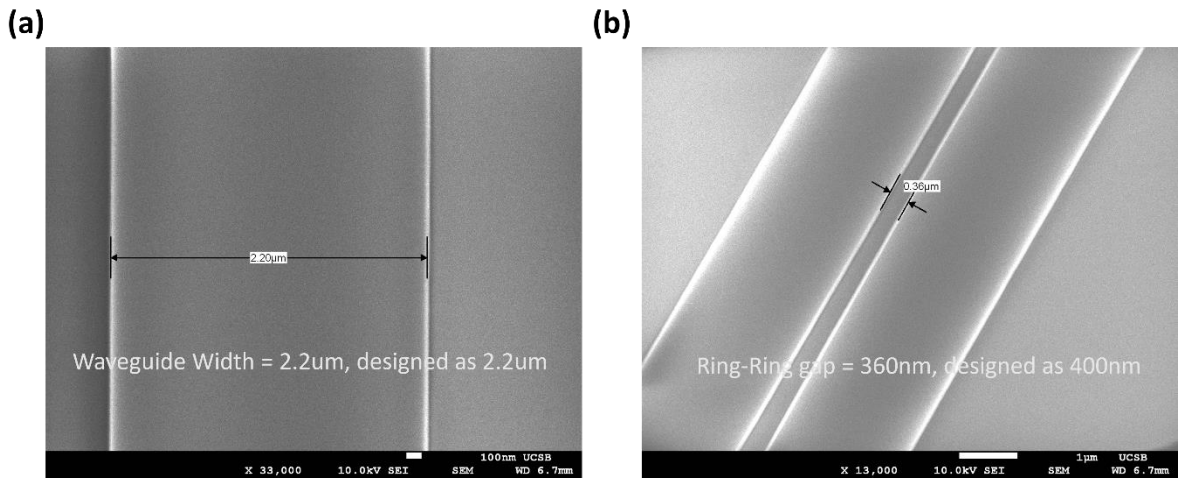


**Figure 2. 12 SEM images of fabricated waveguides.**

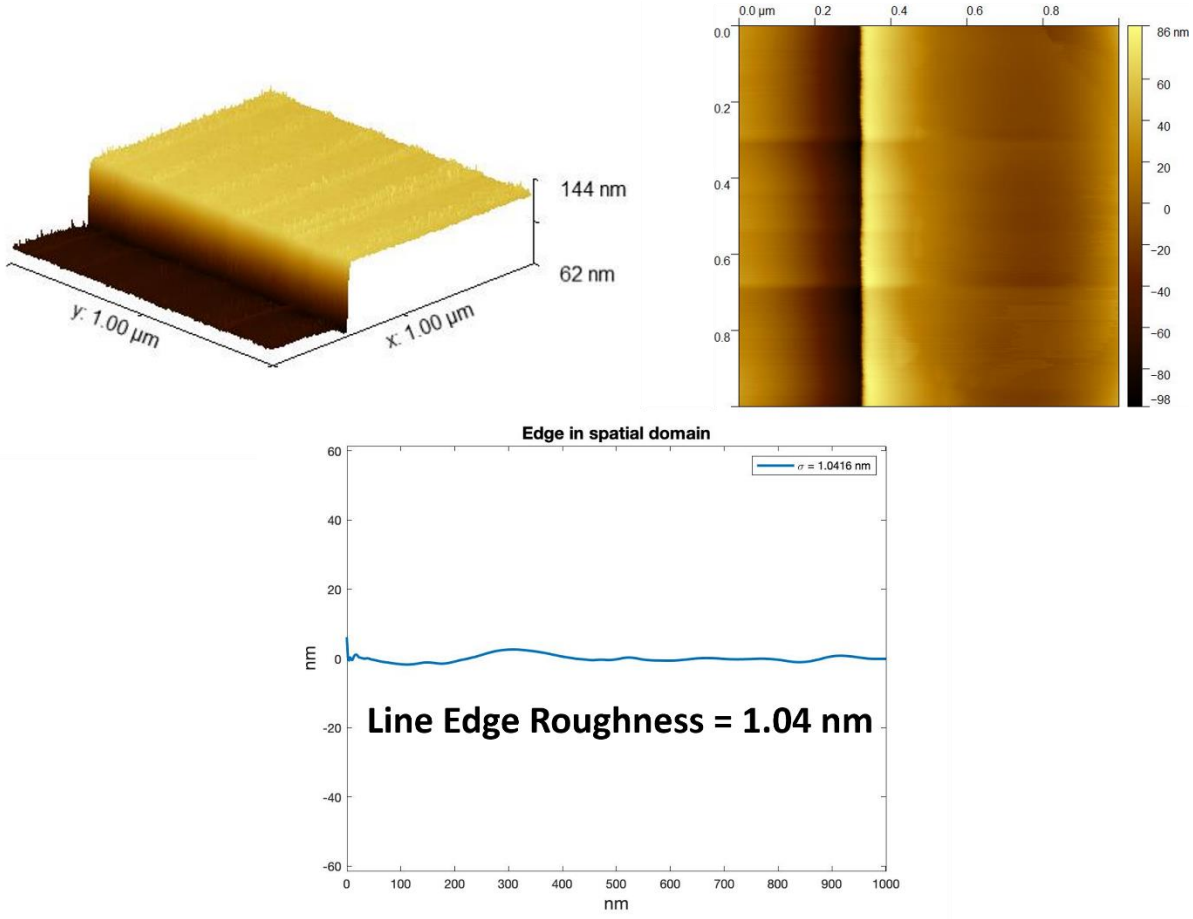


**Figure 2. 13 AFM measurement of waveguide edge.**

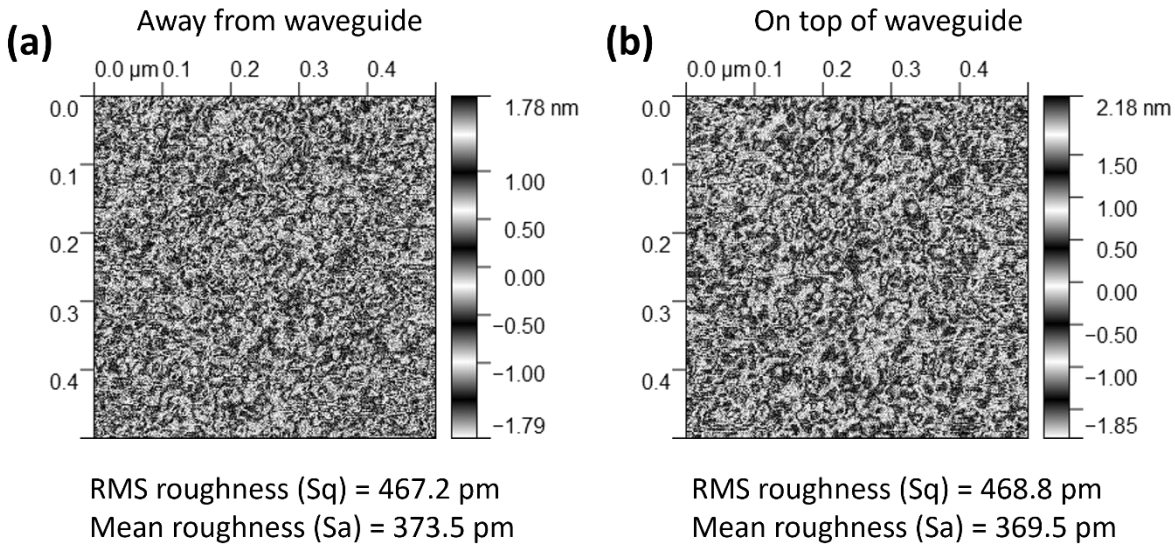


**Figure 2. 14 AFM measurement of waveguide top and bottom surfaces.**

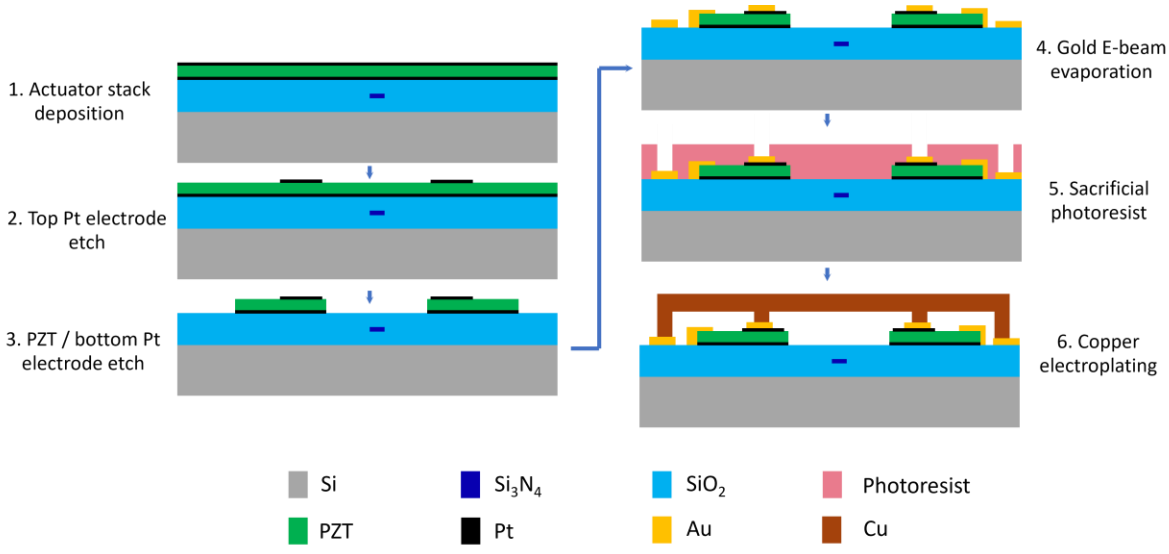


**Figure 2. 15 PZT fabrication process.**

For the PZT fabrication, as shown in Figure 2.15, the actuator stack consists of a sputtered 40 nm thick TiO2 adhesion layer, a sputtered 150 nm thick Pt bottom electrode, and a 500 nm (or 1 μm) thick layer of PZT (52/48 Zr/Ti ratio) deposited via chemical solution deposition (CSD), and the stack is capped with a sputtered 100 nm thick Pt top electrode. The PZT and Pt electrodes are patterned by argon ion milling. With the actuator patterned, electrical traces are evaporated and patterned through lift-off and consist of a Cr/Pt/Au stack with thicknesses of 20 nm, 20 nm, and 730 nm, respectively. To reduce resistivity and minimize gold coverage on the electrodes, a 10 μm thick copper layer is electroplated using photoresist molds and a sputtered copper seed layer. The photoresist molds and copper seed layer are removed with solvents to release the device. While the PZT material is capable of withstanding temperatures up to 700 degrees during processing, the procedure outlined above operates below 350 degrees due to the constraints imposed by metal processing, which have thermal limitations. It is possible to address this thermal constraint by incorporating extra contact pads, introducing an inter-layer dielectric, or modifying the metal material.

The final fabricated PZT-actuated $Si_3N_4$ resonator is shown in Figure 2.16 (a), and the detailed mask layout and layers is shown in Figure 2.16 (b). From the layer labeling, "SiN" is where the waveguide is patterned, "TopPt" are the locations that contain top electrode, "PZTmill" are the locations that contain PZT, "WetEtch" are the vias to the bottom electrode, "CPW" is where gold is evaporated, "PZTProt" is where the copper is anchored to the gold, and "Cu1" is electroplated copper (suspended in air if "PZTProt" is not patterned underneath).

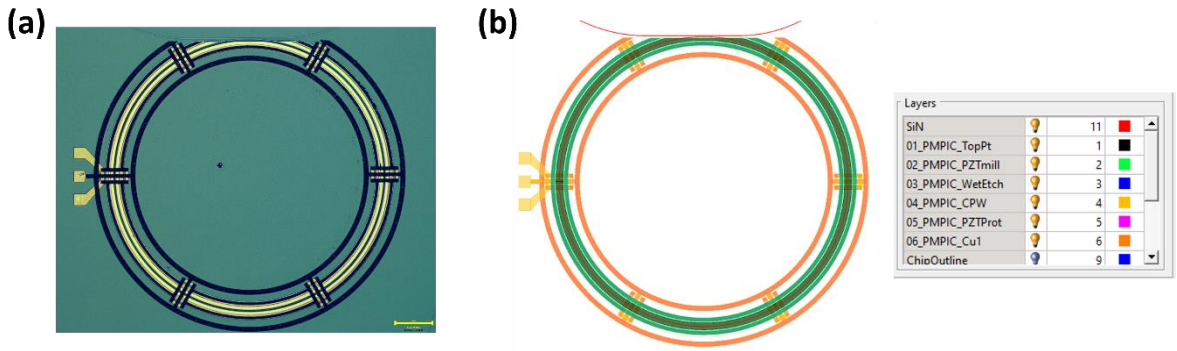


**Figure 2. 16 (a) Fabricated PZT-actuated silicon nitride ring modulator; (b) Mask layout and layer description of the device.**

An X-ray diffraction (XRD) scan is performed on the PZT materials, as shown in Figure 2.17, which is deposited by Radiant Technologies, Inc., and has a composition along the morphotropic phase boundary where the peak piezoelectric coefficients are observed [58]. The PZT contains random crystallographic orientation, as can be seen from the XRD. It's possible that piezoelectric performance, and thus modulator performance, could be improved by controlling orientation to achieve predominantly (100)-oriented PZT [58]. No other detrimental X-ray signatures such as pyrochlore are observed.

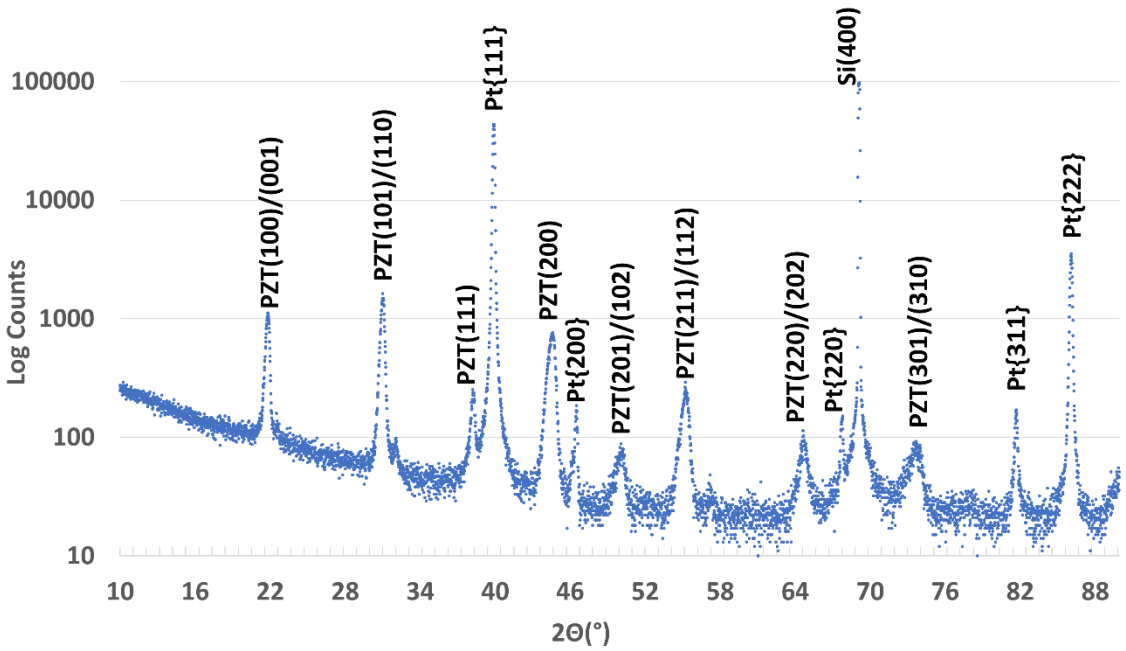


**Figure 2. 17 X-ray diffraction (XRD) scan of the PZT material.**

# 3. Characterization of PZT Modulator

## *3.1 Resonator Quality Factor and Loss Measurement*

A high quality factor (Q) resonator requires accurate characterization with an optical frequency standard [59]. This is achieved using an RF-calibrated unbalanced fiber-based Mach-Zehnder interferometer (MZI) as a frequency ruler. Other quality factor measurement methods, such as cavity ring-down measurement [60], will not be discussed in this thesis, as the devices' Q values in this thesis are not ultra-high. The MZI's free spectral range (FSR) can be calibrated using single-sideband laser sweeping measurement [61] or the cavity optical frequency discrimination (OFD) method [9], which will be discussed in Chapter 4.

As discussed in the previous section, there are two types of resonators and PZT ring modulators characterized in this section: one for 1550 nm design and one for 780 nm. For the 1550 nm resonator design, as illustrated in Figure 3.1 (c), a fiber laser with piezo frequency tuning is modulated by a waveform generator. The scanned laser signal passes through both the MZI with a calibrated FSR of 5.87 MHz and the resonator under test. Both optical signals are measured with a balanced photodetector and fed to an oscilloscope for processing along with the ramp signal. As shown in Figure 3.1 (b), plotted from the oscilloscope, the full-width-at-half-maximum (FWHM) of the PZT-actuated resonator resonance is measured to be 54.52 MHz at 1550 nm using the MZI with calibrated 5.87 MHz FSR as an accurate frequency reference. The measurement yields a 7.1 million intrinsic Q, a 3.6 million loaded Q, and a corresponding 0.03 dB/cm waveguide loss. The calculation of Q factor and propagation loss is described below.

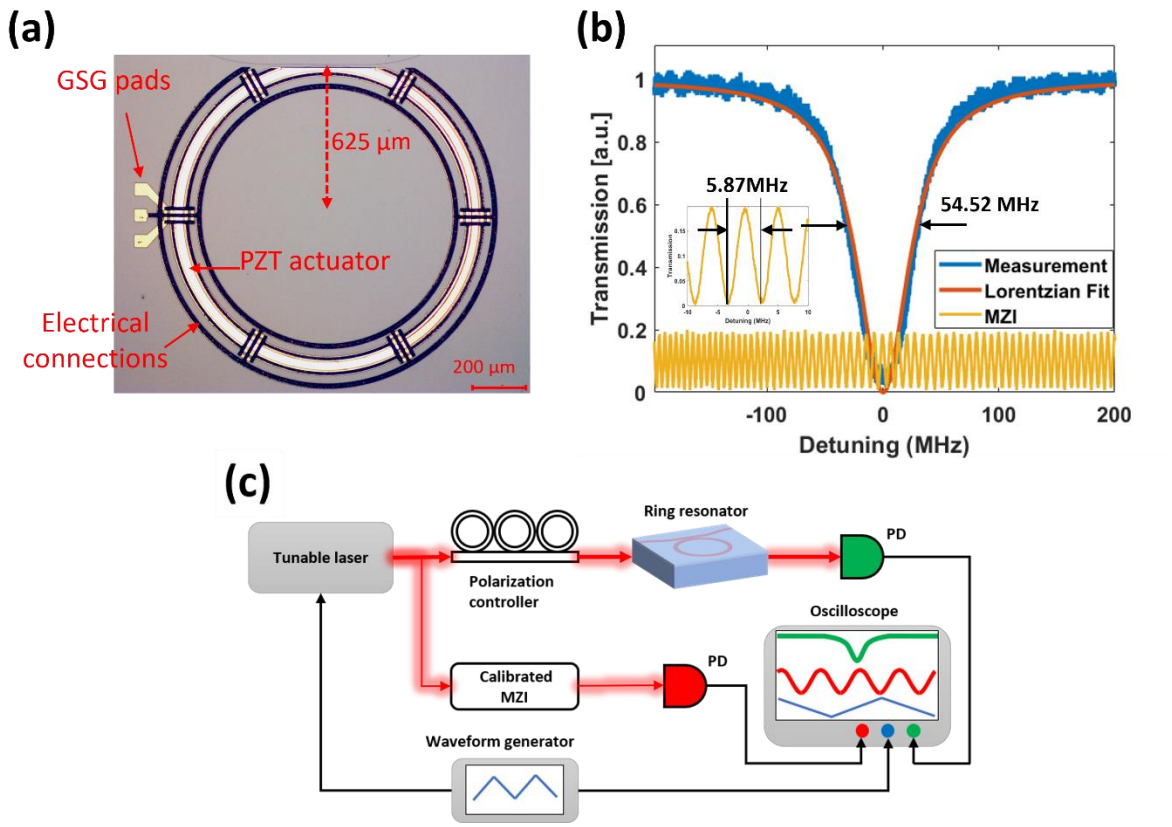


**Figure 3. 1 (a) The optical image of the fabricated PZT modulator resonator. (b) The Q measurement of the 1550 nm resonator. The calibrated MZI with a 5.87 MHz FSR acts as a frequency ruler (yellow trace) to measure the FWHM of the resonator resonance (blue trace). (c) System diagram of the quality factor measurement with the calibrated MZI.**

From the couple mode equations [62]:

$$\frac{da}{dt} = \left(-i\omega + \frac{\gamma}{2}\right) a + i\sqrt{\gamma_c} S_{in} \tag{3.1}$$

$$S_{out} = S_{in} + i\sqrt{\gamma_c} a \tag{3.2}$$

The measured resonance shape can be fitted to a Lorentzian profile with the transmission expressed as:

$$T = \left|\frac{S_{out}}{S_{in}}\right|^2 = \left|\frac{i\omega + (\gamma_{in} - \gamma_c)/2}{i\omega + (\gamma_{in} + \gamma_c)/2}\right|^2 \quad (3.3)$$

where $\gamma_{in} = c\alpha/n_g$ is the intrinsic linewidth and $\gamma_c = c\kappa^2/n_g L$ is the extrinsic linewidth. $n_g$ is the group index of the waveguide and α is the propagation loss. $L = 2\pi R$ is the perimeter of the ring resonator and $\kappa^2$ is the power coupling coefficient.

Through Lorentzian fitting, two parameters can be extracted: one corresponds to $\gamma_{in}$ and other corresponds to $\gamma_c$. To differentiate them, multiple devices with the same resonator design but different coupling gaps are measured. Because the intrinsic linewidth $\gamma_{in}$ does not change while the extrinsic linewidth $\gamma_c$ (bus coupling rate) varies due to different coupling conditions, both $\gamma_{in}$ and $\gamma_c$ can be identified.

The intrinsic and extrinsic quality factor of the device and the propagation loss α can be calculated [63,64]:

$$Q_{in} = \frac{\omega}{\gamma_{in}} = \frac{2\pi n_g}{\lambda_{res}\alpha} \quad (3.4)$$

$$Q_{ex} = \frac{\omega}{\gamma_c} = \frac{2\pi n_g L}{\lambda_{res}\kappa^2} \quad (3.5)$$

The loaded quality factor can be expressed as:

$$Q_{Load} = \frac{\lambda_{res}}{FWHM} = \frac{\omega}{\gamma_{in} + \gamma_c} = \frac{2\pi n_g L}{\lambda_{res}}\left(\alpha L + \kappa^2\right)^{-1} \quad (3.6)$$

As discussed in Chapter 2, the effective index changes as a function of PZT offset and thickness is summarized in Figure 3.2 (a), indicating that a 2 μm offset results in the largest index change. Fabricated resonators with different PZT offsets are tested for Q and loss, as shown in Figure 3.2 (b). When the PZT actuator is located directly above the waveguide, the Q and the loss are reduced by approximately 20% compared to when the PZT actuator is not present. However, with the PZT actuator laterally offset by 2 μm from the waveguide and

fabricated on top of the upper oxide cladding, the reduction in loss and Q are only under a few tenths of a dB.

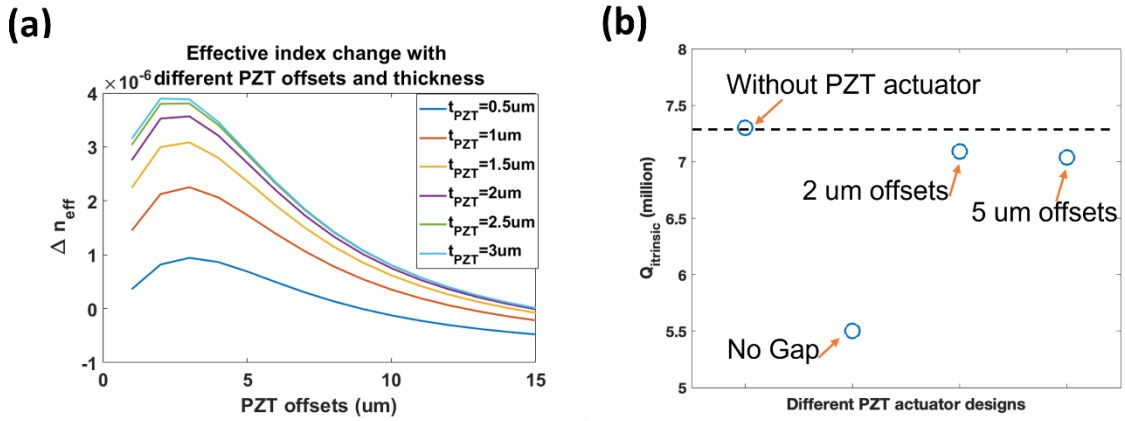


**Figure 3. 2 Summary of the simulation data, showing that the 2 µm offset results in the largest strain effect. (b) The measurement of the fabricated devices agrees with the simulation.**

Similarly, the Q measurement of the 780 nm resonator is conducted using the same method as in Figure 3.1 (c). The laser source is a 780 nm distributed Bragg reflector (DBR) laser, the photodetectors are adjusted for the visible range, and the unbalanced fiber MZI is designed for visible wavelengths and calibrated to be 24 MHz at 780 nm. As illustrated in Figure 3.3, for a 780 nm resonator design with a coupling gap of 1.15 µm and a ring radius of 750 µm, the average loaded Q is 2.48 Million with a standard deviation of 0.24 from measurements of 6 devices. The average intrinsic Q is 12.08 Million with a corresponding loss of 4.3 dB/m at 780 nm. The resonance exhibits an extinction ratio (ER) of 3.1 dB and a FWHM linewidth of 171 MHz.

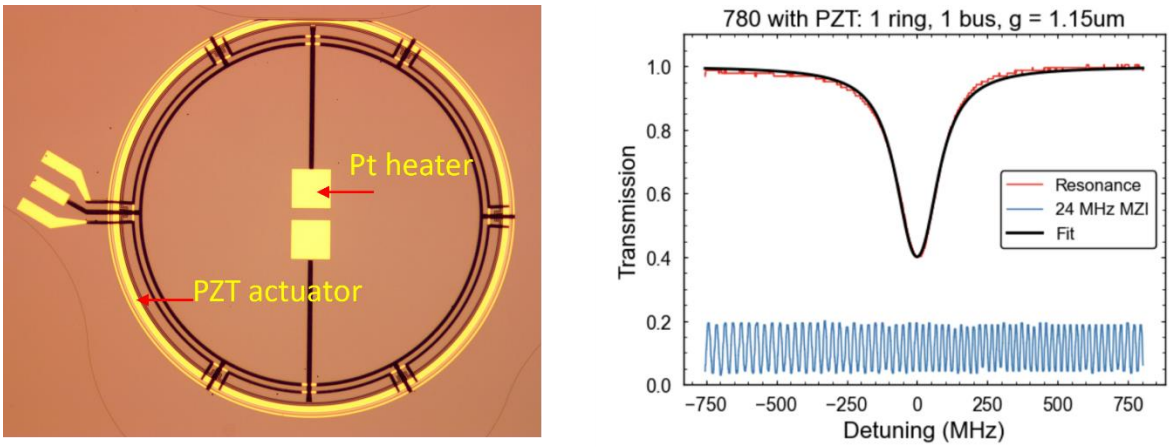


**Figure 3. 3 The Q measurement of the 780 nm resonator. The calibrated MZI with a 24 MHz FSR acts as a frequency ruler (blue trace) to measure the resonator resonance (red trace).**

### *3.2 PZT Actuator Static Tuning Measurement*

Static tuning of the PZT actuator, which shifts the ring resonance as a function of applied bias voltage, is shown in Figure 3.4 (a). The electric field is applied to the PZT actuator electrodes using a DC probe, including strain through the piezoelectric effect, thereby changing the waveguide refractive index. For the 1550 nm PZT modulator, we measure a 14 dB ER across the full 4 GHz tuning range, as the applied voltage is varied from 0 V to 20 V. Nonlinearity and hysteresis are observed in static tuning by sweeping the DC bias voltage in both forward (from -20 V to 20 V) and backward (from 20 V to -20 V) direction, as shown in Figure 3.4 (b), due to the ferroelectric nature of PZT [7,65]. PZT is a ferroelectric material with a spontaneous electric polarization. When polarized by an electric field, PZT retains that polarization when the field is removed. The average tuning coefficient is calculated to be -1.3 pm/V or -162 MHz/V. The half-wave voltage-length product $V_\pi L$ of

the modulator is calculated to be 43 V·cm, and $V_\pi L\alpha$, taking into account the waveguide loss, is 1.3 V·dB, comparable to state-of-art phase modulators [7,46,66]. We measure the static power consumption to be 20 nW at 20 V bias voltage using a precision source and measure unit (Keysight B2902A) with 100 fA measurement resolution, determined by the leakage current through the PZT actuator. It is worth noting that with a 500 nm PZT thickness, the devices have a dielectric breakdown voltage of approximately 30-40 V, which can be improved with a thicker PZT thickness and optimized actuator design. The RF power dissipation can be calculated by:

$$P = CV^2 f = \frac{\varepsilon_r \varepsilon_o wl}{t} V^2 f \tag{3.7}$$

where $w$, $l$ and $t$ are the electrode width, length and PZT thickness, $f$ is the RF driving frequency and $V$ is the applied voltage. The average capacitances measured for the 1550 nm PZT modulator and 780 nm modulator are 600 pF and 700 pF.

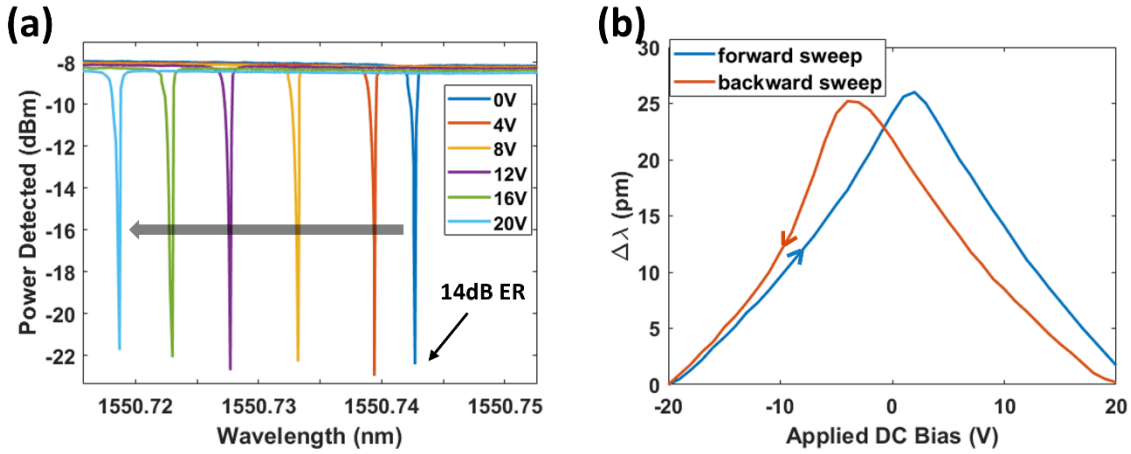


**Figure 3. 4 The optical transmission spectrum of the static tuning of the device. The resonance has a 14 dB extinction ratio (ER) across the 4 GHz tuning range. (c) The linear fitting of the tuning curve corresponds to -1.3 pm/V or -162 MHz/V tuning coefficient.**

Similarly, static tuning is also measured for the 780 nm PZT modulator. As described in the previous section, the top cladding thickness of 780 nm design is decreased from 6 μm to 4 μm compared to the 1550 nm design, therefore we expect an increase in stress-optic tuning strength. For the 780 nm run, a metal heater utilizing the bottom electrode platinum layer as the heating element is shown as in Figure 3.3, and the thermal tuning is measured and shown in Figure 3.5 with a tuning coefficient of 87.4 MHz/mW. The Pt heater is located approximately 100 μm away from the nitride waveguides. The static tuning of the 780 nm PZT actuators is measured for different PZT offset designs, as shown in Figure 3.6. For no offset design actuators, the tuning coefficient is measured to be about 480 MHz/V, while for the 2 μm offset design, the tuning coefficient is measured to be about -150 MHz/V. The difference between tuning directions is due to the physical process of the stress-optic effect from the two designs. When there is no offset, the PZT film sits on top of the waveguide, and the strain will propagate underneath, acting as a "pulling" force to the waveguide, whereas when there is an offset in the middle of the two PZT films, the strain that propagates underneath will act as a "squeezing" force to the waveguide. The dielectric breakdown voltage for the 780 nm PZT modulator is measured to be around 70 V, mainly due to a thicker PZT film of 1 μm compared to 500 nm of the 1550 nm design.

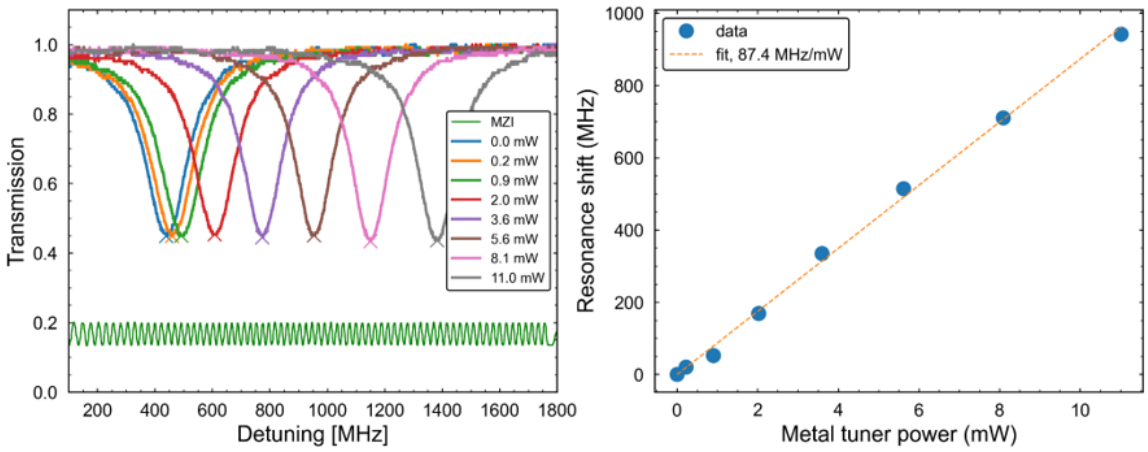


**Figure 3. 5 Thermal tuning of the Pt heater located inside the PZT actuator.**

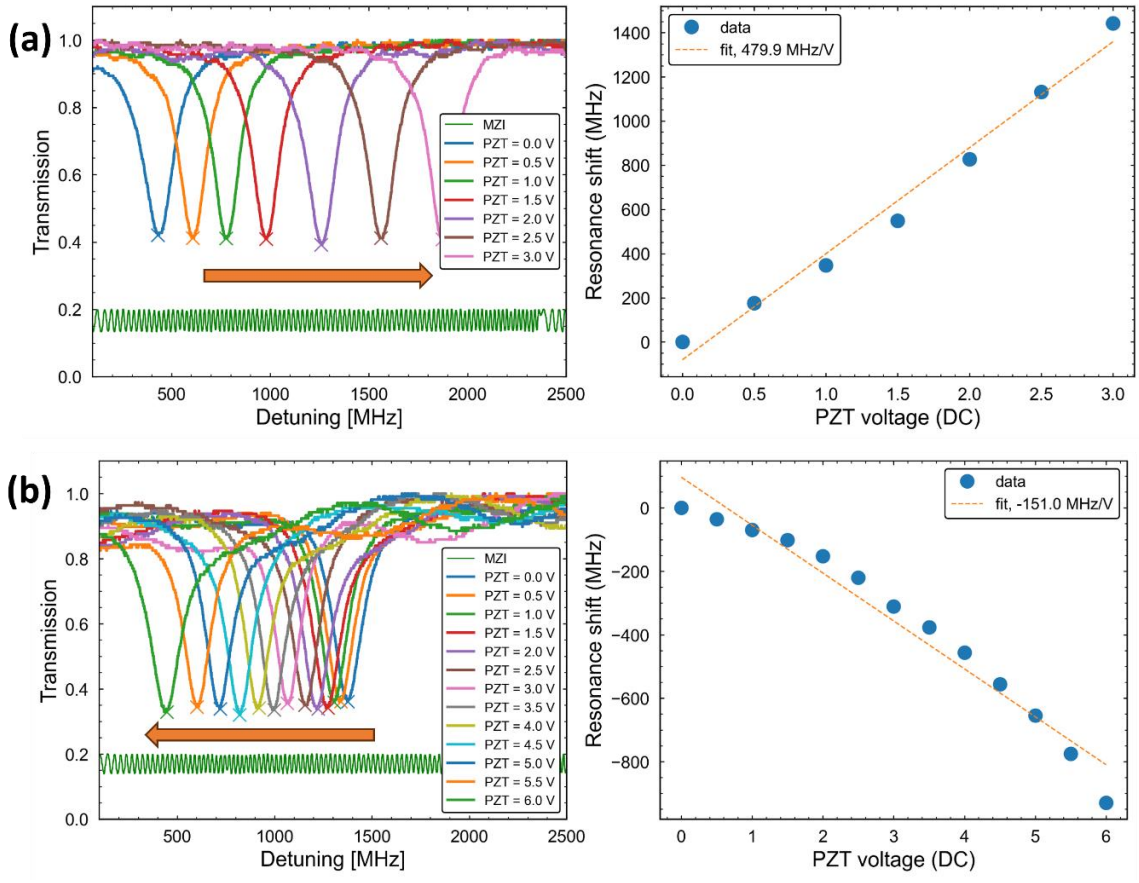


**Figure 3. 6 PZT static tuning of (a) No PZT offset design with 480 MHz/V tuning strength and (b) 2 µm PZT offset design with -150 MHz/V tuning strength.**

### *3.3 Modulator Bandwidth Measurement*

The small-signal electrical-to-optical modulation response $S_{21}$ for the 1550 nm PZT modulator is measured using a semiconductor diode laser (Velocity TLB-6730) modulated to the FWHM point of the resonance, a calibrated fast photodetector (Thorlabs DET01CFC, bandwidth 1.2 GHz), and a vector network analyzer (Keysight N5247B PNA-X). The measurement set-up is illustrated in Figure 3.7 (a).

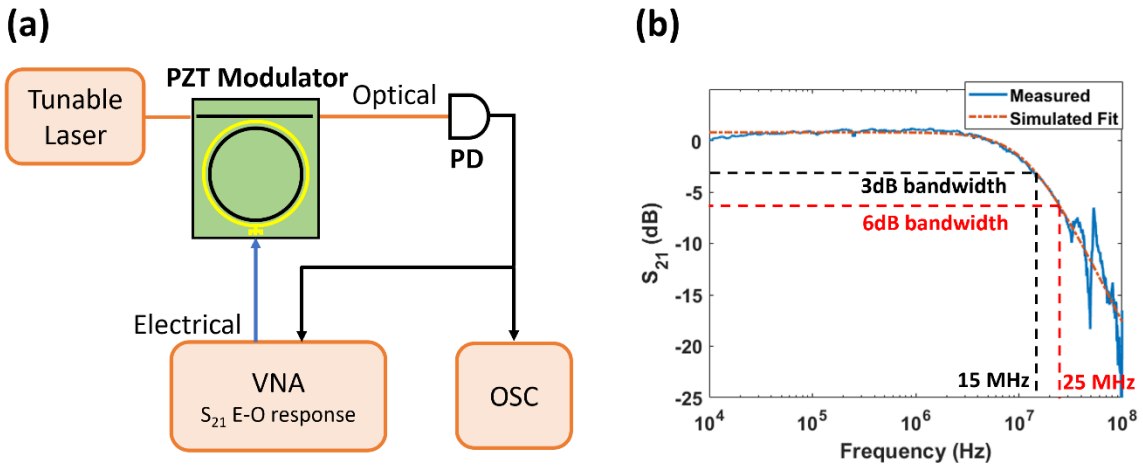


**Figure 3. 7 (a) The experimental diagram for small-signal electrical-to-optical frequency response measurements. (b) The frequency response (S21) indicates that the 3-dB and 6-dB modulation bandwidth is 15 MHz and 25 MHz, respectively.**

As depicted in Figure 3.7 (b), the 3-dB and 6-dB modulation bandwidths are 15 MHz and 25 MHz, respectively. Since the network analyzer measures the photocurrent of the detector, describing the optical response in terms of detected optical power, the 3-dB bandwidth of the detected optical power equals the measured 6-dB bandwidth of the detected photocurrent, which is 25 MHz.

To study the bandwidth limitations and performance, a small-signal model is developed for the PZT ring modulator. The dynamics are described by the coupled-mode theory for a microresonator modulator [67]:

$$\frac{da}{dt} = (i\omega_r - \frac{1}{\tau})a - i\mu S_{in} \tag{3.8}$$

$$S_{out} = S_{in} - i\mu a \tag{3.9}$$

Here, $S_{in}$ is the optical continuous wave (CW) input to the resonator, $S_{out}$ is the time-varying bus output, and $a$ represents the energy stored inside the resonator. $\tau$ is the effective photon lifetime, given by $1/\tau = 1/\tau_{ex} + 1/\tau_{in}$, which is also the effective optical linewidth of the resonator. $\tau_{ex}$ represents the amplitude decay time constant due to bus-ring coupling, and $\tau_{in}$ represents the amplitude decay time constant due to cavity intrinsic loss. $\omega_r$ is the on-resonance frequency of the resonator, and $\mu$ is the coupling coefficient between the bus and the ring where $\mu^2 = 2/\tau_{ex}$.

In steady state, considering input of $S_{in} = S_{in0}e^{i\omega_{in}t}$, $a = a_0 e^{i\omega_{in}t}$ and $S_{out} = S_{out0}e^{i\omega_{in}t}$ where $\omega_{in}$ is the laser carrier frequency

$$a_0 = \frac{-i\mu}{i\Delta\omega + \frac{1}{\tau}} S_{in0} \tag{3.10}$$

$$S_{out0} = \frac{i\Delta\omega + \frac{1}{\tau} - \frac{2}{\tau_e}}{i\Delta\omega + \frac{1}{\tau}} S_{in0} \tag{3.11}$$

where $\Delta\omega = \omega_{in} - \omega_r$ is the laser detuning frequency.

Since the transmission T is proportional to the $\left|\frac{S_{out}}{S_{in}}\right|^2$ and hence $\left|\frac{S_{out0}}{S_{in0}}\right|^2$, therefore, from Equation 3.11 the transmission T can be characterized as:

$$T = \left| \frac{i(\omega_{in} - \omega_r) + \frac{1}{\tau_{in}} - \frac{1}{\tau_{ex}}}{i(\omega_{in} - \omega_r) + \frac{1}{\tau}} \right|^2 \tag{3.12}$$

Now considering small-signal modulation, $a = a_0(t)e^{i\omega_{in}t}$, by substituting Equation 3.8, we arrive at:

$$\frac{da_0(t)}{dt} = -\left(i\Delta\omega + \frac{1}{\tau}\right)a_0(t) - i\mu S_{in0} \tag{3.13}$$

In dynamic small-signal domain we have $\Delta\omega = \Delta\omega_0 + \delta\Delta\omega(t)$ and $a = a_0 + \delta a(t)$, therefore by deriving Equation 3.13 and consider first order AC components, we arrive at:

$$\frac{d}{dt}(\delta a(t)) = -\left(i\Delta\omega + \frac{1}{\tau}\right)\delta a(t) - a_0\delta\Delta\omega(t) \tag{3.14}$$

We can treat the small perturbation as $\delta\Delta\omega(t) = \beta e^{i\omega_s t}$ and $\delta a(t) = \delta a_0 e^{i\omega_s t}$, where β and $\delta a_0$ are the corresponding amplitude constants, and $\omega_s$ is the modulation frequency from the VNA, and we arrive at:

$$\delta a_0 = \frac{-a_0\beta}{i(\Delta\omega+\omega_s)+\frac{1}{\tau}} \tag{3.15}$$

Therefore, $S_{21}$ is proportional $|\delta S_{out}|^2$ and hence $|\delta a_0|^2$ if we consider the magnitude only:

$$S_{21} \propto \left|\frac{a_0\beta}{i(\Delta\omega+\omega_s)+\frac{1}{\tau}}\right|^2 \tag{3.16}$$

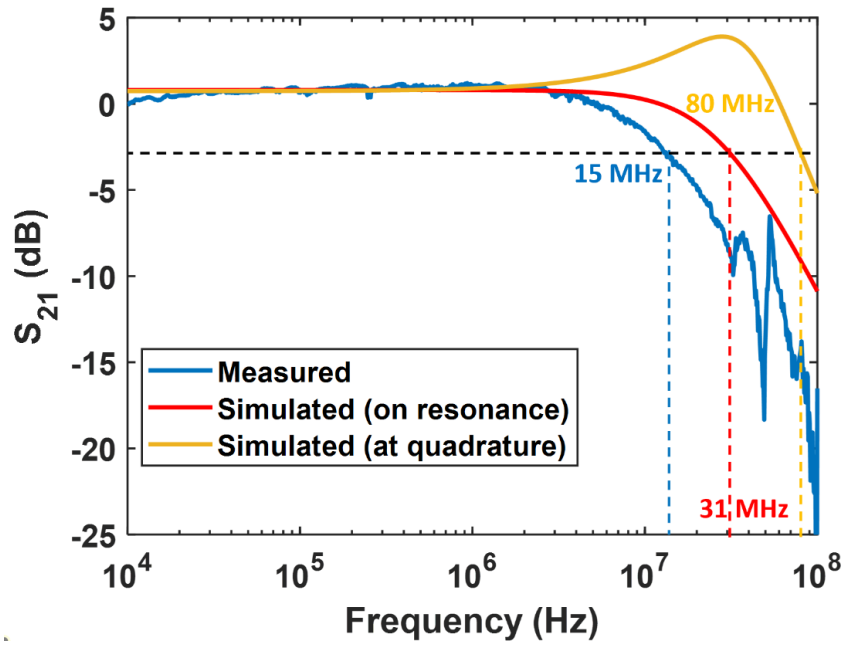


**Figure 3. 8 Optical response calculation at different detuning point (red and orange curve) with measured optomechanical response S21 (blue curve).**

By plotting the calculated $S_{21}$ as shown in Figure 3.8, the optical bandwidth enhancement expected from operating at the quadrature point of resonance yields the yellow curve, whereas on-resonance operation yields the red curve. These calculations estimated an 80 MHz optical bandwidth for at quadrature operation and a 31 MHz optical bandwidth for on-resonance operation, both of which are larger than what we have measured. The peak in the frequency response (yellow trace) occurs due to the constructive interference between the detuned input laser frequency and the coupled light preexisting inside ring resonator and oscillating at its natural frequency [68–70]. To study the bandwidth limitation and performance, we model the system into three parts: electrical, PZT opto-mechanical and

optical, as illustrated in Figure 3.9. The measured frequency response can be decoupled into three parts and expressed as:

$$\frac{1}{f_{measured}^2} = \frac{1}{f_e^2} + \frac{1}{f_{OM}^2} + \frac{1}{f_o^2} \tag{3.17}$$

where electrical response is $f_e = \frac{1}{2\pi\tau_e} = \frac{1}{2\pi RC}$ and optical response is $f_o = \frac{1}{2\pi\tau_{ph}} = \frac{c}{\lambda Q}$.

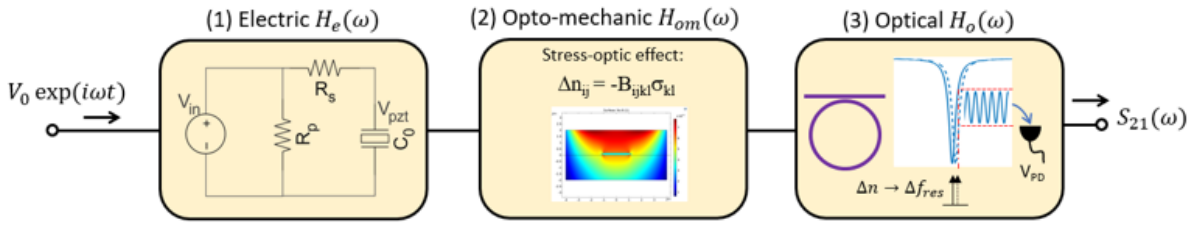


**Figure 3. 9 Modeling of the frequency response system divided into (1) electric, (2) opto-mechanic and (3) optical response.**

The PZT actuator capacitance is measured to be around 600 pF, and the resistance is 2.2 Ω, yielding an electrical bandwidth of 120 MHz. Considering only the electrical RC time constants and quadrature point optical bandwidth cascaded, the effective bandwidth is $\frac{1}{f^2} = \frac{1}{f_e^2} + \frac{1}{f_o^2}$, which yields an effective bandwidth of 66 MHz. Performing the same calculation for on-resonance operation yields 30 MHz, both of which are higher than the measured 15 MHz bandwidth. Incorporating a time constant for the optomechanical stress-optic actuator and using the RC time constant and quadrature yellow curve, we calculated the bandwidth of the optomechanical stage to be approximately $f_{OM}$ = 15 MHz, according to Equation 3.17. This calculation points to our piezo actuator being the current bandwidth limitation. For optical bandwidth, with a higher Q or narrower resonator linewidth, the modulator is more

susceptible to index variation, which will enhance the modulation depth but, on the other hand, will limit the optical bandwidth.

For the 780 nm PZT modulator, $S_{21}$ is measured in a similar setup, as shown in Figure 3.10. The optical 3-dB bandwidth (6-dB electrical bandwidth) is 10 MHz, and the out-of-phase bandwidth is about 16 MHz. A positive phase value for $S_{21}$ indicates that the output phase leads the input phase, and a negative value indicates that the output phase lags the input phase.

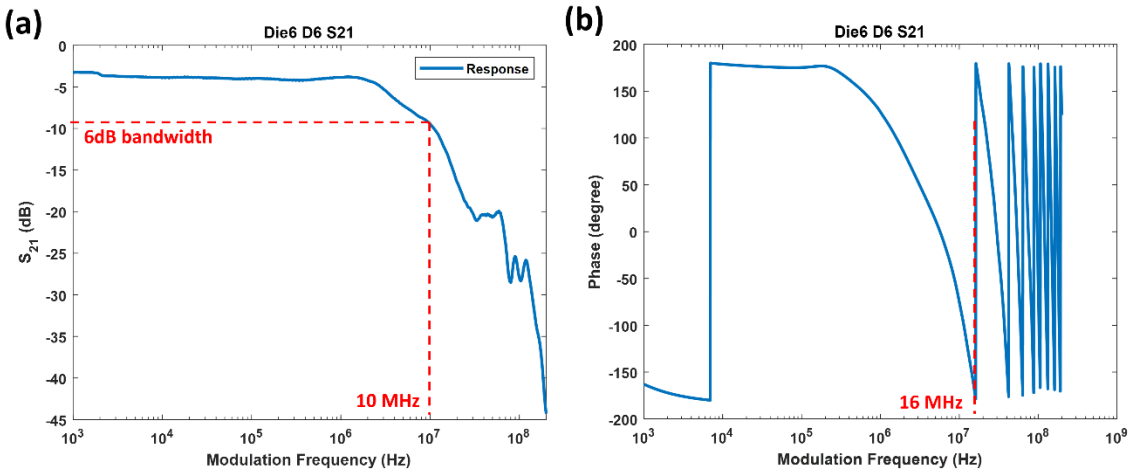


**Figure 3. 10 The frequency response ($S_{21}$) (a) amplitude information and (b) phase information of the 780 nm PZT modulator.**

### *3.4 Modulator Linearity Measurement*

The modulator linearity is characterized by measuring the third-order intermodulation distortion (IMD3) spurious free dynamic range (SFDR) [71–73]. The SFDR is a common measure of modulator linearity and is defined as the signal level at which the noise floor and power of the third order distortion tone are equal. The two-tone test is performed by

applying two closely placed RF signals to the modulator and measuring the intermodulation components at the optical output using an electrical spectrum analyzer (ESA). The measured noise floor is -97.9 dBm/Hz at 1 MHz and -110.1 dBm/Hz at 10 MHz. IMD3 SFDR values of 65.1 dB·Hz$^{2/3}$ and 73.8 dB·Hz$^{2/3}$ are measured at 1 MHz and 10 MHz, respectively, as shown in Figure 3.11 (c) and (d).

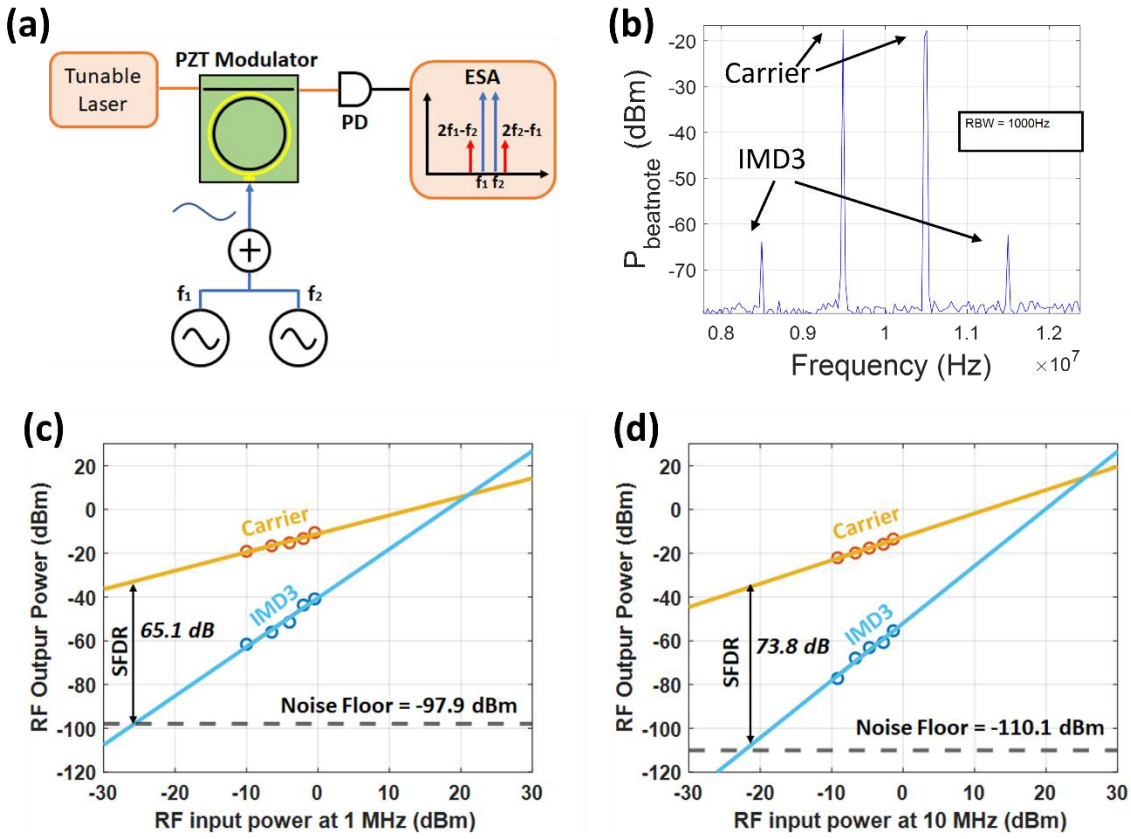


**Figure 3. 11 (a) The experimental diagram for two-tone spurious-free dynamic range (SFDR) measurements. (b) Detected RF power of the carrier frequencies at 9.5 MHz and 10.5 MHz and the third-order intermodulation distortion (IMD3) frequencies at 8.5 MHz and 11.5 MHz with 1 kHz resolution bandwidth. (c) and (d) RF output power of the fundamental and third order intermodulation distortion (IMD3) component as a function of RF input power of the ring modulator at 1 MHz and 10 MHz.**

The SFDR measurement setup is shown in Figure 3.11 (a). The optical signal from a tunable CW laser (Velocity TLB-6730) is coupled into the PZT modulator, which is biased at the FWHM point of the resonator resonance. A two-tone signal input at 1 MHz and 10 MHz is generated using a Keysight EDU33212A waveform generator. The two-tone signal is applied to the modulator with an RF probe and the fundamental and the IMD3 frequencies are measured with a photodetector (Thorlabs PDB470C, Bandwidth DC – 400 MHz) and a 40 GHz RF spectrum analyzer (Rohde & Schwarz FSEK20, Bandwidth 9 kHz – 40 GHz). The spectrum of a 10 MHz signal with -4.73 dBm RF input power is shown as an example in Figure 3.11 (b) with a measured -80.1 dBm noise floor. The noise power per unit bandwidth is calculated with a 1 kHz resolution bandwidth to be -110.1 dB/Hz assuming the noise floor used in the SFDR calculation [72].

In summary, a low-power photonic integrated PZT actuated stress-optic microresonator modulator is demonstrated for optical control functions, realized in the CMOS-compatible ultra-low loss silicon nitride platform. The waveguide-offset, fully planar design achieves 0.03 dB/cm loss in a 625 μm radius resonator operating at 1550 nm, with a DC - 25 MHz 3-dB optical modulation bandwidth, an order of magnitude improvement over prior PZT stress-optic modulators [7], and power consumption of 20 nW. The resonator has an intrinsic Q of 7.1 million, which is over 10 times larger than prior state of the art [7] and 14 dB ER over a 4 GHz tuning range. The modulator resonance tuning coefficient is measured to be 1.3 pm/V (162 MHz/V) and corresponding half-wave voltage-length products are $V_\pi L$ = 43 V·cm and $V_\pi L\alpha$ = 1.3 V·dB. The IMD3 SFDR is measured to be 65.1 dB·Hz$^{2/3}$ and 73.8 dB·Hz$^{2/3}$ at 1 MHz and 10 MHz, respectively. Since the modulation is based on stress-optic induced

changes in the silicon nitride, this design will work with ultra-low loss visible to IR designs with only small waveguide design changes to operate in the visible [1]. The silicon nitride waveguide layers are completely fabricated in a CMOS compatible process and can withstand temperatures up to 1200 C. The PZT is a back-end process that is deposited at a lower temperature on the silicon nitride wafers after the CMOS process, and is therefore compatible with the ultra-low loss silicon nitride process. This advance in ultra-low loss waveguide modulators will enable chip-level control to be integrated with other ultra-low loss silicon nitride components [11] for a wide range of visible to IR applications, including atomic and molecular quantum sensing, computing and communication, controllable optical frequency combs, low-power stabilized lasers, atomic clocks, and ultra-low phase noise microwave synthesizers.

# 4. PZT Modulation in Laser Stabilization Control Applications

## *4.1 Introductions to PDH Locking and Laser Stabilization*

The Pound-Drever-Hall (PDH) locking technique is a common method to stabilize the laser frequency by locking it to a stable cavity. Originally introduced by Ronald W. P. Drever, J. L. Hall, and R. Pound in the 1980s [74], the PDH locking technique has since evolved into an indispensable tool for achieving high-precision control of laser frequencies. This method has found extensive use in areas such as atomic and molecular physics [75–77], quantum optics [13,14], and advanced technologies like gravitational wave detection [78,79].

PDH locking [30] requires phase modulating the frequency of a laser beam to generate sidebands which contain the definite phase relationship to the incident signal. The phase modulation is typically achieved by using an electro-optic modulator (EOM) and is necessary to generate PDH error signals. Next, an acoustic-optic modulator (AOM) is often needed to perform frequency shifting and adjust the laser frequency to the reference cavity. Then the modulated laser beam is directed into a high-finesse optical cavity. The reflected or transmitted light from the cavity is mixed with the reference laser beam and results in a beat frequency known as the PDH signal, which will be measured with a photodetector and demodulated to generate an error signal that is proportional to the laser frequency deviation from the cavity resonance. This error signal is used in a feedback loop to actively stabilize the laser frequency to the cavity resonance.

Table top ultra-stable lasers employ PDH locking of the laser to a bulky reference cavity with large optical volume to achieve best performance, delivering laser linewidth down to 40 mHz [80]. These spectrally pure laser sources play a pivotal role in precision scientific

experiments and applications such as atomic clocks [16,81], precision spectroscopy [17], quantum computing and sensing [13] and fiber optic links and communications [22]. To fully harness the potential of stabilized lasers, it is imperative to implement these designs and applications on a CMOS-compatible, wafer-scale, photonic integrated circuit platform such as a silicon nitride ultra-low loss platform [11], ensuring small footprint, low cost, and minimal power consumption.

### *4.2 Control Applications: Sideband Modulation and Carrier Tracking with PZT Modulation*

To demonstrate the applicability of PZT modulation in optical control applications and its potential for on-chip photonic integrated laser stabilization, two applications are presented: PDH stabilization of a laser to an optical reference cavity [30] and laser carrier tracking [82]. Figure 4.1 (c) illustrates the experimental setup for PDH locking. Instead of using an electro-optic modulator (EOM), a PZT modulator is employed to generate double sidebands on the laser carrier. An acousto-optic modulator (AOM) is utilized to frequency shift the double sideband (DSB) modulated carrier and lock it to a reference cavity resonance. The reference cavity is an integrated silicon nitride bus-coupled resonator with an ultra-high Q of $10^8$ and a large mode volume of $2.9\times10^6$ $\mu m^3$ [62]. The narrow resonance provided by the high Q is exploited to suppress laser frequency noise fluctuations, and the large mode volume is chosen to reduce the thermo-refractive noise (TRN) floor.

The modulation depth of the DSB modulated carrier is a crucial factor in laser noise stabilization. In this experiment, a 20 MHz, 8 V peak-to-peak sinusoidal voltage is applied

to the PZT actuator, as illustrated in Figure 4.1 (a). Amplitude modulation produces a modulation depth that can be approximated by:

$$\begin{aligned} A(t) &= [1 + m_0 \cos(\Omega t)] A_0 e^{i\omega t} \\ &= A_0 e^{i\omega t} + \frac{m_0 A_0}{2} e^{i(\omega+\Omega)t} + \frac{m_0 A_0}{2} e^{i(\omega-\Omega)t} \end{aligned} \tag{4.1}$$

The sideband modulation depth at $\omega \pm \Omega$, as shown in Figure 4.1 (b), is calculated to be $m_0$ = 0.48 by fitting Equation 4.1 to the measured response, resulting in a sideband-to-carrier power ratio $\frac{m_0^2}{2}$ = 12%. The laser frequency noise (FN) is measured using the self-delayed homodyne laser frequency noise method with an unbalanced fiber MZI optical frequency discriminator [83] with an FSR of 1.03 MHz. The power spectral density of the frequency noise as a function of frequency offset from carrier is shown in Figure 4.1 (d). The stabilized laser frequency noise (red curve) is reduced by four orders of magnitude (~40 dB) compared to the unstabilized laser over the frequency range of 100 Hz to 1 kHz and reduced by two orders of magnitude (~20 dB) at a 10 kHz frequency offset. The laser stabilization locking circuits have a bandwidth of approximately 1 MHz, where the servo bump can be observed in the stabilized frequency noise measurement. The thermo-refractive noise (TRN) floor is calculated for the silicon nitride high Q resonator, as shown by the green dashed curve in Figure 4.1 (d). The stabilized laser is able to achieve close to the TRN limit for this cavity over the frequency range of 1 kHz to 10 kHz. The demonstrated PZT-actuated ring modulator can be an ideal on-chip and low-power solution to the bulk EOM component and provides sufficient bandwidth in a PDH locking circuit for laser stabilization.

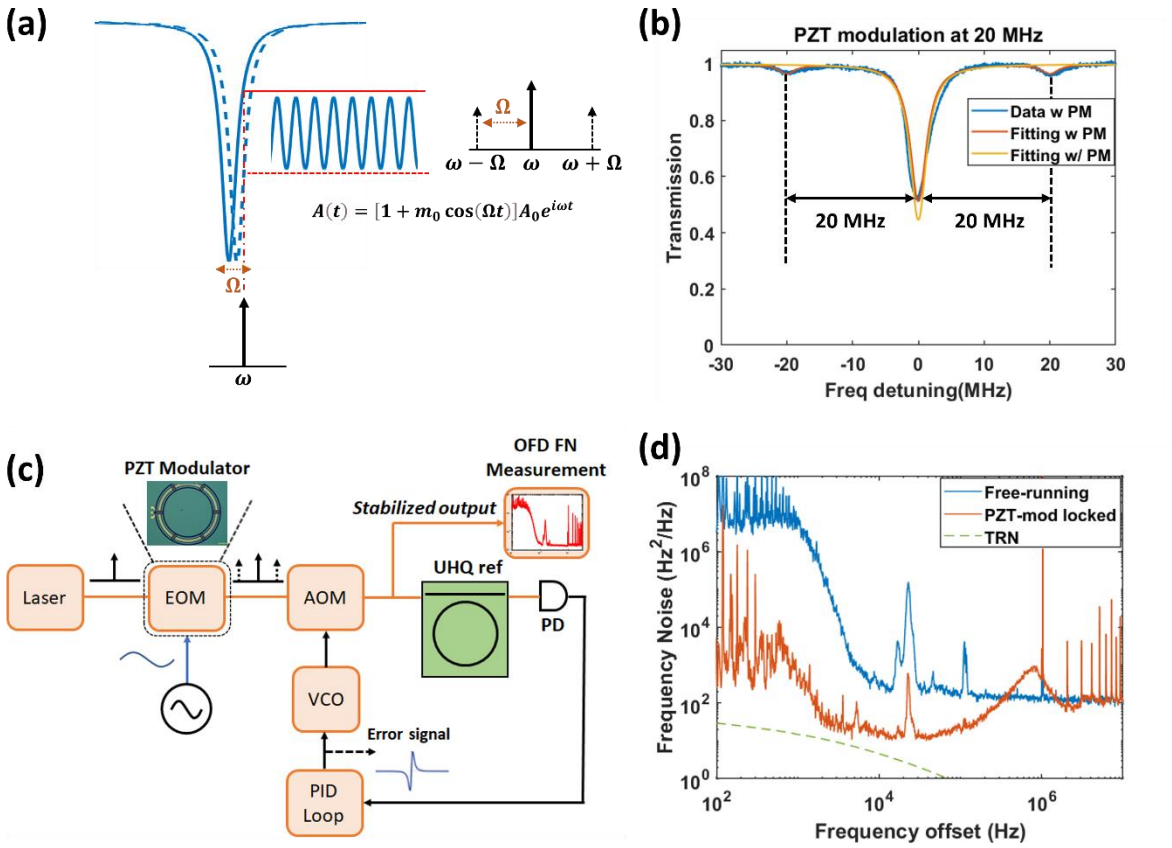


**Figure 4. 1 Laser stabilization demonstration. (a) Illustration of DSB modulated carrier. (b) Measured DSB spectrum of the laser signal with and without the PZT DSB modulation, showing the 40MHz sidebands with modulation depth of 0.48. (c) A semiconductor laser is PDH locked to an ultra-high Q (UHQ) reference cavity using the PZT modulator as a double sideband (DSB) modulator, replacing the electro-optic modulator (EOM). The double sideband modulated carrier is frequency shifted by an acousto-optic modulator (AOM) and locked to the quadrature point of an UHQ integrated reference resonator using a proportional–integral–derivative (PID) control loop that drive a voltage-controlled oscillator (VCO) AOM frequency shift control signal. The resulting stabilized frequency noise is measured using an unbalanced fiber MZI optical frequency discriminator (OFD). (d) Measured frequency noise (FN) power**

**spectral density for the free-running (blue trace) and stabilized laser (red trace) showing 40 dB close to carrier noise reduction and near thermo-refractive noise (TRN) limited performance for the 1 kHz to 10 kHz frequency range.**

The frequency noise of the laser signal is measured using an optical frequency discriminator (OFD) consisting of a fiber based unbalanced Mach-Zehnder interferometer (MZI) and a balanced photodetector (Thorlabs PDB450C). The frequency noise of the laser, $S_f(v)$, is related to the power spectral density of the detector output $S_{\mathrm{det}}(v)$, expressed as [83]:

$$S_f(v) = S_{\mathrm{det}}(v)\left(\frac{v}{\sin(\pi v \tau_D)V_{pp}}\right)^2 \tag{4.2}$$

where $v$ is the frequency offset, $\frac{1}{\tau_D}$ is the FSR of the MZI, $V_{pp}$ is the peak-to-peak value of the detector. A high-speed sampling scope (Keysight Infiniivision DSOX6004A) is used to measure the power spectral density $S_{\mathrm{det}}(v)$ with averaging over 16 traces. The $V_{pp}$ is measured with a ramp signal applied to the MZI.

Demonstration of the PZT modulator as an automated laser carrier tracking filter is shown in Figure 4.2. Laser carrier tracking is essential for monitoring and stabilizing wavelength changes to minimize the wavelength drift and spectral misalignments, which cause power loss and signal distortion in fiber communications [82]. In this experiment, the stress-optic modulator resonance is locked to the laser output using a PID locking loop, as depicted in Figure 4.2 (a). The PDH error signal (shown in the inset) indicates the deviation between the resonator resonance and the laser tone. The PDH servo utilizes the error signal to control the PZT actuator and lock the resonance to the laser carrier. To demonstrate the

tracking function, the filter output is measured in response to a sinusoidally varying output wavelength and to a step response output wavelength shift of the tunable laser. The sinusoidally varying or step input signal ($V_{in}$) is applied to the optical frequency modulation control input of a Velocity TLB-6730 laser. The small signal frequency response of the tracking loop, including the individual responses of the laser, the PZT actuator, the photodetector, and the PID loop, is characterized by $V_{out}/V_{in}$, as shown in Figure 4.2 (b). The bandwidth of the system, characterized at the 180˚ phase lag point, is $f_{180°} = 0.9$ MHz and is mainly limited by the tunable laser bandwidth wavelength control of approximately 1 MHz. As shown on the right side of Figure 4.2 (b), within the locking bandwidth, the optical level at the tracking filter output of the signal is maintained at a constant value (within 3% at 1 kHz and 10 kHz) with the external signal dithering. When the applied signal reaches 1 MHz, which is near a bandwidth resonance, the optical output of the filter fluctuates. The tracking system step response is measured and shown in Figure 4.2 (c), where the blue trace represents the applied step signal (1 kHz square waveform) to the laser frequency tuning, and the red trace represents the control loop response measured at the input to the PZT actuator. The tracking filter output demonstrates the stabilization time (90% to 10%) in response to the step wavelength change at the input. The time to stabilize the lock is approximately 130 μs, and the settling time is approximately 8 μs. With proper bandwidth design, this integrated PZT modulator could be used to monitor and track the signal carrier drifting and filter the desired signals in communication links.

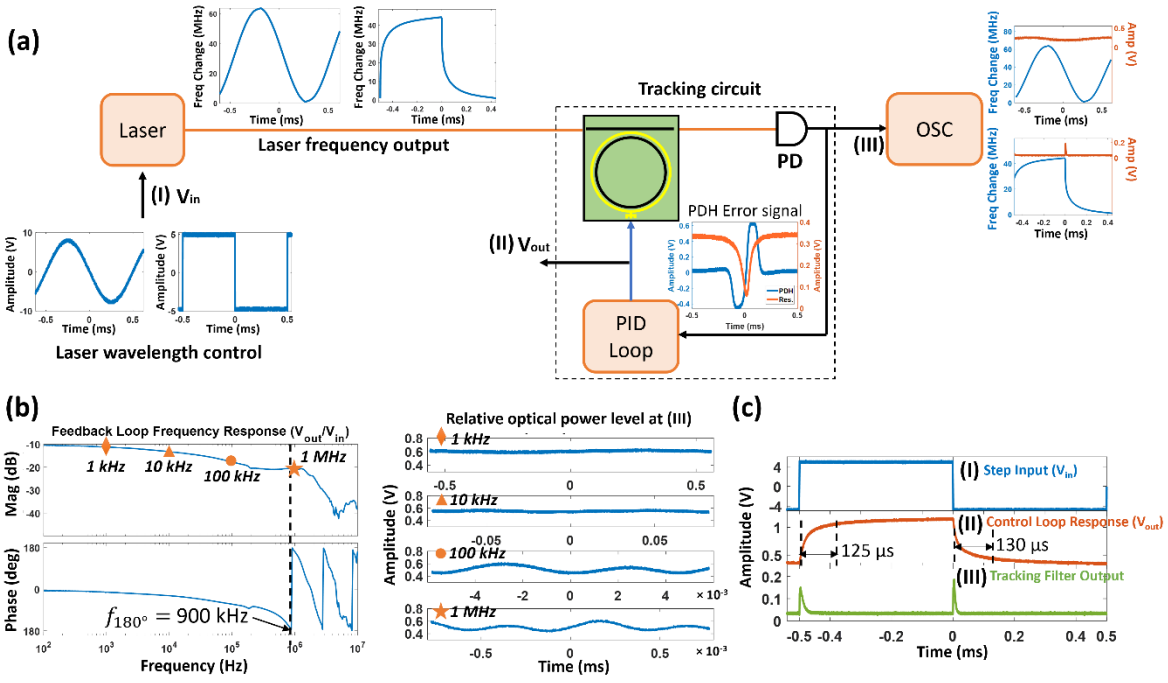


**Figure 4. 2 (a) The PZT-actuated ring modulator is locked to the laser in a PID locking loop, when an external signal is applied to the laser, the locked modulator will respond to the signal dithering and track the laser carrier. The scope at the output port recorded the optical level fluctuation (orange) with the signal dithering in the laser signal (blue). (b) The total response of the feedback loop shows the bandwidth is close to 1 MHz. (c) Step input, control loop response, and tracking filter output stabilization time (from 90% to 10%) ~ 130 µs with ~ 8 µs settling time.**

### *4.3 AOM/EOM-free Laser Stabilization with PZT Modulation*

High spectral purity lasers are a key component for many applications, including precision spectroscopy [17], atomic clocks [16], quantum computing and sensing [13], and fiber optic links and communications [22]. These systems achieve ultra-high optical stability and ultra-low phase noise by employing table-top lasers, free-space optics, bulk AOMs,

EOMs and table-top reference cavities configured with a PDH locking circuit [79]. In order to reduce the size, cost and power consumption of the stabilized laser system, it is necessary to the realize the bulky AOM and EOM functionality in a high-performance photonic integrated circuit technology such as the ultra-low loss silicon nitride waveguide platform [6]. However, AOMs are difficult to realize in the silicon nitride platform and consume high power above 1 Watt, and silicon nitride does not support electro-optic modulation function directly due to its material properties as discussed in the introduction. Therefore, new approaches are needed for integrated PDH laser stabilization in the ultra-low loss, CMOS foundry compatible silicon nitride platform. Our group at UCSB has demonstrated a photonic integrated dual-stage laser stabilization and achieved 292 Hz integral linewidth [83]. The dual stage process is described in Figure 4.3. First, an integrated SBS laser made of ultra-high Q silicon nitride resonator is designed and demonstrated to have the frequency noise reduction at high frequency offsets from the laser carrier due to the nonlinear Brillouin process. Next, the laser signal is PDH locked to an integrated silicon nitride reference cavity fabricated on the same waveguide platform to further reduce the frequency noise at low frequency offsets from the carrier.

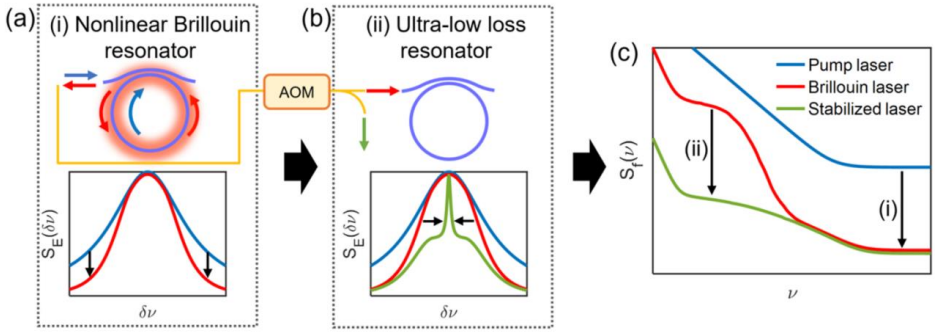


**Figure 4. 3 Dual stage laser stabilization using integrated silicon nitride ultra-high Q resonators [83] as (a) nonlinear Brillouin laser resonator and (b) reference cavity to**

**achieve laser noise reduction at both high- and low-frequency. (c) Frequency noise illustration showing the frequency noise of the laser can be first reduced at the high frequency offset from the carrier due to the nonlinear Brillouin process and then further reduced at the low frequency offset from the carrier by PDH locking to a reference cavity.**

Based on these results, the next step for an integrated stabilized laser is to realize AOM and EOM functions on the chip. Here, we combined the two applications discussed in the previous section and demonstrated the stabilization of a semiconductor laser to an integrated silicon nitride waveguide reference cavity using the integrated PZT modulator, without the use of an AOM or EOM component. The PZT modulator is employed as a novel carrier-tracking DSB modulator that simultaneously generates a DSB signal for the PDH loop while tracking the laser output as the laser is stabilized to the reference cavity.

The scheme, as shown in Figure 4.4, is based on driving the PZT modulator with an electrical combiner network (bias-T) and applying a sinusoidal drive signal to the high-frequency bias-T port that drives the PZT modulator to the DSB and modulates the 1550 nm semiconductor laser (Velocity TLB-6700) output. This DSB-modulated carrier was used to lock the laser onto the $Si_3N_4$ ring-resonator reference cavity with a PDH loop. The low-frequency port of the bias-T is used to auto-track the modulator to the laser by maintaining a constant average output power, whereas a second PID lock stabilizes the laser close-to-carrier noise and drifts to the reference cavity. Using this approach, the photonic integrated PZT modulator provides DSB modulation over a wide laser detuning range, while the frequency noise of the laser is reduced and the carrier is stabilized to the reference cavity by

the PDH loop. The frequency noise of the stabilized optical output was measured using a self-delayed homodyne laser frequency noise method with an unbalanced fiber MZI as the optical frequency discriminator. The resulting frequency noise power spectral density (PSD) is plotted in Figure 4.5 (a) as a function of the frequency offset from the laser carrier. Compared with the free-running laser (blue trace), the AOM-free stabilized laser frequency noise (orange trace) is reduced by over 40 dB from the 10 Hz to 1 kHz frequency offset range and is close to the simulated TRN limit (green dashed trace), which is intrinsic to the optical mode volume for the reference cavity. The $1/\pi$ integral linewidth (ILW) is reduced by 4.5 times from 3.2 kHz to 712 Hz. As shown in Figure 4.5 (b), the Allan deviation (ADEV), which measures the frequency stability between certain amount of observation time, is reduced by an order of magnitude from $1.8\times10^{-11}$ at 5 μs to $2\times10^{-12}$ at 5 ms.

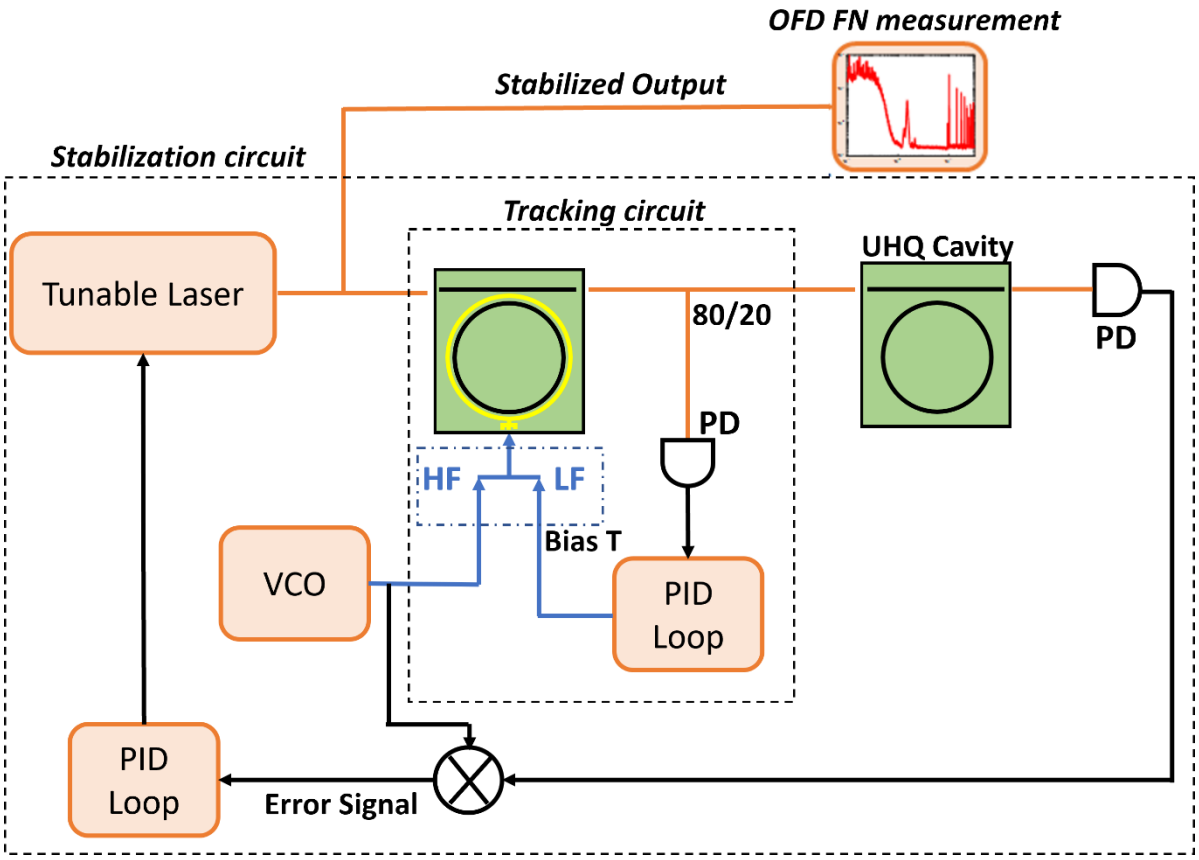

**Figure 4. 4 Experimental diagram for AOM-free photonic integrated stabilization. VCO, voltage-controlled oscillator. UHQ cavity, ultra-high quality factor cavity. PD, photodetector.**

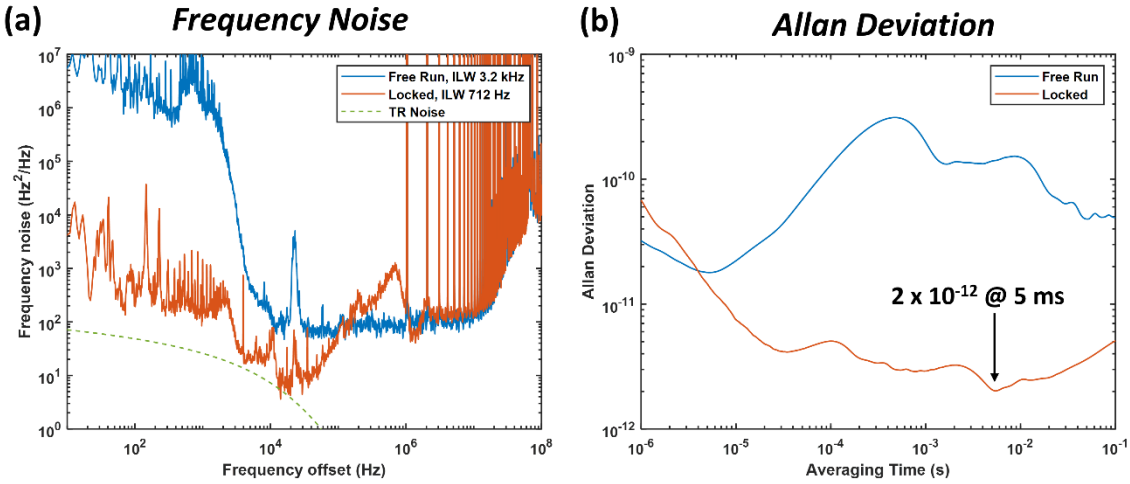


**Figure 4. 5 (a) Frequency noise measurement for the free-running and stabilized laser with simulated TRN in the reference cavity. (b) The ADEV plots of the free-running and the stabilized laser.**

The demonstrated AOM/EOM-free photonic integrated laser stabilization scheme employs only one PZT-integrated silicon nitride ring-resonator modulator in a PDH configuration without the complexity or power consumption, loss tradeoffs, and integration complexity of the bulky AOM frequency shifters and EOM phase modulators. This approach has multiple advantages: (1) The PZT-actuated modulator consumes tens of nW compared to high-power consumption of the AOM component over several watts; (2) the DSB/carrier-tracking modulator does not affect the low optical waveguide losses across the visible to IR; (3) the stress-optic design supports waveguides that can operate from the

visible to the infrared with only simple mask-level or waveguide thickness design changes; and (4) the common integration platform can realize more completely stabilized laser systems on-chip integration. This work demonstrates a path towards photonic integrated stabilized lasers because the PZT stress-optic modulator is compatible with both integrated reference cavity [9] and lasers (e.g., external laser cavity lasers [10], SBS lasers [3] or injection-locked lasers [84,85]), as shown in Figure 4.6. Because the components are fabricated using the same $Si_3N_4$ ultra-low loss waveguide process, this work can be translated to the visible regime [1] and paves the way toward all-waveguide, system-on-chip photonic integrated frequency-stabilized lasers. Such integrated systems-on-chip stabilized lasers will lower the cost and weight and improve reliability for a wide range of applications, such as fiber optic communications, quantum sensing and computing [13], atomic, molecular, and optical (AMO) physics, and atomic clock applications [16].

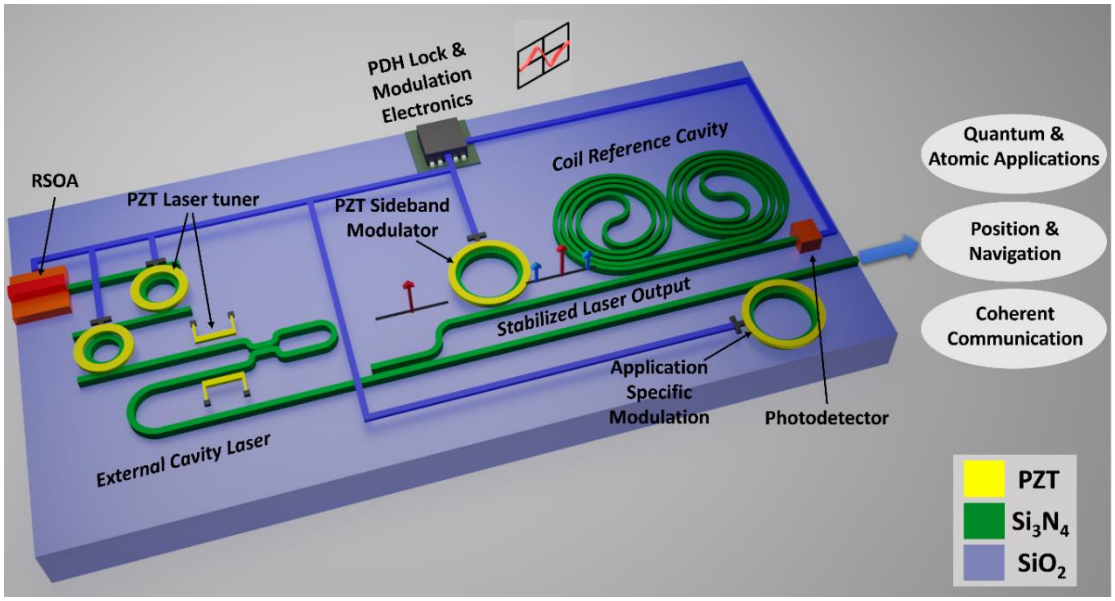


**Figure 4. 6 Illustrative example application of PZT-actuated modulator for control functions in an external cavity laser (ECL). The PZT actuator can be used to tune and**

**control the ECL, and generate sidebands to further stabilize the laser fluctuation by Pound-Drever Hall (PDH) locking to an ultra-high Q reference cavity. The stabilized output can be modulated (optional) based on specific applications.**

# 5. Integrated Symmetrically-coupled Three-Ring Photonic Molecule with PZT Control

## *5.1 Introduction of Photonic Molecule*

Photonic molecules (PM) are systems of coupled atom-like optical resonators that produce rich quantized energy states and supermodes with behavior analogous to atoms and molecules [86]. The field of photonic molecules explores the utilization of photons in optically coupled resonant microstructures to achieve functionalities and behaviors akin to electronic atomic and molecular systems. In this context, optical resonators can be likened to photonic atoms, and groupings of these photonic atoms can be engineered to function as photonic molecules. For instance, an assembly of interconnected photonic atoms, such as micro-resonators, can be employed to create a photonic molecule exhibiting behavior resembling its electronic counterpart, featuring atomic energy levels or resonant states and molecular super-modes. The concept of the photonic molecule is analogous to the hydrogen molecule system [87], as shown in Figure 5.1, the energy level or the orbital of two separated hydrogen atoms are equivalent. When the two atoms get close, the original degenerate energy level will split into a non-degenerate state due to the inter-atom coupling or bonding and anti-bonding atom orbitals. Analogously, the microresonator can be treated as a hydrogen atom in a photonic molecule system. When two resonators are strongly coupled, their degenerate resonant frequency will split into two resonant frequencies. The frequency differential between the split resonances is governed by the interplay of the coupling rates between the two resonators.

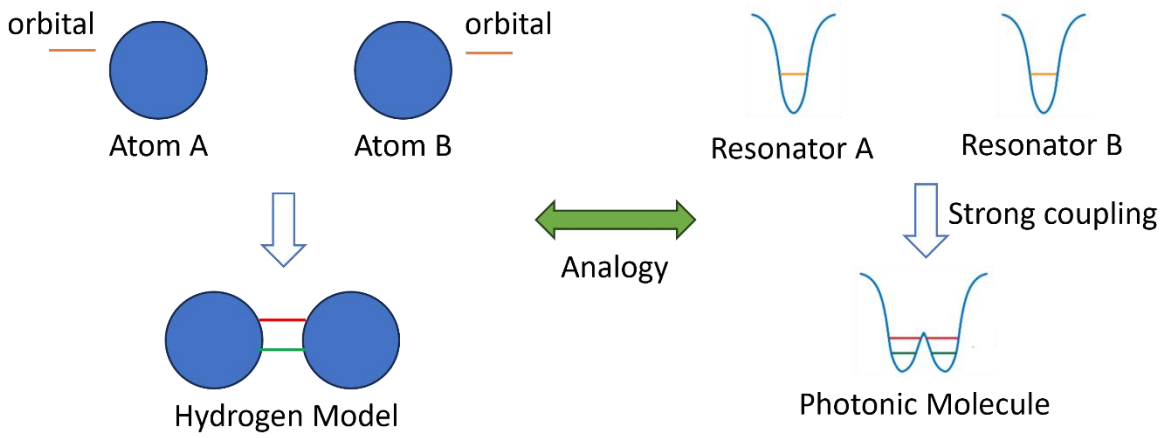


**Figure 5. 1 Analogy of hydrogen model to photonic molecule**

Photonic molecules can realize complex optical energy modes that simulate states of matter and have applications to quantum, linear, and nonlinear optical systems. These characteristics enable precision control of light and light-matter interactions including complex dispersion engineering [88] and nonlinear energy-level transitions [89], and applications including many body physics simulations [90] and quantum optical phenomena [91]. Its applications span various domains, encompassing the development of novel lasers for communication and sensing, spectral engineering [92,93], optical signal processing [94,95], nonlinear optics [96], and nano-particle detection [97]. Furthermore, they find utility in ultra-sensitive spectroscopy detection, label-free single molecule detection [98], ultra-low power optical switching [99,100], analog and specialized analog optical computing and processing (e.g., Ising models), programmable RF and digital optical circuits, slow light, and analogs to electromagnetically induced transparency [101], many-body physics simulations [90], quantum information processing, and quantum communication networks. The incorporation of tunability into photonic molecule structures

enables the harnessing of light forces within resonators for sensing changes in small biological samples, opening up new avenues such as ultra-sensitive spectroscopy detectors and analog specialized computation.

Progress in photonic molecule integration has been limited to the coupling between a single bus to two- and three-coupled microring resonators [102,103], microdisks [104], and photonic crystals [105]. More recent dual resonator advances include electrooptically tunable molecules for soliton optical frequency comb generation [106] and an optical isolator without tuning [107]. These demonstrations have had limited tunability, symmetry, and bus coupling, where molecules with more than two resonators are limited to chain-linked two-two coupling (Figure 5.2 (d)) [108] or serially coupling (Figure 5.2 (c)) [109]. Additionally, thermal tuning for DC bias control has limited power scalability and low linewidth resolution due to low Q and high loss [102]. For more complex coupled resonator circuits, it is critical to enable DC bias resonance tuning of each resonator independently using low-power actuators. In addition to DC tuning and biasing, it is also desirable to use actuators that can be modulated in the MHz to GHz range. In addition, only limited arrays comprising a few coupled very high-Q resonators have been manufactured and utilized for PM demonstrations until recently, with a constrained selection of integration platforms [90]. Although lower Q resonator arrays, such as coupled photonic crystal cavities with Qs in the tens of thousands, have been demonstrated, the fabrication of arrays from resonators with Qs ranging from the tens to hundreds of millions has remained elusive until recent developments. The inability to integrate large-scale arrays of coupled high-Q resonators has hindered the transformation of applications that could leverage these extensive systems of coupled photonic atoms. For instance, only in recent times have strong couplings been

achieved between high-Q whispering gallery mode (WGM) microcavities and tapered fibers, enabling the observation of fundamental temporal behaviors—the optical equivalent of Rabi-like oscillations, previously observed only in low-Q cavities [108,110]. The progression from basic demonstrations involving a few high-Q resonators coupled to tapered fibers to chip-scale integrated high-Q resonators designed and fabricated with waveguides and extensive tunability marks a transformative shift in the field of photonic molecules. The next stage of photonic molecule development requires scaling in terms of the number of resonators per molecule, complexity of energy modes, controllability of the resonance linewidth and splitting, and low power dissipation actuation and fabrication in a wafer-scale CMOS foundry-compatible photonic integration platform. Achieving these goals requires a fully planar fabrication process of low-loss waveguides and high Q coupled resonators that can be independently tuned with low-power actuation that maintains the low loss and high Q.

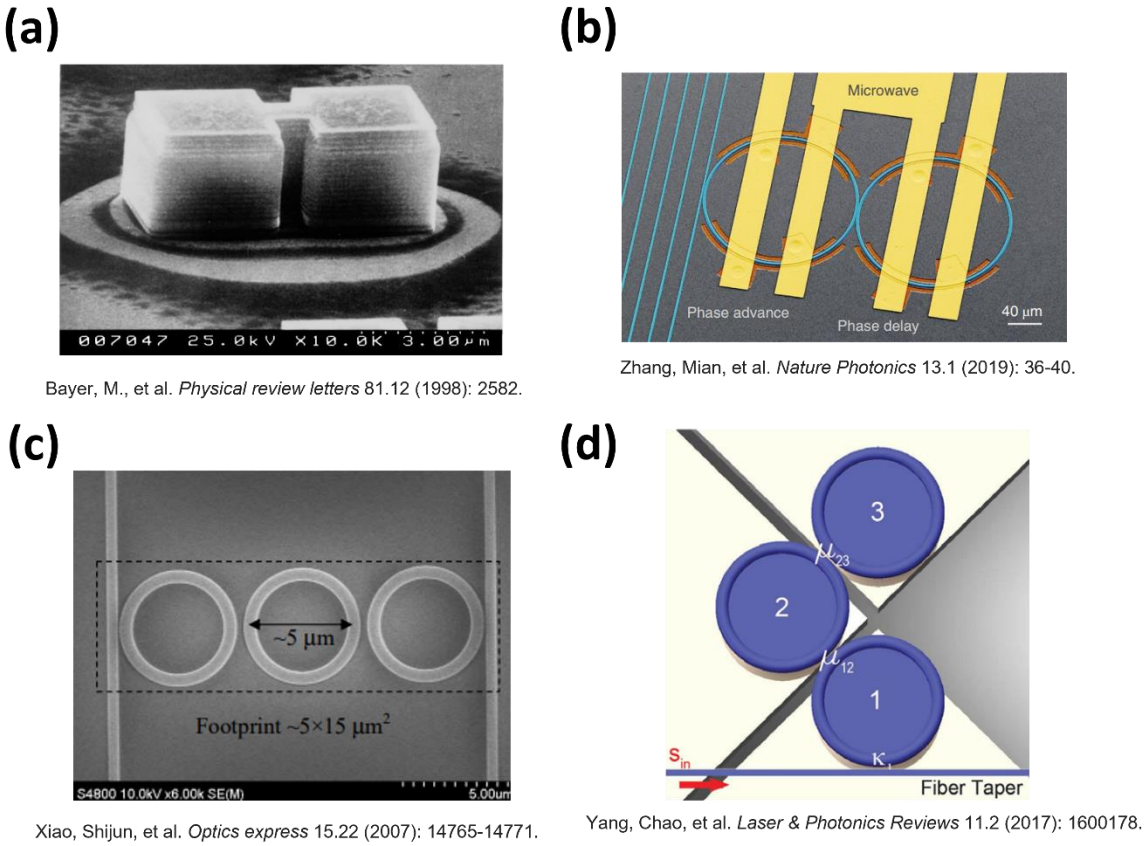


Bayer, M., et al. *Physical review letters* 81.12 (1998): 2582.

Zhang, Mian, et al. *Nature Photonics* 13.1 (2019): 36-40.

Xiao, Shijun, et al. *Optics express* 15.22 (2007): 14765-14771.

Yang, Chao, et al. *Laser & Photonics Reviews* 11.2 (2017): 1600178.

**Figure 5. 2 Previous work on photonic molecule.**

Low power PZT stress-optic actuators are able to maintain low optical waveguide losses and high optical Q with static (DC) tuning capabilities as well as AC modulation, and offer low crosstalk [111]. Other stress-optic modulation approaches include resonant AC aluminum nitride (AlN) modulators [52]. The choice of stress-optic actuator should be compatible with fully planar, ultra-low loss platforms, without requiring complex under-etching processes [7] and maintain low optical losses across the visible to IR.

### *5.2 Device Design and Simulation*

The photonic molecule demonstrated in this thesis is shown in Figure 5.3 (a) with the three coupled ring-bus resonators symmetric to the three axes angled at 120 degrees offset as indicated by the dotted lines. The waveguide and actuator structure are fully planar monolithic as shown before in Chapter 2, without requiring undercut or released tuning structures and waveguides. The individual resonator design hass a 580 μm radius with a 1.5 μm ring-bus coupling gap, and the waveguide geometry is 175 nm thickness and 2.2 μm width. The PZT actuator is designed with a 2 μm horizontal offset gap from the waveguide center to avoid overlap with the optical mode and maintain low optical loss and high Q while realizing a large strain-optic effect and index and resonance shift [111]. The optical microscope image of the fabricated device is shown in Figure 5.3 (b).

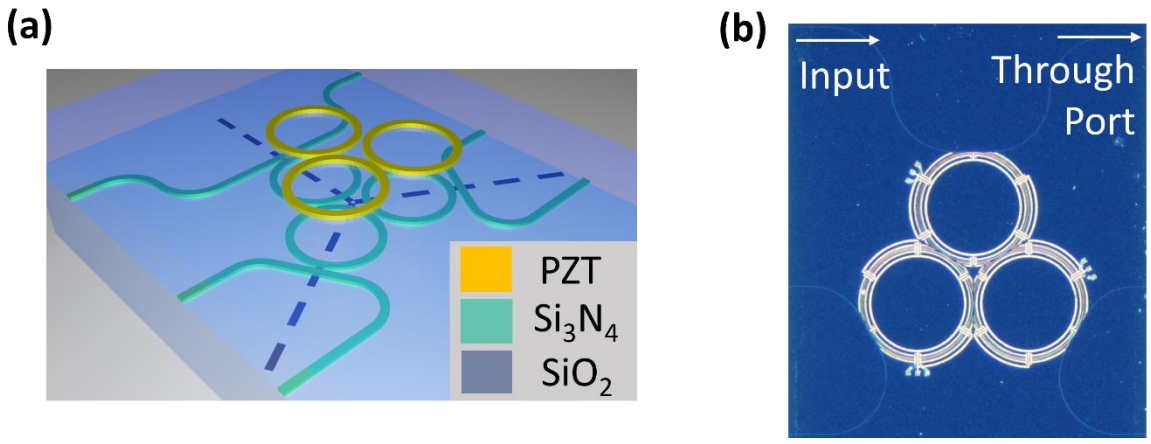


**Figure 5. 3 Illustration of PZT controlled photonic molecule and optical micrograph of a fabricate device with monolithically integrated PZT actuators.**

As discussed in the introduction section, in analogy to the hydrogen molecule where each hydrogen atom has two split states due to the bonding and antibonding orbitals, each

photonic atom in the photonic molecule has two degenerate modes at each resonant frequency due to the mutual coupling to the other two atoms, the clockwise (CW) and the counterclockwise (CCW) propagating, as shown in Figure 5.4 (a) and (b). Each photonic atom (resonator) can be considered to have two split states with a bonding orbital and an antibonding orbital as in the hydrogen molecule model, where these states coherently add to generate supermodes. Therefore, six supermodes are supported due to the strong coupling between all three resonators. The coupling between these modes is determined by the gap between the resonators. If we observe such coupled cavities in standing waves, the modes in each cavity can be treated as either even (E) or odd (O) parity with respect to its axes [112] as indicated in Figure 5.4 (c), in comparison to the hydrogen model where the bonding orbitals (cosine function, even) or antibonding orbitals (sine function, odd) in Figure 5.4 (b) can be treated the same. Therefore, one should observe four energy states from such a photonic molecule system, where Odd-Odd-Odd (OOO) indicates the highest energy level and Even-Even-Even (EEE) represents the lowest energy level. The other four supermodes come into two degenerate pairs, one is symmetric to the vertical axes and the other one is asymmetric.

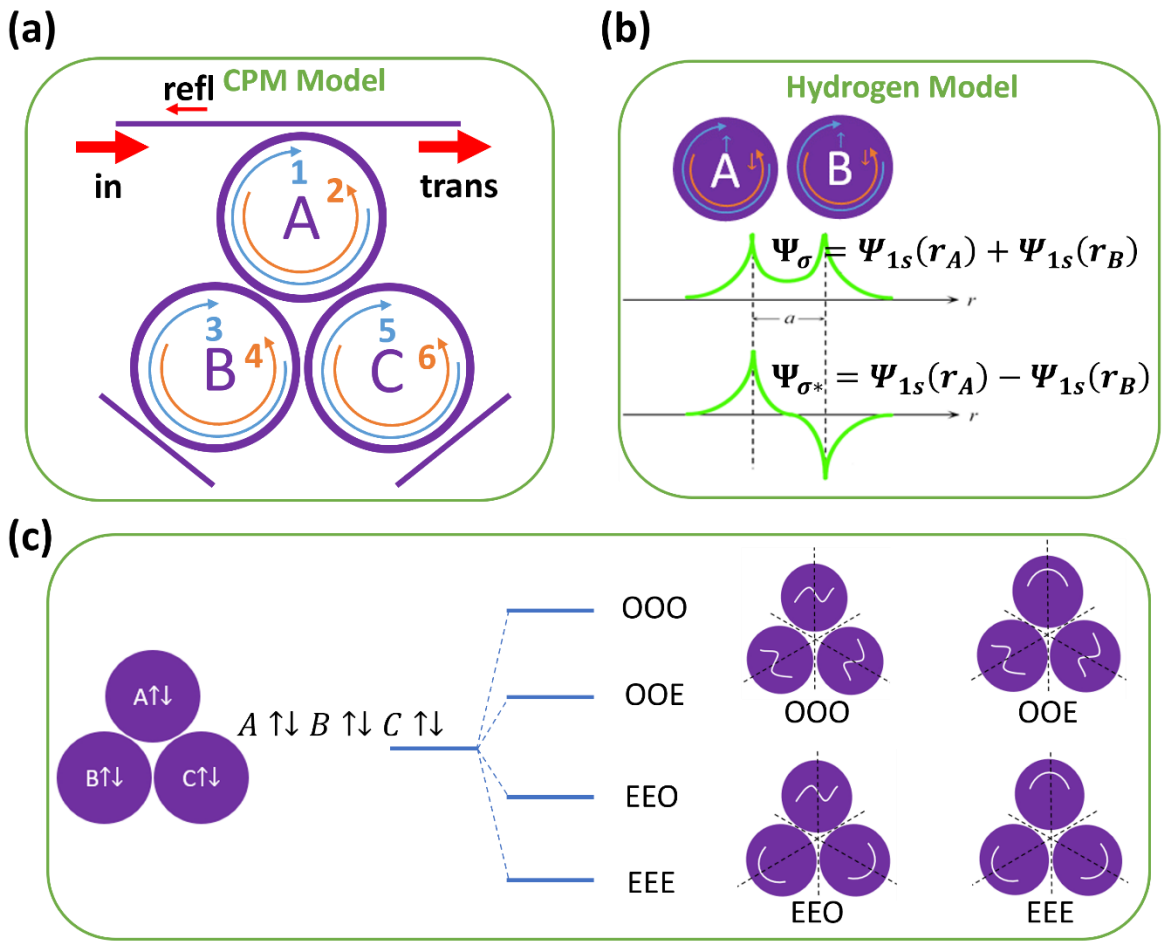


**Figure 5. 4 (a) Coupled photonic molecule model and (b) the comparison with hydrogen model. (c) The energy state splitting of three coupled atoms.**

The coupled mode theory (CMT) model [113] is formulated in a matrix approach, where the diagonal elements specify the resonance frequency and loss rate for each mode and the non-diagonal elements specify the coupling rates between the modes. In this simulation, the backscattering within each resonator due to the perturbation from particles or defects is ignored, since the resonator has a higher linewidth than the backscattering induced mode splitting [62].

The general transfer matrix therefore can be developed as [113]:

$$\frac{d}{dt}\begin{bmatrix} a_1 \\ a_2 \\ a_3 \\ a_4 \\ a_5 \\ a_6 \end{bmatrix} = \begin{bmatrix} -\frac{\gamma}{2}+i\omega_A & 0 & 0 & i\kappa_{12} & 0 & i\kappa_{13} \\ 0 & -\frac{\gamma}{2}+i\omega_A & i\kappa_{12} & 0 & i\kappa_{13} & 0 \\ 0 & i\kappa_{12} & -\frac{\gamma}{2}+i\omega_B & 0 & 0 & i\kappa_{23} \\ i\kappa_{12} & 0 & 0 & -\frac{\gamma}{2}+i\omega_B & i\kappa_{23} & 0 \\ 0 & i\kappa_{13} & 0 & i\kappa_{23} & -\frac{\gamma}{2}+i\omega_C & 0 \\ i\kappa_{13} & 0 & i\kappa_{23} & 0 & 0 & -\frac{\gamma}{2}+i\omega_C \end{bmatrix} \begin{bmatrix} a_1 \\ a_2 \\ a_3 \\ a_4 \\ a_5 \\ a_6 \end{bmatrix} + \begin{bmatrix} 1 \\ 0 \\ 0 \\ 0 \\ 0 \\ 0 \end{bmatrix} i\sqrt{\gamma_c}s_{in} \tag{5.1}$$

where $a_i$ represents the modal amplitudes of the supermodes, $\omega_i$ is the resonant frequency of individual photonic atom, $\kappa_{ij}$ is the coupling rate between the $i_{th}$ and $j_{th}$ modes, $\gamma$ is the total loss rate, $\gamma_c$ represents the bus-ring coupling rate and $s_{in}$ is the optical input in the bus waveguide.

Thus, the transmission for each port pf the photonic molecule can be plotted based on the matrix. For example, from the input port to the throughput of the PM can be written as:

$$T = \left|\frac{S_{out}}{S_{in}}\right|^2 = \left|1 + i\sqrt{\gamma_c}a_1\right|^2 \tag{5.2}$$

The drop port $n$ or the reflection port can be written as:

$$R_n = \left|i\sqrt{\gamma_c}a_n\right|^2 \tag{5.3}$$

Therefore, the spectrums of each port can be simulated based on the equations and matrix above with different settings of intrinsic and coupling losses ($\gamma$, $\kappa_{ij}$ and $\gamma_c$). An example is shown in Figure 5.5 for symmetric alignment case.

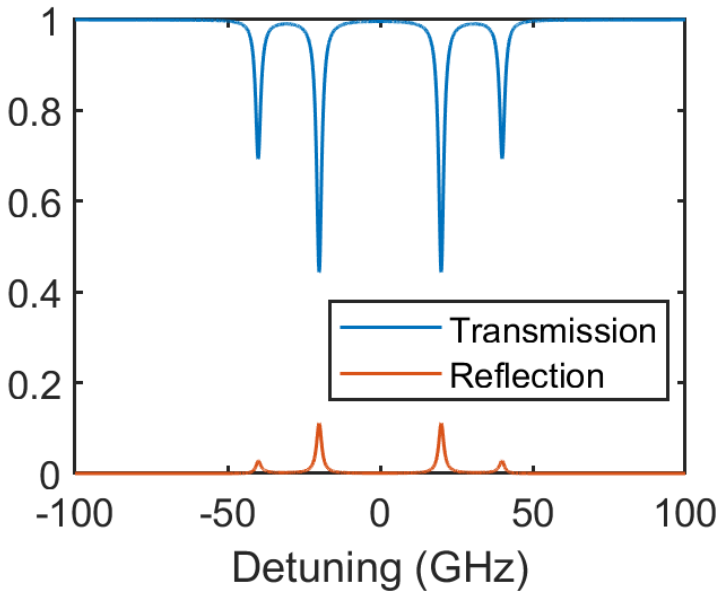


**Figure 5. 5 Simulation of the symmetric alignment case of transmission and reflection spectrum.**

To verify the accuracy of the numerical modeling, simulation of such a structure is also performed in Lumerical INTERCONNECT. Due to the relative large size of the photonic structure, it is time- and resource-consuming to perform an accurate FDTD (Finite-Difference Time-Domain) simulation. Alternatively, INTERCONNECT provides an efficient way to simulate such a complex photonic structure in component level. As shown in Figure 5.6, the PM is simulated in Lumerical INTERCONNECT using the waveguide and the coupler components to realize the three symmetrically coupled resonator system by incorporating device waveguide length, measured waveguide losses, simulated effective mode index and coupling coefficients.

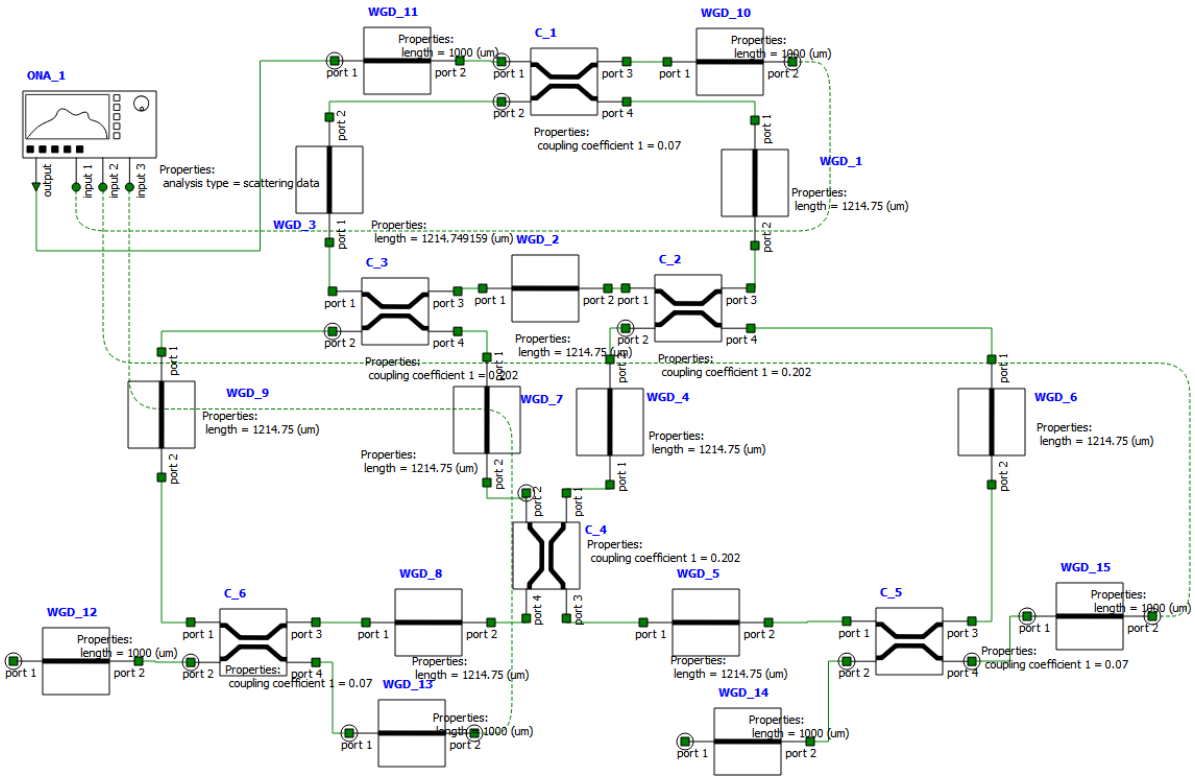


**Figure 5. 6 Lumerical INTERCONNECT schematic diagram.**

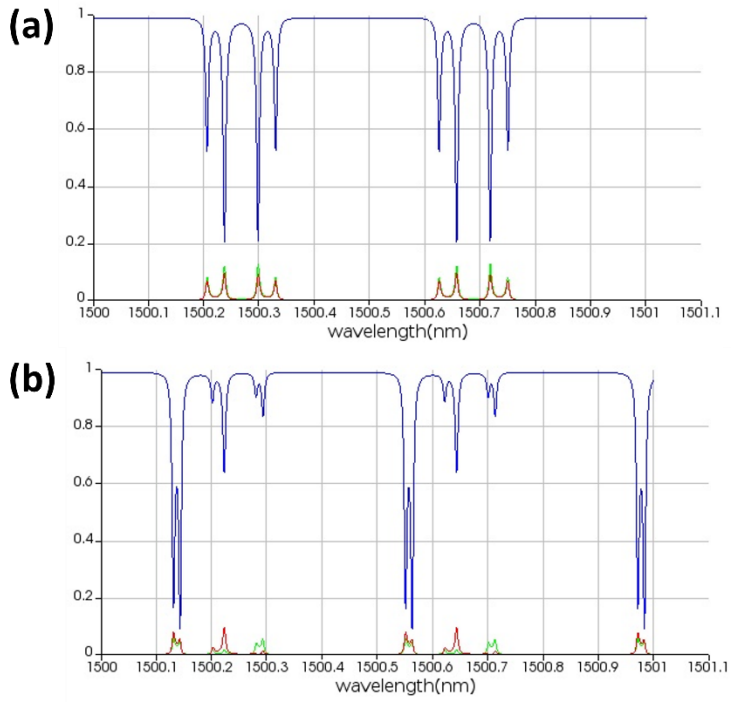


**Figure 5. 7 Lumerical INTERCONNECT simulation of (a) symmetric aligned case and (b) non-degenerate splitting case. Blue curve represents the through port output and the red and green curve represent the drop ports at the two other rings.**

Three mode-splitting cases are studied and the comparison between the CPM modeling and the device simulation for different cases ((a) perfectly symmetric case, (b) non-degenerate case, and (c) actual measurement case) are shown in Figure 5.8, and the accuracy between the modeling prediction, simulation verification, and measurements can be confirmed. When all resonator waveguides and coupling parameters are identical, the energy modes are degenerate with 4 supermodes as shown in the transmission spectrum in Figure 5.8 (a). The rightmost supermode has the highest energy level and the leftmost supermode has the lowest energy level. The four remaining supermodes are present in two degenerate pairs [112]. When symmetry is broken, for example, if the coupling strengths κ between the

resonators are non-uniform, the middle degenerate pairs split and mode degeneracy is lifted, as shown in Figure 5.8 (b). Fabrication variations among resonators and coupling lead to asymmetric molecule energy, as shown in the experimental and modeled energy spectra in Figure 5.8 (c).

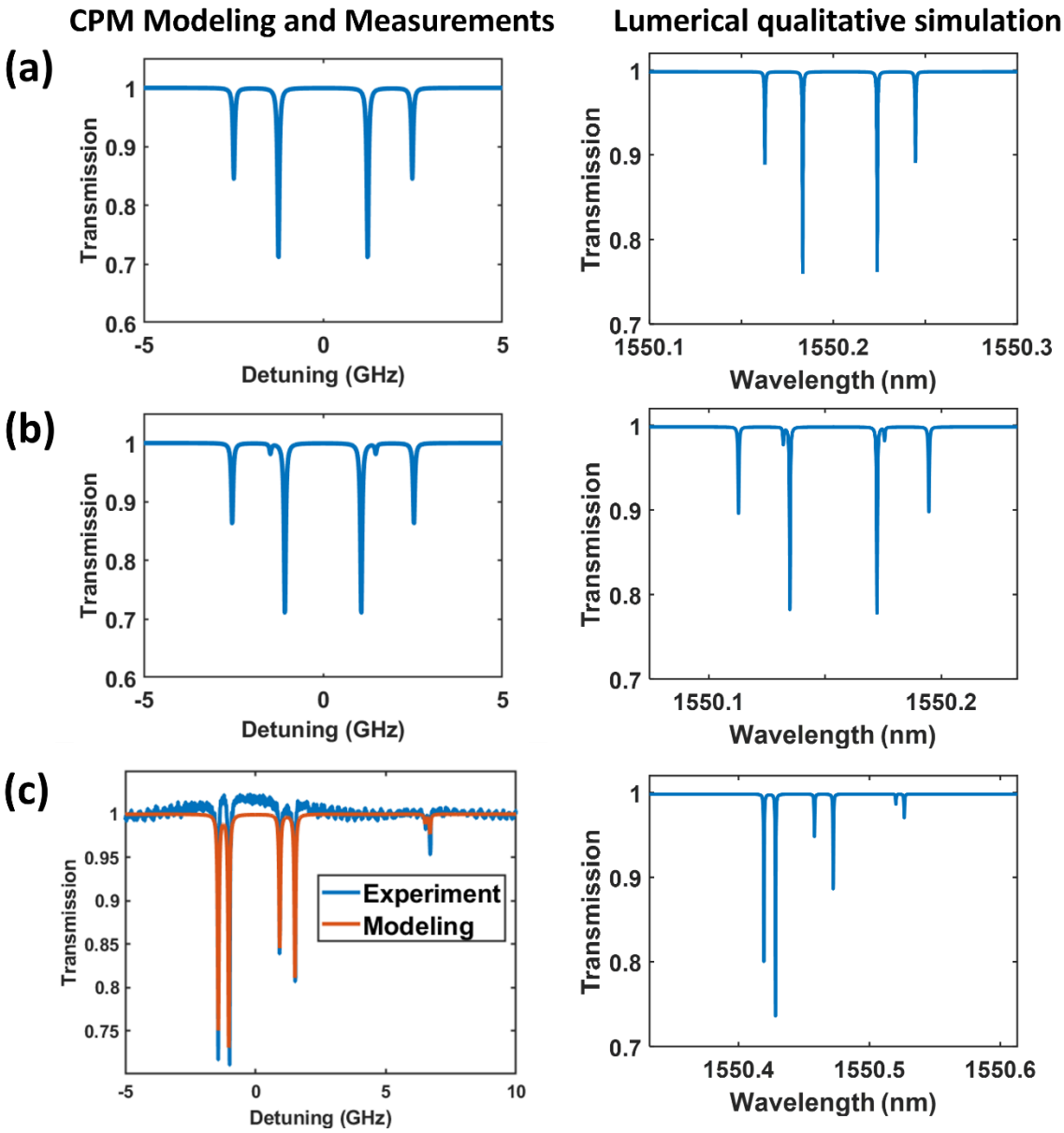


**Figure 5. 8 Comparison between the coupled photonic molecule (CPM) modeling (left side) and Lumerical simulation for different cases (right side).**

### *5.3 Device Characterization and PZT Control Demonstration*

We measure the resonance FWHM of the single-ring resonator that composes the three rings to be 43.23 MHz at 1550 nm, as shown in Figure 5.9 (a), using a radio frequency calibrated unbalanced MZI [62]. These measurements correspond to an intrinsic Q factor of 8.11 million and loaded Q factor of 4.48 million, corresponding to a propagation loss of 3.3 dB/m. For comparison, the resonator of the same geometry but without the PZT actuator has a resonance FWHM of 36.60 MHz, as shown in Figure 5.9 (b), corresponding to an 8.37 million intrinsic Q factor and propagation loss of 3.19 dB/m. The loss is increased by only 3%, demonstrating that the monolithically integrated PZT actuators maintain the properties of the ultra-low waveguide loss and high-Q. The device has a 48 GHz FSR and a 2.5 GHz tuning range with tuning responsivity of 160 MHz/V. The photonic molecule insertion loss is estimated to be 1 dB from the through port, with a coupling loss measured with a straight waveguide to be 5 dB from double sides.

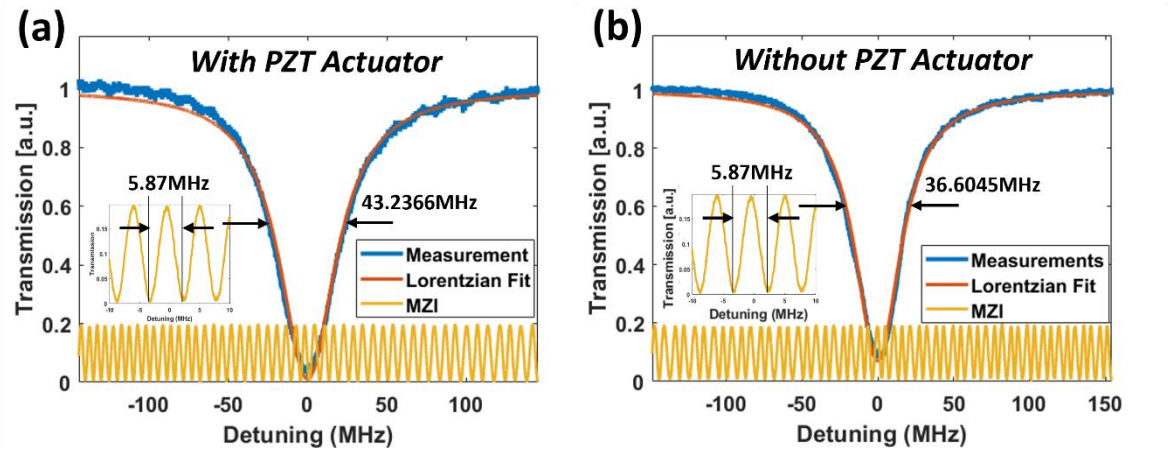


**Figure 5. 9 The quality factor (Q) measurement of a single ring resonator with R = 580 µm with and without PZT actuator.**

The actual transmission spectrum of the PM is measured as shown in Figure 5.10, and the six supermodes have well-defined resonances with narrow linewidths of 47 MHz, 49 MHz, 58 MHz, 54 MHz, 46 MHz and 50 MHz, and corresponding loaded Q factor of 4.12 million, 3.95 million, 3.34 million, 3.58 million, 4.21 million and 3.87 million respectively. The measured spectrum (blue) is in good agreement with the CMT matrix model fitting (orange), which incorporates the measured cavity loss $\gamma$ and inter-ring coupling coefficient $\kappa$. This model allows us to accurately design and predict the mode energy splitting, which becomes increasingly important as the energy state complexity of photonic molecules increases and enables calibration owing to fabrication and environmental perturbations. The drop ports of the photonic molecules were measured as shown in Figure 5.11.

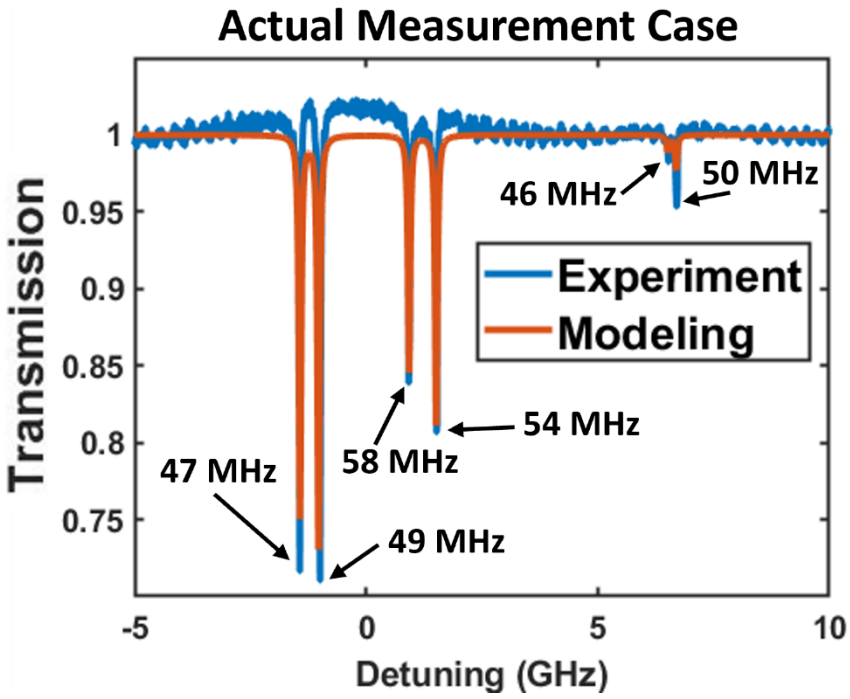


**Figure 5. 10 Measured and modeled PM transmission spectra for a single bus.**

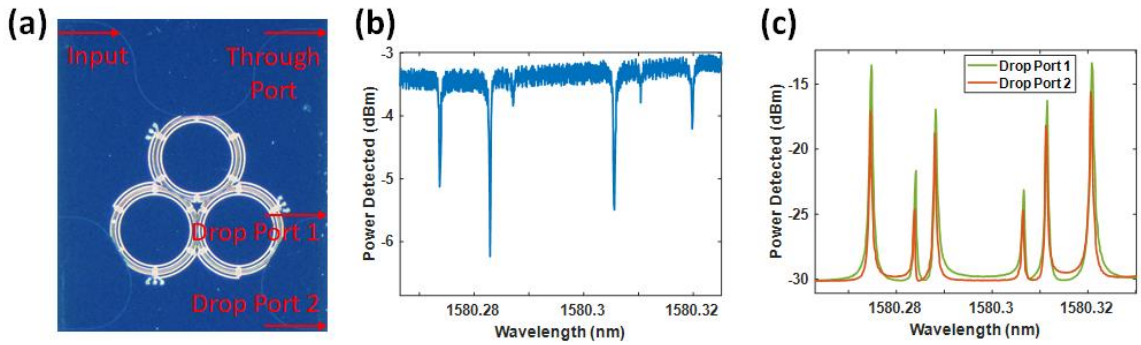


**Figure 5. 11 Spectrum measurements of the photonic molecule (a) at both through port (b) and drop ports (c).**

Next, we demonstrate PM supermode tuning by controlling the PZT DC bias for each ring resonator. The independent DC bias for each ring resonator enables full control over supermode splitting and frequency location. An example is shown in Figure 5.12 (a) - (c). The colored lines indicate the measured transmission spectra as the DC bias voltages applied to the PZT actuators were adjusted from 0 V to 15 V on each ring. The modeled behavior, indicated by the dashed lines, is in strong agreement with the measurements, yielding an important tool for designing, predicting, and accurately controlling the supermodes. By tuning two resonators simultaneously, the symmetric degenerate case can be reached, as shown in Figure 5.12 (d), demonstrating that the photonic molecule can be calibrated and balanced, and the energy splitting can be tuned and controlled. The PZT material has a high resistivity, resulting in a very low leakage current and power dissipation, measured to be approximately 6 nA at a 15 V bias, corresponding to 90 nW electrical power consumption per actuator. The capacitance of the PZT actuator was measured as approximately 600 pF, corresponding to a stored energy of 67 nJ at 15 V.

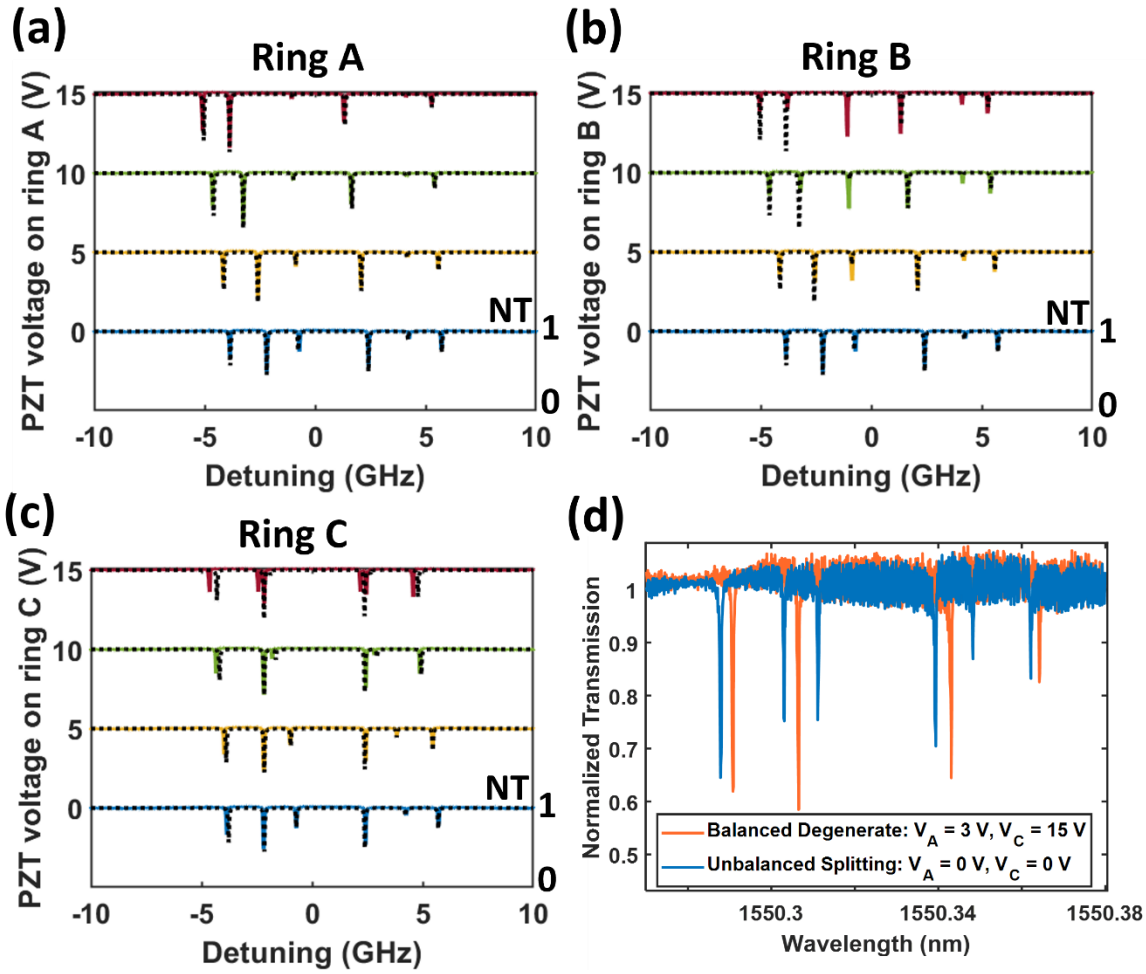


**Figure 5. 12 (a)-(c): DC biasing of rings A, B and C. The colored lines indicate the measured transmission spectrums as DC bias is adjusted from 0 to 15V and the dashed black lines are the coupled photonic molecule model fitting. (d) The symmetric case can be reached by tuning multiple rings; N.T., normalized transmission.**

### *5.4 Discussion of the work*

A comparison of the performance of this work that with of three other coupled-resonator photonic molecules is summarized in Table 5.1. This work demonstrated a monolithically integrated, programmable, and strongly coupled three-ring resonator photonic molecule. The

molecule consists of silicon nitride three-ring resonators with an intrinsic Q of $8.11\times10^6$, the highest reported to date for a PZT-controlled integrated ring resonator. The ability to maintain high Q via PZT actuation without degradation as the resonance shifts results in narrow PM resonance linewidths that are independent of the tuning and state splitting, and a resonance splitting to linewidth ratio of 58, representing the lowest linewidth for a PZT tunable resonator and over an order of magnitude improvement in the resonance split-to-linewidth ratio for a prior integrated three-resonato PM [102]. The PZT actuator offers 90 nW ultra-low power dissipation with a linear tuning coefficient of 160 MHz/V. The devices are fabricated using a CMOS foundry compatible process without requiring complex processes, such as undercut or released and suspended structures.

PZT actuation provides a programmable PM platform that increases the design and spectral flexibility and the potential to scale to larger arrays owing to its lower power and compact size. The multiple discrete levels of the photonic molecule can be utilized as a signal splitter or wavelength shifter with proper PZT spatiotemporal modulation [111] and can enable new integrated circuits for tunable dispersion compensators [106], optical frequency comb generation [114], and optical parametric oscillation by tuning the phase matched modes [115]. These results provide a path towards integration of photonic molecules for applications like multichannel high-order filters [103], topological photonics [88], ultra-low phase noise lasers through higher-order mode inhibition of stimulated Brillouin lasers (SBL) through mode splitting [116], and many body physics simulations [90]. Low-power consumption is critical to enable large-scale integration of coupled photonic atoms and complex photonic molecules on a chip and is suited for heterogeneous integration with semiconductor lasers.

| Reference | This work | [102] | [108] | [109] |
|---|---|---|---|---|
| Integration | Yes | Yes | No | No |
| Material | Si3N4 /SiO2 | SOI | Silica toroid | Polymeric Silicone |
| Tunability | PZT | Microheater | Temperature control (TEC) | Mechanical Stretching |
| Loaded Q | 4.48 M | 6.7 K | 29, 37 & 110 M | 79 K |
| Linewidth | 43 MHz | 29 GHz * | 6.8 - 1.8 MHz | NA |
| Supermodes | 6 | 6 | 3 | NA |
| Detuning Range | 2.5 GHz | 80 GHz | 0.75 GHz * | NA |
| Resonance Splitting / Linewidth | 58 | 2.8 | 110 | NA |
| Power Consumption | 90 nW per actuator | 35 mW | NA | NA |

**Table 5. 1 Summary of this work with comparable integrated ring-resonator modulator. SOI: silicon on insulator; TEC: thermoelectric cooler. * Extracted based on the information provided in the literature.**

# 6. Discussion and Future Work

## *6.1 Non-magnetic integrated optical isolator and circulator*

One of the potential future works that this thesis could lead to is a non-magnetic integrated optical isolator and circulator. Non-reciprocal devices, such as optical isolators and circulators, play a crucial role in telecommunication and quantum applications by facilitating signal routing and preventing unwanted back-reflection signals to protect and stabilize lasers. The main approaches to optical isolation require breaking optical reciprocity and include the intrinsic magnetic response in a material used with the waveguide [117], utilizing optical nonlinearities for spatial mode, polarization, or frequency conversion [118], employing temporal modulation of the refractive index of the material [119], and exploring optical chirality [120]. Traditionally, non-reciprocity in optical systems has been achieved through the use of magneto-optic materials and Faraday effect-induced polarization rotation [121,122]. However, this method often requires an external magnetic field, permanent magnets, or a current loop. Such requirements are not compatible with the CMOS fabrication processes. Introducing a magnetic field on-chip may adversely affect nearby electronics and circuits, thereby presenting challenges for backend processing.

Other non-magnetic techniques have also been demonstrated. These effects utilize nonlinear mode, frequency conversion, or RF frequency index modulation. Optical nonlinearities, such as second-order Kerr nonlinearity, are input signal power-dependent and some designs do not work with both input and reflected signals simultaneously, attributes that do not lend to a true optical isolator. Direct modulation of the refractive index using traveling or standing wave index modulation is an attractive approach, with past designs having a large footprint, high power, and complex electrode connections.

Based on the results of three-resonator photonic molecule discussed in Chapter 5, we propose a non-magnetic integrated optical isolator and circulator by spatio-temporal modulation of three photonic integrated silicon nitride waveguide bus-coupled optical ring resonators, as shown in Figure 6.1 (a), and modulated by low-power stress-optic PZT actuators that are driven by three RF signals of the same amplitude but are 120-degree phase-shifted between rings, as shown in Figure 6.1 (b). This design is inspired by an electrical circuit demonstrated for RF isolation with 40 dB isolation [123], which utilized the parametric modulation of three coupled discrete electronic RLC resonator tank circuits. Modulation of the index of refraction in a ring resonator as a function of position in the ring and time imparts an equivalent angular velocity. However, modulation of the index in a single ring has serious drawbacks, including constraints imposed by the boundary conditions of the optical and electrical fields, lack of tunability, limits on isolation and engineering of isolation passband shapes, and lack of three-port operation as a circulator. The proposed approach shown in Figure 6.2, splits the resonator into three strongly coupled resonators, each with its own bus coupling. This geometry provides several advantages: (1) bulk modulation of each ring can be performed at arbitrary frequencies determined by the desired isolation separation, which can be as low as the MHz regime to 10s to 100s of MHz, design choice; (2) each resonator has a coupled bus providing 3-port circulator function; (3) DC tuning of the ring coupling provides full tunability using the photonic molecule tuning model; (4) driving the resonators can be achieved with low power (10s nW) PZT actuators; and (5) the combination of ultra-low loss silicon nitride with PZT modulation enables very high Q with narrow resonator linewidths, making tuning and isolation possible with lower bandwidth (e.g. 10s of MHz) signals.

When the driving frequency matches the ring-to-ring coupling rate with proper RF driving power, an effective angular momentum will be imparted on the three resonators in a circularly rotating fashion, thus breaking the reciprocity by introducing an asymmetric phase shift for counter-propagating modes of the photonic molecule [123]. This asymmetric splitting frequency up-shifts the passband resonances for light propagating through the photonic molecule in one direction and frequency-down shifts the passband resonance for light propagating through the photonic molecule in the opposite direction while simultaneously routing it to another of the bus ports, making the circulator function. For a symmetrically aligned three-resonator photonic molecule, one should observe the degenerate mode split in one light propagation direction but remain the same in the other direction when the reciprocity breaking condition is reached, indicating signal isolation. The driving frequency also needs to be larger than the linewidth of the supermode so that the splitting will fall out of the resonance band and achieve a large isolation. An example of the measurement setup for the 780 nm photonic molecule isolator is shown in Figure 6.2.

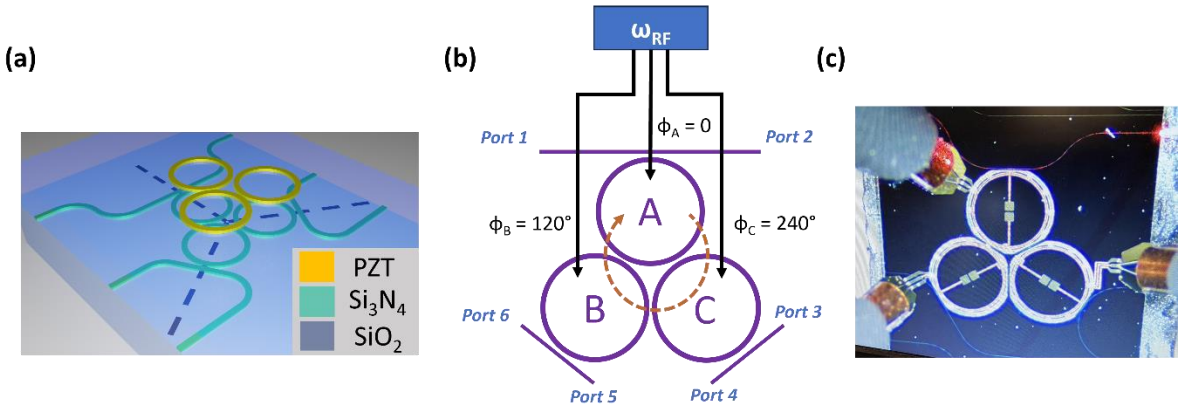


**Figure 6. 1 (a) Three-port integrated optical isolator/circulator; (b) Imparting equivalent angular moment via parametric modulation of three coupled resonators with three RF signals of same amplitude and 120 degrees phase shift from each other**

**to induce magnetic-free optical non-reciprocity; (c) Measurements showing RF probing of three resonators photonic molecule with PZT actuators.**

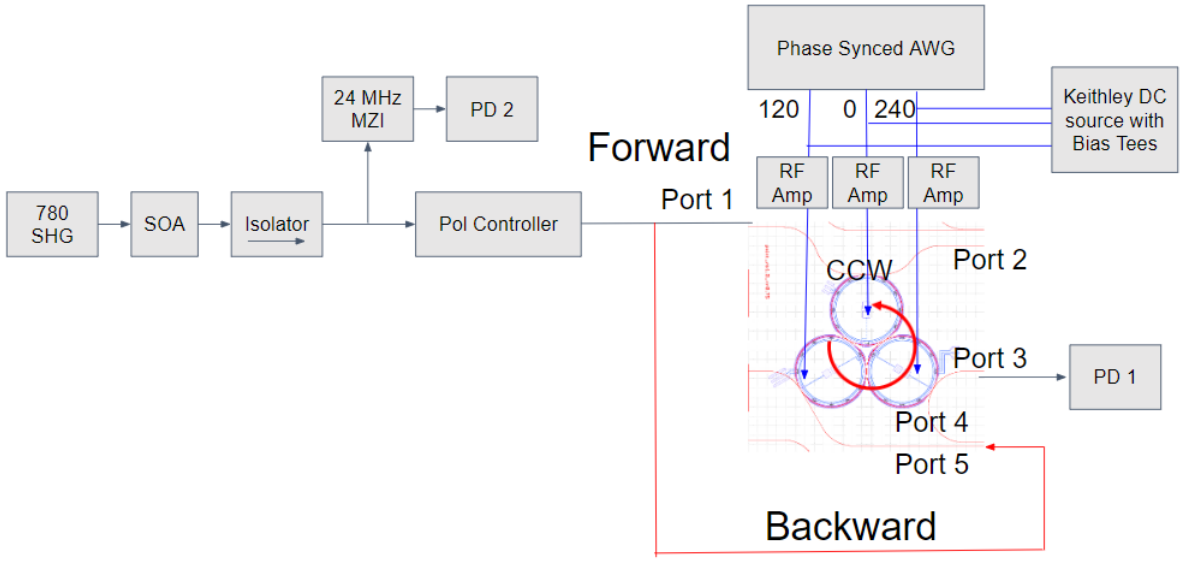


**Figure 6. 2 Measurement setup for 780 nm isolator test. The three RF signals are generated from the arbitrary waveform generator (AWG) and are phase synchronized, and then are amplified and applied to each resonator via the PZT actuator modulation.**

This approach has advantages over single-ring approaches [124] including wavelength tunability, decoupling of the relationship between optical resonance and electrical modulation, and benefits of a three-port optical circulator. Ultra-low power dissipation PZT actuators are planar-processed on the wafer scale and are compatible with the silicon nitride platform, leading to a promising approach for photonic integrated non-magnetic optical isolators and circulators.

### *6.2 PZT-actuated fast-switchable high-order ring filter*

Another application that can be enabled by the PZT modulator demonstrated in this thesis is the PZT-actuated fast-switchable high-order filters. Fast-switchable and widely tunable optical filters are important for many applications in optical communications, tunable laser sources, and nonlinear optics. It is desirable to have filters with a high extinction ratio, flat passbands, and low loss that can be quickly switched on and off faster than 1 μs for optical gating, which can be realized by coupling multiple rings based on a silicon nitride ultra-low loss waveguide platform and controlled by fast PZT modulation and tuning.

As shown in Figure 6.3, 3$^{rd}$ and 4$^{th}$ order of cascaded ring filters have been designed at 780 nm and 1550 nm, respectively, for AMO and telecommunication applications. According to the simulation shown in Figure 6.4, these add-drop filters can have a flat passband of approximately 6 GHz, with a large extinction ratio of 100 dB for the 3$^{rd}$ order filter and 120 dB for the 4$^{th}$ order filter. The PZT actuator demonstrated in the previous chapters with a 20-30 MHz modulation speed can be used to switch the filter into and out of the signal carrier frequency, achieving less than 0.1 μs switch time, which cannot be realized by conventional low-speed thermal tuner.

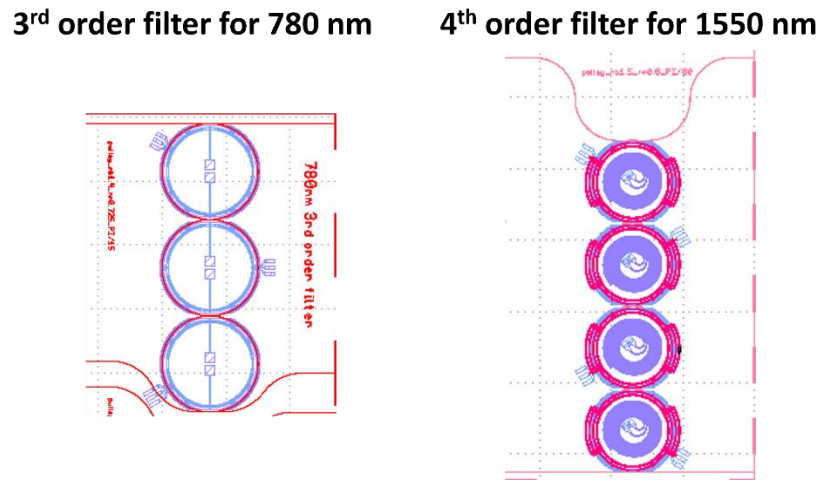


**Figure 6. 3 Third and fourth order ring filter design for 780 nm and 1550 nm. Thermal heater using the bottom Pt electrode layer is patterned inside the ring to assist for cascaded ring resonance alignment.**

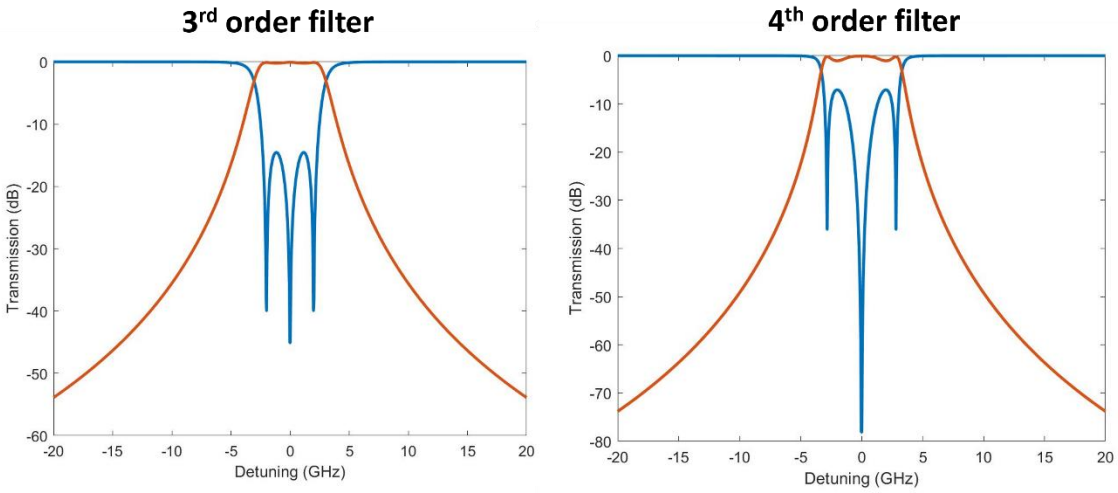


**Figure 6. 4 Simulation of the high-order ring filter at 1550 nm. For third order filter design, a flat passband about 6 GHz with 100 dB extinction ratio can be reached; for fourth order filter design, a flat passband about 6 GHz with 120 dB extinction ratio can be reached.**

### *6.3 Photonic integrated stabilized laser*

As discussed in Chapter 4, an immediate near-term work is to develop a fully on-chip and photonic integrated stabilized laser using a PZT modulator and actuator for the on-chip control and tuning functions. There are two types of design. The first is a PZT-tunable external cavity laser. As shown in Figure 6. 5, the external cavity is based on an ultra-low loss silicon nitride waveguide platform, and the PZT actuator can be integrated into the vernier rings and waveguide phase shifter to control the external cavity and detune the laser. The second design is similar to that discussed in Chapter 4, where the PZT modulator can be implemented in the AOM/EOM-free scheme and acts as a bridge to connect the dual-stage laser stabilization with the nonlinear Brillouin laser and reference cavity locking. As shown in Figure 6.6, the PZT actuator can be integrated on top of the SBS resonator and the filter ring to directly control and detune the SBS laser. Then, on the same waveguide platform, the PZT modulator can be used as a DSB modulator and the laser signal can be further PDH-locked to a reference cavity on the same silicon nitride chip.

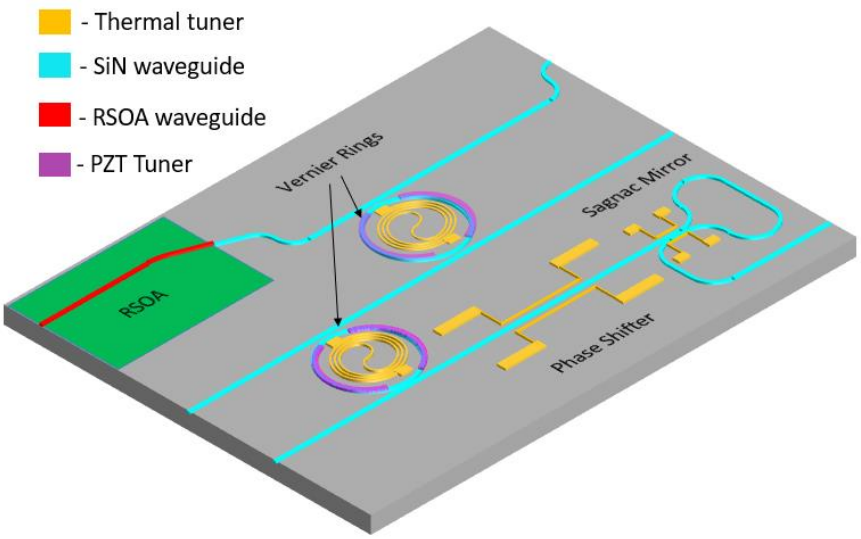


**Figure 6. 5 External cavity laser with PZT actuator integrated on vernier rings and waveguide to detune the laser.**

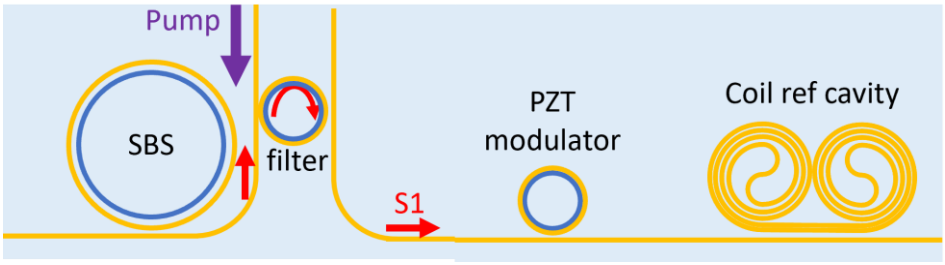


**Figure 6. 6 Photonic integrated stabilized laser source with SBS resonator and reference cavity. The PZT actuator is integrated on top of the SBS resonator and filter to directly control the SBS laser. The PZT ring modulator is used as DSB modulator to generate sidebands on the laser carrier for PDH locking to the coil reference cavity.**

## References


1. N. Chauhan, J. Wang, D. Bose, K. Liu, R. L. Compton, C. Fertig, C. W. Hoyt, and D. J. Blumenthal, "Ultra-low loss visible light waveguides for integrated atomic, molecular, and quantum photonics," Opt. Express, OE **30**, 6960–6969 (2022).

2. K. Liu, N. Jin, H. Cheng, N. Chauhan, M. W. Puckett, K. D. Nelson, R. O. Behunin, R. O. Behunin, P. T. Rakich, and D. J. Blumenthal, "Ultralow 0.034 dB/m loss wafer-scale integrated photonics realizing 720 million Q and 380 μW threshold Brillouin lasing," Opt. Lett., OL **47**, 1855–1858 (2022).

3. S. Gundavarapu, G. M. Brodnik, M. Puckett, T. Huffman, D. Bose, R. Behunin, J. Wu, T. Qiu, C. Pinho, N. Chauhan, J. Nohava, P. T. Rakich, K. D. Nelson, M. Salit, and D. J. Blumenthal, "Sub-hertz fundamental linewidth photonic integrated Brillouin laser," Nature Photonics **13**, 60–67 (2019).

4. T. Huffman, D. Baney, and D. J. Blumenthal, "High Extinction Ratio Widely Tunable Low-Loss Integrated Si3N4 Third-Order Filter," 12 (n.d.).

5. K. Liu, N. Chauhan, J. Wang, A. Isichenko, G. M. Brodnik, P. A. Morton, R. Behunin, R. Behunin, S. B. Papp, S. B. Papp, and D. J. Blumenthal, "Semiconductor laser stabilized by a photonic integrated 4 meter coil-waveguide resonator," in *Optical Fiber Communication Conference (OFC) 2022 (2022), Paper Tu3D.2* (Optica Publishing Group, 2022), p. Tu3D.2.

6. X. Xue, Y. Xuan, C. Wang, P.-H. Wang, Y. Liu, B. Niu, D. E. Leaird, M. Qi, and A. M. Weiner, "Thermal tuning of Kerr frequency combs in silicon nitride microring resonators," Opt. Express, OE **24**, 687–698 (2016).

7. W. Jin, R. G. Polcawich, P. A. Morton, and J. E. Bowers, "Piezoelectrically tuned silicon nitride ring resonator," Opt. Express, OE **26**, 3174–3187 (2018).

8. N. Hosseini, R. Dekker, M. Hoekman, M. Dekkers, J. Bos, A. Leinse, and R. Heideman, "Stress-optic modulator in TriPleX platform using a piezoelectric lead zirconate titanate (PZT) thin film," Opt. Express, OE **23**, 14018–14026 (2015).

9. K. Liu, N. Chauhan, J. Wang, A. Isichenko, G. M. Brodnik, P. A. Morton, R. O. Behunin, R. O. Behunin, S. B. Papp, S. B. Papp, and D. J. Blumenthal, "36 Hz integral

linewidth laser based on a photonic integrated 4.0 m coil resonator," Optica, OPTICA **9**, 770–775 (2022).

10. T. Komljenovic, S. Srinivasan, E. Norberg, M. Davenport, G. Fish, and J. E. Bowers, "Widely Tunable Narrow-Linewidth Monolithically Integrated External-Cavity Semiconductor Lasers," IEEE Journal of Selected Topics in Quantum Electronics **21**, 214–222 (2015).

11. D. J. Blumenthal, R. Heideman, D. Geuzebroek, A. Leinse, and C. Roeloffzen, "Silicon Nitride in Silicon Photonics," Proc. IEEE **106**, 2209–2231 (2018).

12. C. Sorace-Agaskar, D. Kharas, S. Yegnanarayanan, R. T. Maxson, G. N. West, W. Loh, S. Bramhavar, R. J. Ram, J. Chiaverini, J. Sage, and P. Juodawlkis, "Versatile Silicon Nitride and Alumina Integrated Photonic Platforms for the Ultraviolet to Short-Wave Infrared," IEEE J. Select. Topics Quantum Electron. **25**, 1–15 (2019).

13. A. Orieux and E. Diamanti, "Recent advances on integrated quantum communications," J. Opt. **18**, 083002 (2016).

14. A. W. Elshaari, W. Pernice, K. Srinivasan, O. Benson, and V. Zwiller, "Hybrid integrated quantum photonic circuits," Nat. Photonics **14**, 285–298 (2020).

15. Z. L. Newman, V. Maurice, T. Drake, J. R. Stone, T. C. Briles, D. T. Spencer, C. Fredrick, Q. Li, D. Westly, B. R. Ilic, B. Shen, M.-G. Suh, K. Y. Yang, C. Johnson, D. M. S. Johnson, L. Hollberg, K. J. Vahala, K. Srinivasan, S. A. Diddams, J. Kitching, S. B. Papp, and M. T. Hummon, "Architecture for the photonic integration of an optical atomic clock," Optica, OPTICA **6**, 680–685 (2019).

16. A. D. Ludlow, M. M. Boyd, J. Ye, E. Peik, and P. O. Schmidt, "Optical atomic clocks," Rev. Mod. Phys. **87**, 637–701 (2015).

17. J. Levine, "Introduction to time and frequency metrology," Review of Scientific Instruments **70**, 2567–2596 (1999).

18. T. J. Kippenberg, R. Holzwarth, and S. A. Diddams, "Microresonator-Based Optical Frequency Combs," **332**, 6 (2011).

19. A. Jadbabaie, N. H. Pilgram, J. Klos, S. Kotochigova, and N. R. Hutzler, "Enhanced molecular yield from a cryogenic buffer gas beam source via excited state chemistry," New J. Phys. (2020).

20. D. Marpaung, C. Roeloffzen, R. Heideman, A. Leinse, S. Sales, and J. Capmany, "Integrated microwave photonics," Laser & Photonics Reviews **7**, 506–538 (2013).

21. C. G. H. Roeloffzen, L. Zhuang, C. Taddei, A. Leinse, R. G. Heideman, P. W. L. van Dijk, R. M. Oldenbeuving, D. A. I. Marpaung, M. Burla, and K.-J. Boller, "Silicon nitride microwave photonic circuits," Opt. Express, OE **21**, 22937–22961 (2013).

22. G. M. Brodnik, M. W. Harrington, J. H. Dallyn, D. Bose, W. Zhang, L. Stern, P. A. Morton, R. O. Behunin, S. B. Papp, and D. J. Blumenthal, "Optically synchronized fibre links using spectrally pure chip-scale lasers," Nat. Photon. **15**, 588–593 (2021).

23. M. Schioppo, J. Kronjäger, A. Silva, R. Ilieva, J. W. Paterson, C. F. A. Baynham, W. Bowden, I. R. Hill, R. Hobson, A. Vianello, M. Dovale-Álvarez, R. A. Williams, G. Marra, H. S. Margolis, A. Amy-Klein, O. Lopez, E. Cantin, H. Álvarez-Martínez, R. Le Targat, P. E. Pottie, N. Quintin, T. Legero, S. Häfner, U. Sterr, R. Schwarz, S. Dörscher, C. Lisdat, S. Koke, A. Kuhl, T. Waterholter, E. Benkler, and G. Grosche, "Comparing ultrastable lasers at 7 × 10−17 fractional frequency instability through a 2220 km optical fibre network," Nat Commun **13**, 212 (2022).

24. K. Beloy, M. I. Bodine, T. Bothwell, S. M. Brewer, S. L. Bromley, J.-S. Chen, J.-D. Deschênes, S. A. Diddams, R. J. Fasano, T. M. Fortier, Y. S. Hassan, D. B. Hume, D. Kedar, C. J. Kennedy, I. Khader, A. Koepke, D. R. Leibrandt, H. Leopardi, A. D. Ludlow, W. F. McGrew, W. R. Milner, N. R. Newbury, D. Nicolodi, E. Oelker, T. E. Parker, J. M. Robinson, S. Romisch, S. A. Schäffer, J. A. Sherman, L. C. Sinclair, L. Sonderhouse, W. C. Swann, J. Yao, J. Ye, X. Zhang, and Boulder Atomic Clock Optical Network (BACON) Collaboration*, "Frequency ratio measurements at 18-digit accuracy using an optical clock network," Nature **591**, 564–569 (2021).

25. D. J. Blumenthal, H. Ballani, R. O. Behunin, J. E. Bowers, P. Costa, D. Lenoski, P. A. Morton, S. B. Papp, and P. T. Rakich, "Frequency-Stabilized Links for Coherent WDM Fiber Interconnects in the Datacenter," J. Lightwave Technol., JLT **38**, 3376–3386 (2020).

26. S. Olmschenk, K. C. Younge, D. L. Moehring, D. N. Matsukevich, P. Maunz, and C. Monroe, "Manipulation and detection of a trapped ${\mathrm{Yb}}^{+}$ hyperfine qubit," Phys. Rev. A **76**, 052314 (2007).

27. P. De Heyn, J. De Coster, P. Verheyen, G. Lepage, M. Pantouvaki, P. Absil, W. Bogaerts, J. Van Campenhout, and D. Van Thourhout, "Fabrication-Tolerant Four-Channel Wavelength-Division-Multiplexing Filter Based on Collectively Tuned Si Microrings," J. Lightwave Technol. **31**, 2785–2792 (2013).

28. X. Shi, J. Zhang, X. Zeng, X. Lü, K. Liu, J. Xi, Y. Ye, and Z. Lu, "Suppression of residual amplitude modulation effects in Pound–Drever–Hall locking," Appl. Phys. B **124**, 153 (2018).

29. Y. Zeng, Z. Fu, Y.-Y. Liu, X.-D. He, M. Liu, P. Xu, X.-H. Sun, and J. Wang, "Stabilizing a laser frequency by the Pound–Drever–Hall technique with an acousto-optic modulator," Appl. Opt. **60**, 1159 (2021).

30. E. D. Black, "An introduction to Pound–Drever–Hall laser frequency stabilization," American Journal of Physics **69**, 79–87 (2001).

31. J. I. Thorpe, K. Numata, and J. Livas, "Laser frequency stabilization and control through offset sideband locking to optical cavities," Opt. Express, OE **16**, 15980–15990 (2008).

32. Q.-X. Li, S.-H. Yan, E. Wang, X. Zhang, and H. Zhang, "High-precision and fast-response laser power stabilization system for cold atom experiments," AIP Advances **8**, 095221 (2018).

33. Y. Fan, A. van Rees, P. J. M. van der Slot, J. Mak, R. M. Oldenbeuving, M. Hoekman, D. Geskus, C. G. H. Roeloffzen, and K.-J. Boller, "Hybrid integrated InP-$Si_3N_4$ diode laser with a 40-Hz intrinsic linewidth," Opt. Express, OE **28**, 21713–21728 (2020).

34. T. J. Kippenberg, A. L. Gaeta, M. Lipson, and M. L. Gorodetsky, "Dissipative Kerr solitons in optical microresonators," Science **361**, eaan8083 (2018).

35. Z. Ye, A. Fülöp, Ó. B. Helgason, P. A. Andrekson, and V. Torres-Company, "Low-loss high-Q silicon-rich silicon nitride microresonators for Kerr nonlinear optics," Opt. Lett., OL **44**, 3326–3329 (2019).

36. B. J. Eggleton, C. G. Poulton, P. T. Rakich, M. J. Steel, and G. Bahl, "Brillouin integrated photonics," Nat. Photonics **13**, 664–677 (2019).

37. N. Chauhan, A. Isichenko, K. Liu, J. Wang, Q. Zhao, R. O. Behunin, P. T. Rakich, A. M. Jayich, C. Fertig, C. W. Hoyt, and D. J. Blumenthal, "Visible light photonic integrated Brillouin laser," Nat Commun **12**, 4685 (2021).

38. R. J. Niffenegger, J. Stuart, C. Sorace-Agaskar, D. Kharas, S. Bramhavar, C. D. Bruzewicz, W. Loh, R. T. Maxson, R. McConnell, D. Reens, G. N. West, J. M. Sage, and J. Chiaverini, "Integrated multi-wavelength control of an ion qubit," Nature **586**, 538–542 (2020).

39. K. Liu, N. Chauhan, J. Wang, P. A. Morton, R. Behunin, R. Behunin, and D. J. Blumenthal, "Precision Laser Stabilization using Photonic Integrated Coil Resonator," in *Frontiers in Optics + Laser Science 2021 (2021), Paper FTh2A.1* (Optica Publishing Group, 2021), p. FTh2A.1.

40. P. R. Stanfield, A. J. Leenheer, C. P. Michael, R. Sims, and M. Eichenfield, "CMOS-compatible, piezo-optomechanically tunable photonics for visible wavelengths and cryogenic temperatures," Opt. Express, OE **27**, 28588–28605 (2019).

41. M. Dong, G. Clark, A. J. Leenheer, M. Zimmermann, D. Dominguez, A. J. Menssen, D. Heim, G. Gilbert, D. Englund, and M. Eichenfield, "High-speed programmable photonic circuits in a cryogenically compatible, visible–near-infrared 200 mm CMOS architecture," Nat. Photon. **16**, 59–65 (2022).

42. Q. Li, T. C. Briles, D. A. Westly, T. E. Drake, J. R. Stone, B. R. Ilic, S. A. Diddams, S. B. Papp, and K. Srinivasan, "Stably accessing octave-spanning microresonator frequency combs in the soliton regime," Optica, OPTICA **4**, 193–203 (2017).

43. S. Miller, Y.-H. D. Lee, J. Cardenas, A. L. Gaeta, and M. Lipson, "Electro-optic effect in silicon nitride," in *CLEO: 2015* (OSA, 2015), p. SF1G.4.

44. Q. Xu, B. Schmidt, S. Pradhan, and M. Lipson, "Micrometre-scale silicon electro-optic modulator," Nature **435**, 325–327 (2005).

45. A. N. R. Ahmed, S. Shi, M. Zablocki, P. Yao, and D. W. Prather, "Tunable hybrid silicon nitride and thin-film lithium niobate electro-optic microresonator," Opt. Lett., OL **44**, 618–621 (2019).

46. K. Alexander, J. P. George, J. Verbist, K. Neyts, B. Kuyken, D. Van Thourhout, and J. Beeckman, "Nanophotonic Pockels modulators on a silicon nitride platform," Nat Commun **9**, 3444 (2018).

47. A. Hermans, M. V. Daele, J. Dendooven, S. Clemmen, C. Detavernier, and R. Baets, "Integrated silicon nitride electro-optic modulators with atomic layer deposited overlays," Opt. Lett., OL **44**, 1112–1115 (2019).

48. Y. Zhang, J. Nauriyal, M. Song, M. G. Baez, X. He, T. Macdonald, and J. Cardenas, "Engineered second-order nonlinearity in silicon nitride," Opt. Mater. Express, OME **13**, 237–246 (2023).

49. B. Zabelich, C. Lafforgue, E. Nitiss, A. Stroganov, and C.-S. Brès, "Silicon nitride electric-field poled microresonator modulator," APL Photonics **9**, 016101 (2024).

50. H. Tian, J. Liu, B. Dong, J. C. Skehan, M. Zervas, T. J. Kippenberg, and S. A. Bhave, "Hybrid integrated photonics using bulk acoustic resonators," Nat Commun **11**, 3073 (2020).

51. A. Mazzalai, D. Balma, N. Chidambaram, R. Matloub, and P. Muralt, "Characterization and Fatigue of the Converse Piezoelectric Effect in PZT Films for MEMS Applications," Journal of Microelectromechanical Systems **24**, 831–838 (2015).

52. J. Liu, H. Tian, E. Lucas, A. S. Raja, G. Lihachev, R. N. Wang, J. He, T. Liu, M. H. Anderson, W. Weng, S. A. Bhave, and T. J. Kippenberg, "Monolithic piezoelectric control of soliton microcombs," Nature **583**, 385–390 (2020).

53. J. M. Arrazola, V. Bergholm, K. Brádler, T. R. Bromley, M. J. Collins, I. Dhand, A. Fumagalli, T. Gerrits, A. Goussev, L. G. Helt, J. Hundal, T. Isacsson, R. B. Israel, J.

Izaac, S. Jahangiri, R. Janik, N. Killoran, S. P. Kumar, J. Lavoie, A. E. Lita, D. H. Mahler, M. Menotti, B. Morrison, S. W. Nam, L. Neuhaus, H. Y. Qi, N. Quesada, A. Repingon, K. K. Sabapathy, M. Schuld, D. Su, J. Swinarton, A. Száva, K. Tan, P. Tan, V. D. Vaidya, Z. Vernon, Z. Zabaneh, and Y. Zhang, "Quantum circuits with many photons on a programmable nanophotonic chip," Nature **591**, 54–60 (2021).

54. J. F. Bauters, M. J. R. Heck, D. John, D. Dai, M.-C. Tien, J. S. Barton, A. Leinse, R. G. Heideman, D. J. Blumenthal, and J. E. Bowers, "Ultra-low-loss high-aspect-ratio Si_3N_4 waveguides," Opt. Express **19**, 3163 (2011).

55. S. Trolier-McKinstry and P. Muralt, "Thin Film Piezoelectrics for MEMS," Journal of Electroceramics **12**, 7–17 (2004).

56. W. A. Lanford and M. J. Rand, "The hydrogen content of plasma-deposited silicon nitride," Journal of Applied Physics **49**, 2473–2477 (2008).

57. R. Germann, H. W. M. Salemink, R. Beyeler, G. L. Bona, F. Horst, I. Massarek, and B. J. Offrein, "Silicon Oxynitride Layers for Optical Waveguide Applications," J. Electrochem. Soc. **147**, 2237 (2000).

58. N. Ledermann, P. Muralt, J. Baborowski, S. Gentil, K. Mukati, M. Cantoni, A. Seifert, and N. Setter, "{1 0 0}-Textured, piezoelectric Pb(Zrx, Ti1−x)O3 thin films for MEMS: integration, deposition and properties," Sensors and Actuators A: Physical **105**, 162–170 (2003).

59. J. Li, H. Lee, K. Y. Yang, and K. J. Vahala, "Sideband spectroscopy and dispersion measurement in microcavities," Opt. Express, OE **20**, 26337–26344 (2012).

60. D. K. Armani, T. J. Kippenberg, S. M. Spillane, and K. J. Vahala, "Ultra-high-Q toroid microcavity on a chip," Nature **421**, 925–928 (2003).

61. T. Wei, J. Huang, X. Lan, Q. Han, and H. Xiao, "Optical fiber sensor based on a radio frequency Mach–Zehnder interferometer," Opt. Lett., OL **37**, 647–649 (2012).

62. M. W. Puckett, K. Liu, N. Chauhan, Q. Zhao, N. Jin, H. Cheng, J. Wu, R. O. Behunin, P. T. Rakich, K. D. Nelson, and D. J. Blumenthal, "422 Million intrinsic quality factor

planar integrated all-waveguide resonator with sub-MHz linewidth," Nature Communications **12**, 934 (2021).

63. W. Bogaerts, P. De Heyn, T. Van Vaerenbergh, K. De Vos, S. Kumar Selvaraja, T. Claes, P. Dumon, P. Bienstman, D. Van Thourhout, and R. Baets, "Silicon microring resonators," Laser & Photon. Rev. **6**, 47–73 (2012).

64. Q. Zhao, R. O. Behunin, P. T. Rakich, N. Chauhan, A. Isichenko, J. Wang, C. Hoyt, C. Fertig, M. hong Lin, and D. J. Blumenthal, "Low-loss low thermo-optic coefficient $Ta_2O_5$ on crystal quartz planar optical waveguides," APL Photonics **5**, 116103 (2020).

65. M. D. Nguyen, E. P. Houwman, and G. Rijnders, "Large piezoelectric strain with ultra-low strain hysteresis in highly c-axis oriented Pb(Zr0.52Ti0.48)O3 films with columnar growth on amorphous glass substrates," Sci Rep **7**, 12915 (2017).

66. C. Wang, M. Zhang, B. Stern, M. Lipson, and M. Lončar, "Nanophotonic lithium niobate electro-optic modulators," Opt. Express, OE **26**, 1547–1555 (2018).

67. S. Karimelahi and A. Sheikholeslami, "Ring modulator small-signal response analysis based on pole-zero representation," Opt. Express, OE **24**, 7585–7599 (2016).

68. H. Yu, D. Ying, M. Pantouvaki, J. V. Campenhout, P. Absil, Y. Hao, J. Yang, and X. Jiang, "Trade-off between optical modulation amplitude and modulation bandwidth of silicon micro-ring modulators," Opt. Express, OE **22**, 15178–15189 (2014).

69. B. Pile and G. Taylor, "Small-signal analysis of microring resonator modulators," Opt. Express, OE **22**, 14913–14928 (2014).

70. J. Müller, F. Merget, S. S. Azadeh, J. Hauck, S. R. García, B. Shen, and J. Witzens, "Optical Peaking Enhancement in High-Speed Ring Modulators," Sci Rep **4**, 6310 (2014).

71. L. Chen, J. Chen, J. Nagy, and R. M. Reano, "Highly linear ring modulator from hybrid silicon and lithium niobate," Opt. Express **23**, 13255 (2015).

72. A. Ayazi, T. Baehr-Jones, Y. Liu, A. E.-J. Lim, and M. Hochberg, "Linearity of silicon ring modulators for analog optical links," Opt. Express **20**, 13115 (2012).

73. R. S. Guzzon, E. J. Norberg, and L. A. Coldren, "Spurious-Free Dynamic Range in Photonic Integrated Circuit Filters With Semiconductor Optical Amplifiers," IEEE Journal of Quantum Electronics **48**, 269–278 (2012).

74. R. W. P. Drever, J. L. Hall, F. V. Kowalski, J. Hough, G. M. Ford, A. J. Munley, and H. Ward, "Laser phase and frequency stabilization using an optical resonator," Appl. Phys. B **31**, 97–105 (1983).

75. S. Ding, Y. Wu, I. A. Finneran, J. J. Burau, and J. Ye, "Sub-Doppler Cooling and Compressed Trapping of YO Molecules at $\ensuremath{\mu}\mathrm{K}$ Temperatures," Phys. Rev. X **10**, 021049 (2020).

76. J. L. Bohn, A. M. Rey, and J. Ye, "Cold molecules: Progress in quantum engineering of chemistry and quantum matter," Science **357**, 1002–1010 (2017).

77. D. S. Jin and J. Ye, "Introduction to Ultracold Molecules: New Frontiers in Quantum and Chemical Physics," Chem. Rev. **112**, 4801–4802 (2012).

78. Y.-H. Lai, M.-G. Suh, Y.-K. Lu, B. Shen, Q.-F. Yang, H. Wang, J. Li, S. H. Lee, K. Y. Yang, and K. Vahala, "Earth rotation measured by a chip-scale ring laser gyroscope," Nat. Photonics **14**, 345–349 (2020).

79. P. Kwee, C. Bogan, K. Danzmann, M. Frede, H. Kim, P. King, J. Pöld, O. Puncken, R. L. Savage, F. Seifert, P. Wessels, L. Winkelmann, and B. Willke, "Stabilized high-power laser system for the gravitational wave detector advanced LIGO," Opt. Express, OE **20**, 10617–10634 (2012).

80. T. Kessler, C. Hagemann, C. Grebing, T. Legero, U. Sterr, F. Riehle, M. J. Martin, L. Chen, and J. Ye, "A sub-40-mHz-linewidth laser based on a silicon single-crystal optical cavity," Nature Photon **6**, 687–692 (2012).

81. M. Fujieda, M. Kumagai, S. Nagano, A. Yamaguchi, H. Hachisu, and T. Ido, "All-optical link for direct comparison of distant optical clocks," Opt. Express **19**, 16498 (2011).

82. J. Tao, H. Cai, Y. Gu, and A. Liu, "Demonstration of a compact wavelength tracker using a tunable silicon resonator," Opt. Express **22**, 24104 (2014).

83. K. Liu, J. H. Dallyn, and G. M. Brodnik, "Photonic circuits for laser stabilization with integrated ultra-high Q and Brillouin laser resonators," APL Photonics 10 (2022).

84. Y.-H. Lai, D. Eliyahu, S. Ganji, R. Moss, I. Solomatine, E. Lopez, E. Tran, A. Savchenkov, A. Matsko, and S. Williams, "780 nm narrow-linewidth self-injection-locked WGM lasers," in *Laser Resonators, Microresonators, and Beam Control XXII* (International Society for Optics and Photonics, 2020), Vol. 11266, p. 112660O.

85. C. Xiang, J. Guo, W. Jin, L. Wu, J. Peters, W. Xie, L. Chang, B. Shen, H. Wang, Q.-F. Yang, D. Kinghorn, M. Paniccia, K. J. Vahala, P. A. Morton, and J. E. Bowers, "High-performance lasers for fully integrated silicon nitride photonics," Nat Commun **12**, 6650 (2021).

86. S. V. Boriskina, "Photonic Molecules and Spectral Engineering," in *Photonic Microresonator Research and Applications*, I. Chremmos, O. Schwelb, and N. Uzunoglu, eds., Springer Series in Optical Sciences (Springer US, 2010), pp. 393–421.

87. S. Kasap, *Principles of Electronic Materials and Devices*, 3rd ed. (McGraw-Hill, Inc., 2005).

88. L. Lu, J. D. Joannopoulos, and M. Soljačić, "Topological photonics," Nature Photonics **8**, 821–829 (2014).

89. M. Zhang, C. Wang, Y. Hu, A. Shams-Ansari, T. Ren, S. Fan, and M. Lončar, "Electronically programmable photonic molecule," Nature Photon **13**, 36–40 (2019).

90. M. J. Hartmann, F. G. S. L. Brandão, and M. B. Plenio, "Quantum many-body phenomena in coupled cavity arrays," Laser & Photonics Reviews **2**, 527–556 (2008).

91. K. Liao, X. Hu, T. Gan, Q. Liu, Z. Wu, C. Fan, X. Feng, C. Lu, Y. Liu, and Q. Gong, "Photonic molecule quantum optics," Adv. Opt. Photon. **12**, 60 (2020).

92. L. A. M. Barea, F. Vallini, P. F. Jarschel, and N. C. Frateschi, "Silicon technology compatible photonic molecules for compact optical signal processing," Appl. Phys. Lett. **103**, 201102 (2013).

93. S. V. Boriskina, "Spectrally engineered photonic molecules as optical sensors with enhanced sensitivity: a proposal and numerical analysis," J. Opt. Soc. Am. B **23**, 1565 (2006).

94. M. Pöllinger and A. Rauschenbeutel, "All-optical signal processing at ultra-low powers in bottle microresonators using the Kerr effect," Opt. Express, OE **18**, 17764–17775 (2010).

95. L. A. M. Barea, M. C. M. M. Souza, G. F. M. Rezende, and N. C. Frateschi, "Photonic molecules for optical signal processing," in *2014 IEEE Photonics Conference* (2014), pp. 54–55.

96. T. Carmon and K. J. Vahala, "Visible continuous emission from a silica microphotonic device by third-harmonic generation," Nature Phys **3**, 430–435 (2007).

97. J. Zhu, S. K. Ozdemir, Y.-F. Xiao, L. Li, L. He, D.-R. Chen, and L. Yang, "On-chip single nanoparticle detection and sizing by mode splitting in an ultrahigh-Q microresonator," Nature Photon **4**, 46–49 (2010).

98. A. M. Armani, R. P. Kulkarni, S. E. Fraser, R. C. Flagan, and K. J. Vahala, "Label-Free, Single-Molecule Detection with Optical Microcavities," Science **317**, 783–787 (2007).

99. W. Yoshiki and T. Tanabe, "All-optical switching using Kerr effect in a silica toroid microcavity," Opt. Express, OE **22**, 24332–24341 (2014).

100. K. Nozaki, A. Shinya, S. Matsuo, T. Sato, E. Kuramochi, and M. Notomi, "Ultralow-energy and high-contrast all-optical switch involving Fano resonance based on coupled photonic crystal nanocavities," Opt. Express, OE **21**, 11877–11888 (2013).

101. Q. Xu, S. Sandhu, M. L. Povinelli, J. Shakya, S. Fan, and M. Lipson, "Experimental Realization of an On-Chip All-Optical Analogue to Electromagnetically Induced Transparency," Phys. Rev. Lett. **96**, 123901 (2006).

102. M. C. M. M. Souza, G. F. M. Rezende, L. A. M. Barea, A. A. G. von Zuben, G. S. Wiederhecker, and N. C. Frateschi, "Spectral engineering with coupled microcavities: active control of resonant mode-splitting," Opt. Lett., OL **40**, 3332–3335 (2015).

103. M. A. Popovíc, T. Barwicz, M. R. Watts, P. T. Rakich, L. Socci, E. P. Ippen, F. X. Kärtner, and H. I. Smith, "Multistage high-order microring-resonator add-drop filters," Opt. Lett., OL **31**, 2571–2573 (2006).

104. E. Gil-Santos, C. Baker, A. Lemaitre, C. Gomez, S. Ducci, G. Leo, and I. Favero, "High-precision spectral tuning of micro and nanophotonic cavities by resonantly enhanced photoelectrochemical etching," Nat Commun **8**, 14267 (2017).

105. C. Jarlov, K. A. Atlasov, L. Ferrier, M. Calic, P. Gallo, A. Rudra, B. Dwir, and E. Kapon, "1D and 2D arrays of coupled photonic crystal cavities with a site-controlled quantum wire light source," Opt. Express, OE **21**, 31082–31091 (2013).

106. Ó. B. Helgason, F. R. Arteaga-Sierra, Z. Ye, K. Twayana, P. A. Andrekson, M. Karlsson, J. Schröder, and Victor Torres-Company, "Dissipative solitons in photonic molecules," Nature Photonics 1–6 (2021).

107. L. Chang, X. Jiang, S. Hua, C. Yang, J. Wen, L. Jiang, G. Li, G. Wang, and M. Xiao, "Parity–time symmetry and variable optical isolation in active–passive-coupled microresonators," Nature Photonics **8**, 524–529 (2014).

108. C. Yang, X. Jiang, Q. Hua, S. Hua, Y. Chen, J. Ma, and M. Xiao, "Realization of controllable photonic molecule based on three ultrahigh-Q microtoroid cavities: Realization of controllable photonic molecule based…," Laser & Photonics Reviews **11**, 1600178 (2017).

109. T. Siegle, S. Schierle, S. Kraemmer, B. Richter, S. F. Wondimu, P. Schuch, C. Koos, and H. Kalt, "Photonic molecules with a tunable inter-cavity gap," Light: Science & Applications **6**, e16224–e16224 (2017).

110. W. Yoshiki, A. Chen-Jinnai, T. Tetsumoto, S. Fujii, and T. Tanabe, "Time-domain observation of strong coupling between counter-propagating ultra-high Q whispering

gallery modes," in *Laser Resonators, Microresonators, and Beam Control XVIII* (SPIE, 2016), Vol. 9727, pp. 223–233.

111. J. Wang, K. Liu, M. W. Harrington, R. Q. Rudy, and D. J. Blumenthal, "Silicon nitride stress-optic microresonator modulator for optical control applications," Opt. Express, OE **30**, 31816–31827 (2022).

112. E. F. Franchimon, K. R. Hiremath, R. Stoffer, and M. Hammer, "Interaction of whispering gallery modes in integrated optical microring or microdisk circuits: hybrid coupled mode theory model," J. Opt. Soc. Am. B, JOSAB **30**, 1048–1057 (2013).

113. M. C. M. M. Souza, G. F. M. Rezende, L. A. M. Barea, G. S. Wiederhecker, and N. C. Frateschi, "Modeling quasi-dark states with temporal coupled-mode theory," Opt. Express **24**, 18960 (2016).

114. Ó. B. Helgason, M. Girardi, Z. Ye, F. Lei, J. Schröder, and V. Torres-Company, "Surpassing the nonlinear conversion efficiency of soliton microcombs," Nat. Photon. **17**, 992–999 (2023).

115. J. A. Black, G. Brodnik, G. Brodnik, H. Liu, H. Liu, S.-P. Yu, S.-P. Yu, D. R. Carlson, D. R. Carlson, J. Zang, J. Zang, T. C. Briles, S. B. Papp, and S. B. Papp, "Optical-parametric oscillation in photonic-crystal ring resonators," Optica, OPTICA **9**, 1183–1189 (2022).

116. K. Liu, M. W. Harrington, K. D. Nelson, R. O. Behunin, S. B. Papp, and D. J. Blumenthal, "Photonic integrated cascade-inhibited Brillouin laser with sub-100-mHz fundamental linewidth," in *Conference on Lasers and Electro-Optics (2022), Paper SF2K.1* (Optica Publishing Group, 2022), p. SF2K.1.

117. K. Srinivasan and B. J. H. Stadler, "Magneto-optical materials and designs for integrated TE- and TM-mode planar waveguide isolators: a review [Invited]," Opt. Mater. Express **8**, 3307 (2018).

118. A. D. White, G. H. Ahn, K. V. Gasse, K. Y. Yang, L. Chang, J. E. Bowers, and J. Vučković, "Integrated passive nonlinear optical isolators," Nat. Photon. 1–7 (2022).

119. D. L. Sounas and A. Alù, "Non-reciprocal photonics based on time modulation," Nature Photon **11**, 774–783 (2017).

120. D. B. Sohn, O. E. Örsel, and G. Bahl, "Electrically driven optical isolation through phonon-mediated photonic Autler–Townes splitting," Nat. Photon. 1–6 (2021).

121. L. J. Aplet and J. W. Carson, "A Faraday Effect Optical Isolator," Appl. Opt., AO **3**, 544–545 (1964).

122. Y. Shoji, T. Mizumoto, H. Yokoi, I.-W. Hsieh, and R. M. Osgood Jr., "Magneto-optical isolator with silicon waveguides fabricated by direct bonding," Applied Physics Letters **92**, 071117 (2008).

123. N. A. Estep, D. L. Sounas, J. Soric, and A. Alù, "Magnetic-free non-reciprocity and isolation based on parametrically modulated coupled-resonator loops," Nature Phys **10**, 923–927 (2014).

124. H. Tian, J. Liu, A. Siddharth, R. N. Wang, T. Blésin, J. He, T. J. Kippenberg, and S. A. Bhave, "Magnetic-free silicon nitride integrated optical isolator," Nat. Photon. **15**, 828–836 (2021).